1-1-2007

Polymer nanorods : preparation, analysis, and chemical modification.

Taehyung, Kim
University of Massachusetts Amherst

This is an authorized facsimile, made from the microfilm master copy of the original dissertation or master thesis published by UMI.

The bibliographic information for this thesis is contained in UMI's Dissertation Abstracts database, the only central source for accessing almost every doctoral dissertation accepted in North America since 1861.

POLYMER NANORODS: PREPARATION, ANALYSIS, AND CHEMICAL MODIFICATION

A Dissertation Presented

by

TAEHYUNG KIM

UMI Number: 3254958

INFORMATION TO USERS

UMI®

POLYMER NANORODS: PREPARATION, ANALYSIS, AND CHEMICAL MODIFICATION

A Dissertation Presented

by

TAEHYUNG KIM

Approved as to style and content by:

_____
Thomas J. McCarthy, Chair

_____
Thomas P. Russell, Member

_____
Mark A. Tuominen, Member

_____
Shaw Ling Hsu, Department Head
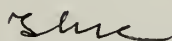Polymer Science and Engineering

POLYMER NANORODS: PREPARATION, ANALYSIS, AND CHEMICAL MODIFICATION

A Dissertation Presented

by

TAEHYUNG KIM
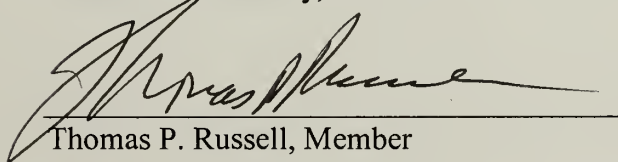
Approved as to style and content by:

_____
Thomas J. McCarthy, Chair
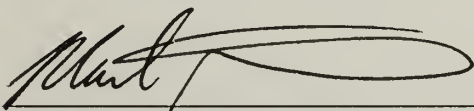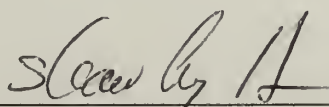
_____
Thomas P. Russell, Member

_____
Mark T. Tuominen, Member

_____
Shaw Ling Hsu, Department Head
Polymer Science and Engineering

To my parents and loving wife. Jinseung

ACKNOWLEDGMENTS

First, I would like to thank my advisor Professor Thomas McCarthy, for his years of thoughtful, patient guidance and support. He has given me enormous research opportunities and the freedom to pursue them. I deeply appreciate help from Professor Thomas Russell, who has been like another advisor to me during my thesis work with scientific advice and guidance. I also thank Professor Mark Tuominen for his valuable comments and suggestions.

My Ph. D. work could have not been accomplished without the assistance of the deparment staff members. I would especially like to thank Jack for discussions and chats which encouraged me, and Lou for help with TEM and SEM experiments.

I want to thank the McCarthy group members, Margarita, Misha, Kevin, Ilke, Ebru, Zhixiang, Jay, Joonsung, Scott, Yufeng, Bokyung, Dalton, Lichao, Jung Ah, and Sung-In, who are good scientists and collegues, and most of all good friends. My classmates deserve my gratitude, Raji, Irene, Joe, Greg, Drew, Amanda, Ting, Angelo, Manuel, Thui, who filled my first year with unforgettable memories. My life in the department would have not been cheerful without many Korean friends, especially Sungkyun, Jin, Dongseok, and Bon-cheol. I also like to express my appreciation to my coworkers, Sung-In, Hongqi, Kyusoon, Lachelle, Sanghyuk, and Firat.

I am truly indebted to my father, who passed away without being able to see me get my Ph. D. degree, and my mother for their constant love and support with my sisters. Most of all, I thank my wife, Jinseung, for he love, patience, support and understanding and my sons, Sungeun and Sungjun, who bring meening to my life.

ABSTRACT

POLYMER NANORODS: PREPARATION. ANALYSIS. AND CHEMICAL
MODIFICATION

FRBRUARY 2007

TAEHYUNG KIM. B.A.. SEOUL NATIONAL UNIVERSITY

M.A.. SEOUL NATIONAL UNIVERSITY

M.A.. UNIVERSITY OF MASSACHUSETTS AMHERST

Ph.D.. UNIVERSITY OF MASSACHUSETTS AMHERST

Directed by: Professor Thomas J. McCarthy

The overall objectives of the projects which constitute this Ph. D. thesis are a

preparation of two-component polymer nanorods using anodic alumina membranes as

templates and an investigation of their structures as well as a possibility for a

preparation of composite nanorods.

Anodic alumina membranes with various pore size prepared by the anodization

of aluminum in electrochemical cell are used as well as commercial membrane (Chapter

2). Diblock copolymer nanorods are prepared using these membranes and their

microphase-separated structures inside the membrane pores are investigated (Chapter 3

and 4). Semicrystalline polymer nanorods are prepared using these membranes and their

composites are prepared by polymerizing second monomer inside these nanorods

(polymer/polymer composite nanorods) or depositing metal clusters inside these

nanorods (polymer/metal composite nanorods) (Chapter 5).

Microphase-separated structures of diblock copolymers inside the cylindrical

membrane pores are affected by the relationship between the size of pores and the repeat

period of the block copolymers (commensurability). Polystyrene-*b*-polybutadiene (PS-*b*-PBD) confined inside the membrane pores show novel structures that cannot be accessed by any other method, caused by the commensurability and large curvature of the templates. The interaction between each block of diblock copolymer and the alumina surface is another factor for the micro-phase separated structures of diblock copolymers inside alumina membrane pores. Surface modification of alumina membrane pores using octyltrimethoxysilane (OTMS) inverted the multi-barrel structure of symmetric polystyrene-*b*-polymethylmethacrylate (PS-*b*-PMMA) and asymmetric PS-*b*-PMMA at large D/L_0, by changing the polarity of the templates. Asymmetric PS-*b*-PMMA at small D/L_0 does not show this inversion.

Poly(4-methyl-1-pentene) (PMP) nanorods are prepared using commercial alumina membranes. PMP/polynorbornene nanorods are prepared by polymerizing norbornene inside PMP nanorods using liquid CO_2 as reaction medium. This also provides a way to observe the structures of these semicrystalline polymer nanorods. PMP/Pt nanorods are prepared by introducing Pt precursors, dimethyl(cyclooctadiene)platinum(II) (CODPtMe$_2$), clusters using supercritical CO_2 as a medium and reducing it with H_2 to form Pt clusters inside PMP nanorods.

TABLE OF CONTENTS

LIST OF TABLES

LIST OF FIGURES

CHAPTER 1

INTRODUCTION

1.1. Overview

Anodized aluminum membranes (AAM) have been of great interest to material scientists for the past decade owing to their interesting features.[1-5] These membranes contain regular cylindrical pores and are heat resistant and tough. The alumina has a high surface energy and is wet by many materials. Moreover, the membrane can be easily dissolved in acidic or basic solution. These features have made alumina membranes good templates for nano-object fabrication, especially nanorods.

Nanorods with regular shape and size can be made using AAMs as templates by forming them inside the regularly packed pores of the membrane and can be building blocks for self-assembled structures. Polymeric nanorods have been recently produced using these membranes.[6,7] The first polymer nanorods and nanotubes using AAMs were prepared by wetting a polymer melt or solution on the membranes.[6] This method has the drawback that the length of the polymer nanorods is not controllable. The McCarthy group developed a practical method in which the length of the polymer nanorods can be controlled by changing heating time.[7]

A nanorod of this sort made up of two components rather than a homogenous nanorod invokes more interest, not only in theory, but also in applications. This thesis work covers two types of two-component nanorods diblock copolymer and semicrystalline polymer nanorods. The aim of this thesis is to prepare block copolymer

1

and semicrystalline polymer nanorods and investigate their structures, including the possibility of preparing composite nanorods.

Chapter 2 describes a procedure for preparing AAMs with various pore sizes. The diameters of the template pores directly affect the morphology of the two-component nanorods as well as the diameter of the produced nanorods. The pore size and pore-to-pore distance is affected by the anodization condition, such as current, voltage, electrolyte composition and temperature. AAMs with pore sizes of less than 100 nm are of interest because the equilibrium period of many block copolymers and the crystal stack distance of semicrystalline polymers is on the order of tens-of-nanometer scale.

Chapter 3 describes the micro-phase separated structure of polystyrene-*b*-polybutadiene (PS-*b*-PBD) prepared from commercial and in house prepared membranes. which represents the strong-segregation limit. The block copolymers were confined inside the nanopores with diameters less than 8 times the equilibrium period and with high curvature. New phases induced from these conditions were observed.

Chapter 4 describes the micro-phase separated structure of polystyrene-*b*-polymethylmethacrylate (PS-*b*-PMMA) prepared from commercial and in house prepared membranes. represents the weak-segregation limit. In addition to pore size, the surface property of AAMs was changed by formation of a silane monolayer. In the case of PS-*b*-PMMA, the surface affinity of each block was changed when the AAM surface was treated with octyltrimethoxysilane.

Chapter 5 describes the preparation of semicrystalline polymer nanorods and their composites with a different polymer or metal clusters. Poly(4-methyl-1-pentene) (PMP) was selected as the substrate nanorod and polynorbornene was selected as the second

2

polymer component. Pt was selected as the metal component. PMP/Polynorbornene nanorods were successfully prepared by polymerizing norbornene inside PMP nanorods in liquid CO_2 by ring-opening metathesis polymerization. PMP/Pt nanorods were successfully prepared by introducing dimethyl(1.5-cyclooctadiene)platinum(II) as an organometallic precursor and reducing it with H_2 in supercritical CO_2.

The balance of this chapter provides the background information on the commensurability of block copolymers in confined geometry, surface modification of metal oxides using silane coupling agents, and subcritical(liquid) and supercritical CO_2 as a reaction media for modifying solid polymer substrates.

1.2. Commensurability

Block copolymer nanorods in alumina pores of defined diameter impact fundamental issues of commensurability, i.e. the relationship between the inherent repeat periods of the copolymer to the physical dimension of the system. If the two are incommensurate then the block copolymer would be forced to shift away from its equilibrium structure to relieve the imposed frustration.

Symmetric diblock copolymers confined between two parallel walls have been studied extensively.[8-17] In this case, one block migrate to the wall surface and the overall structure is a multilayered film. There can be two types of multilayers: a multilayer with identical ends (symmetric case) and a multilayer with different ends (asymmetric case). The film thickness is equal to nL_0 in the symmetric case and is equal to $(n + \frac{1}{2}) L_0$ in the asymmetric case (Figure 1.1.). Both cases are referred to as the commensurate condition.
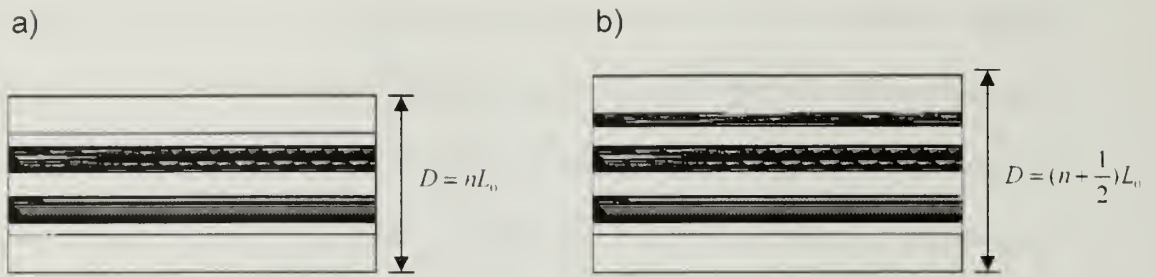
Figure 1.1. Lateral structures of block copolymer thin films between solid substrates in a) symmetric b) asymmetric conditions.

The incommensurate case can be observed when the film thickness is not equal to nL_0 (symmetric case) or $(n + 1/2)$ L_0 (asymmetric case). When a film in an incommensurate condition is located on an open substrate. frustration resulting from incommensurability is relieved by the formation of surface topography consisting of terraces of step height L_0 so that a highly oriented layered structure can propagate throughout the entire film.[12,18] (Figure 1.2)
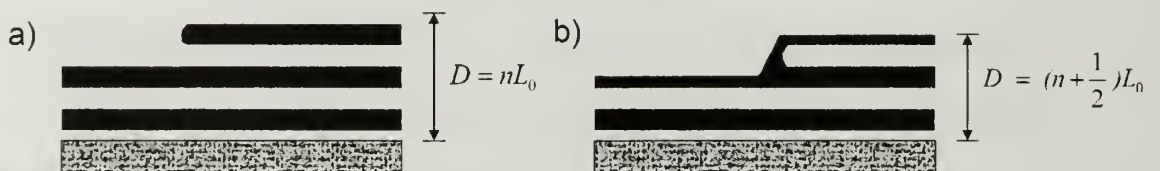
Figure 1.2. Lateral structures of block copolymer thin films on solid substrates in a) symmetric b) asymmetric conditions. Both have incommensurate situations at the left.[12]

When the film is confined between two solid walls, the formation of a surface topography. the mechanism to relieve an imposed frustration in the case of film on open substrate. cannot be applied. Therefore. the copolymer must find an alternative route to respond to this environment. If the interfacial interactions are strong, the period of the

confined multilayers have to either stretch or compress. The thin polymer film cannot relieve the frustration via formation of surface topography. With changes in the thickness of the confined film, the number of layers will change and the stretching or compression of the layers will be distributed throughout the film so that each layer will distort less with increasing thickness. This action preserves the natural period of the copolymer at the expense of the interfacial energies.[19]

Asymmetric diblock copolymers, on the other hand, have drawn much less attention compared with symmetric diblock copolymers. As is in the case of symmetric diblock copolymers, the interplay of the confinement with the preferential interfacial interactions causes deviations of the morphology from that seen in the bulk.

A block copolymer sandwiched between two parallel solid walls experiences an essentially a one-dimensional confinement. Recently, a two-dimensional confinement method has been researched.[20] In addition to the confinement imposed by the film thickness, placing the film into photo-lithographically defined troughs with walls, affects the hexagonal packing of spherical and cylindrical microdomains and can introduce an incommensurability of the in-plane, lateral packing of the copolymer between the natural period and the trough width. The growth of the microdomains along the trough can be used to induce long-range ordering within the trough, which is the key to fabricating sectored surfaces for device applications.

Another type of two-dimensional confinement can be created by use of nanoscopic cylindrical pores that can be conveniently prepared in alumina membrane with pore diameters of the tens-of-nanometer scale. Cylindrical confinement is of particular interest since many situations are met in nature where such confinement

5

influences phase behavior. In addition to confinement, cylindrical nanopores force a curvature on the morphology. So both commensurability between the pore diameter and the natural period and the imposed curvature can strongly influence the morphology of the confined system.

1.3. Surface modification of metal oxide by silylation

When a block copolymer is forced into alumina pores, the interaction between the alumina surface and the outermost layer of the block copolymer plays an important role in determining the morphology of block copolymer as well as the commensurability does. The alumina surface is composed of hydroxyl groups like other metal oxides.[21] Various chemical modification methods have been developed to change the properties of metal oxide surfaces.[22-26] and silylation, the formation of organosilanes layers on the surface, is a recently developed method to modify metal oxide surfaces such as silica[22,27,28] and alumina.[29]

Silylation of silica surface has been researched in broad areas. Hydrophobizing the silica stationary phase with silanes is used to prepare reversed-phase chromatography columns for separation of biomolecules.[30-33] Silylation of surfaces has found applications in producing biocompatible surface,[34-36] lithography,[37] and micropatterning.[38-40]

Organosilanes for modifying metal oxide surfaces have one, two or three hydrolyzable groups in the molecule, and are called mono-, di- and trifunctional organosilanes. Monofunctional organosilanes (R_3SiX, usually X=Cl, OR, NMe_2) have the advantage of reproducible surface structure. It is known that these kinds of organosilanes
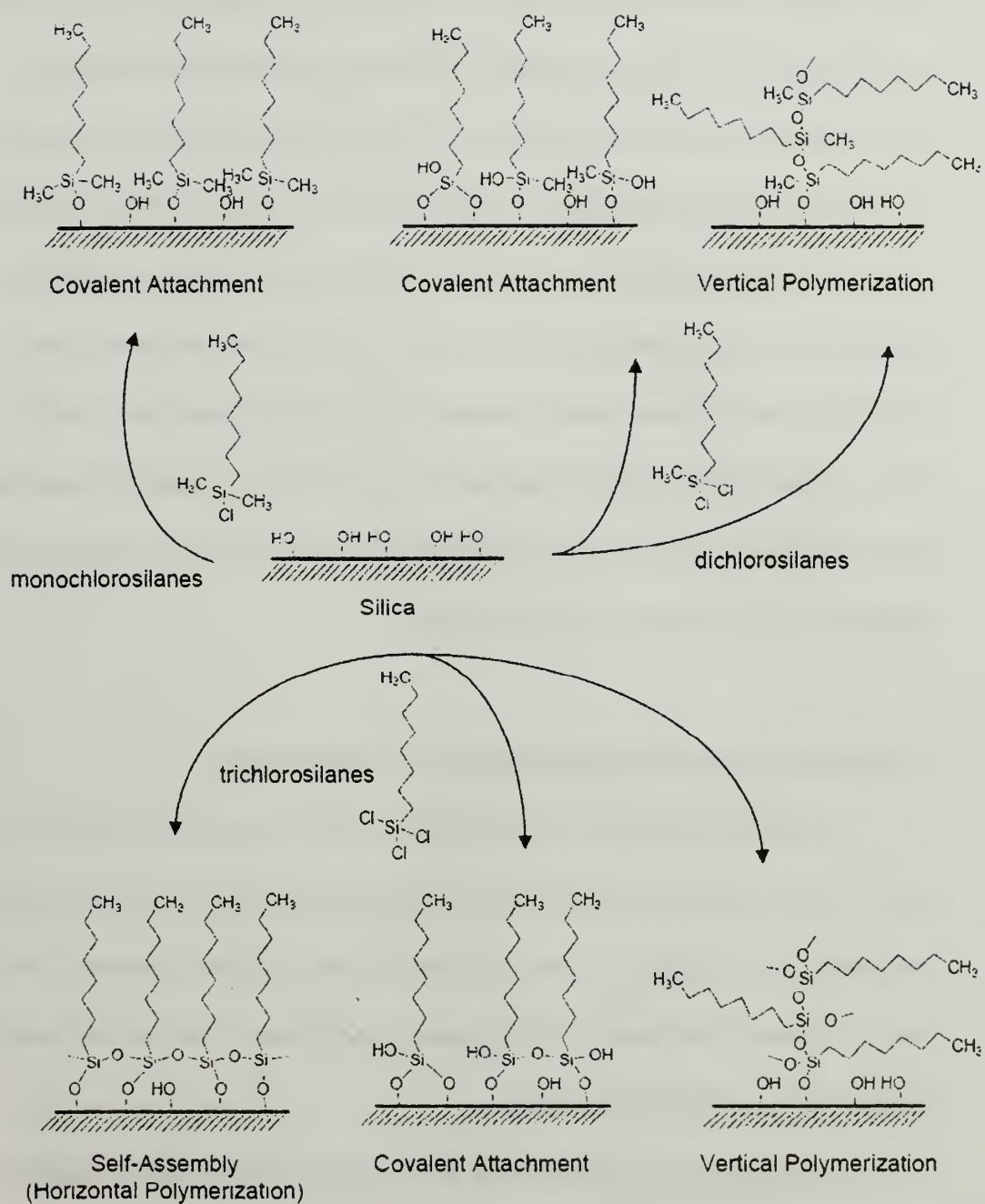
Figure 1.3. Possible products of the reaction of alkylchlorosilanes with silicon oxide surface.[28]

have one kind of attachment with silica by covalent bonding (Si_s-O-Si). Trifunctional organosilanes ($RSiX_3$) are more reactive and have more possible structures. In addition to covalent attachment, they can exhibit two dimensional and three dimensional polycondensation on the surface. (Figure 1.3) Long-chain alkyltrichlorosilanes are the most widely studied, including the self-assembly process and the effect of temperature, solvent and water on the surface properties. Trialkoxysilanes ($Z(CH_2)_nSi(OR)_3$, where R=Me or Et, Z is often amino, epoxy, acryloyl, vinyl, bromo), are often called silane coupling agents and have some advantages over alkyltrichlorosilanes. Trialkoxysilanes don t generate acid on hydrolysis and are more convenient to handle because they are less reactive. The alkoxysilanes undergo exchange reactions with hydroxyl groups under conditions similar to those of carboxylic esters.

1.4. Subcritical (liquid) and supercritical CO_2 as reaction media

Liquid and supercritical CO_2 has attracted both scientific and industrial interest in recent years. A supercritical fluid is any substance above both its critical temperature (T_c) and pressure (P_c). Figure 1.4 shows the phase diagram of a pure substance. The critical point (C) is marked at the end of the gas-liquid equilibrium curve, and the shaded area indicates the supercritical fluid region.

In the supercritical environment, the boundary of liquid and gas disappears and only one phase exists. This phase is termed as supercritical fluid (SCF); it is neither a gas nor a liquid and has unique properties between those of a gas and a liquid. SCFs retain solvent power similar to liquids as well as the transport properties common to gases. They have no surface tension and very low viscosity. Additionally, the density of a SCF

8

can be changed upon minor adjustment of its temperature and pressure. These properties have made SCFs an interesting reaction medium. Table 1.1 provides representative properties of liquid. gas and supercritical fluids.
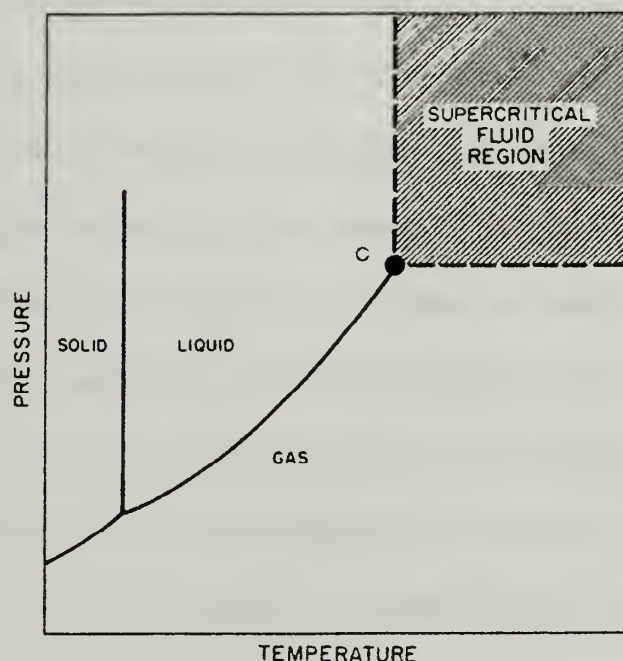
Figure 1.4. Pressure temperature phase diagram for a pure substance.[41]

Table 1.1: Physical property comparison for liquids, gases, and supercritical fluids.

Solvent	Diffusivity (cm^2/sec)	Viscosity (cps)	Density (g/cm^3)	Surface tension (dynes/cm)
Liquid	10^{-5}	1	1.0	20-50
SCF	10^{-3}	0.03	0.2-1.0	0
Gas	10^{-1}	10^{-5}	10^{-3}	-

Carbon dioxide is one of the most commonly used SCF because of its advantages. SC CO_2 has T_c of 31.1 °C and P_c of 73.8 bar (1070 psi) (Table 1.2.). These critical conditions are relatively mild compared with other solvents. Moreover. CO_2 is nontoxic.

9

nonflammable, and inexpensive. It is convenient to recycle CO_2 because it is a gas phase at ambient conditions. Releasing CO_2 as a gas phase leaves no solvent residue.

In addition, two properties of CO_2 are important regarding to polymerization reactions: the solubility of CO_2 and the plasticization effect of CO_2 on the polymer products. The solvent strength of SC CO_2 is similar to that of a typical non-polar solvent. Although it can dissolve many small organic molecules to a certain extent, it cannot dissolve most strongly polar molecules and high molecular weight molecules. Adding cosolvent or surfactant can enhance the solubility of CO_2. Another unique method of manipulating the solvent properties of SC CO_2 is changing its density by temperature and pressure adjustment. Figure 1.5 shows the dependence of CO_2 density on pressure and temperuture. The density of CO_2 changes dramatically by controlling external pressure and temperature, making it possible to increase or decrease the solubility of certain molecules or fractions.

Table 1.2. Critical conditions for various solvents.[41]

Solvents	Critical temperature (°C)	Critical pressure (bar)
Carbon dioxide	31.1	73.8
Ethane	32.2	48.8
Propane	96.7	42.5
Cyclohexane	280.3	40.7
Benzene	289.0	48.9
Toluene	318.6	41.1
p-Xylene	343.1	35.2
Ammonia	132.5	112.8
Water	374.2	220.5

The plasticization effect is another indispensable factor when a polymerization is carried out in liquid or SC CO_2. This is important not only when monomers are diffused into the polymer, but also when additives are incorporated into polymer matix. The T_g depression of amorphous polymers induced by CO_2 has been investigated by some groups.[42-48] The plasticization of polymers has been investigated by studying sorption and dilation of Polyethylmethacrylate (PEMA), poly(vinyl benzoate), and poly(vinyl butyral) by Kamiya and coworkers.[49,50] Figure 1.6 shows that the T_g of PS is depressed with CO_2 pressure and Figure 1.7 shows that the elongation of PEMA increases with CO_2 pressure. The interaction of SC CO_2 with several semi-crystalline polymer was investigated by Shieh et al.[51]

The McCarthy group has developed ideas of polymerization inside plasticed polymer phases and deposition of metal clusters by reducing organometallic precursors in CO_2. Figure 1.8 is a scheme for preparing composite polymer materials.[52,53] In this case, styrene was polymerized inside various swollen polymers. This approach was expanded to the anionic polymerization of ethyl 2-cyanoacrylate within SC CO_2-swollen poly(tetrafluoroethylene-co-hexafluoropropylene)[54] and ring-opening metathesis polymerization of norbornene within SC CO_2-swollen Poly(4-methyl-1-pentene).[55] Figure 1.9 shows a scheme of metal deposition by infusion of organometallic precursors and reduction of them.[56] Platinum clusters were formed in PTFE film and Al_2O_3 membranes.[57]
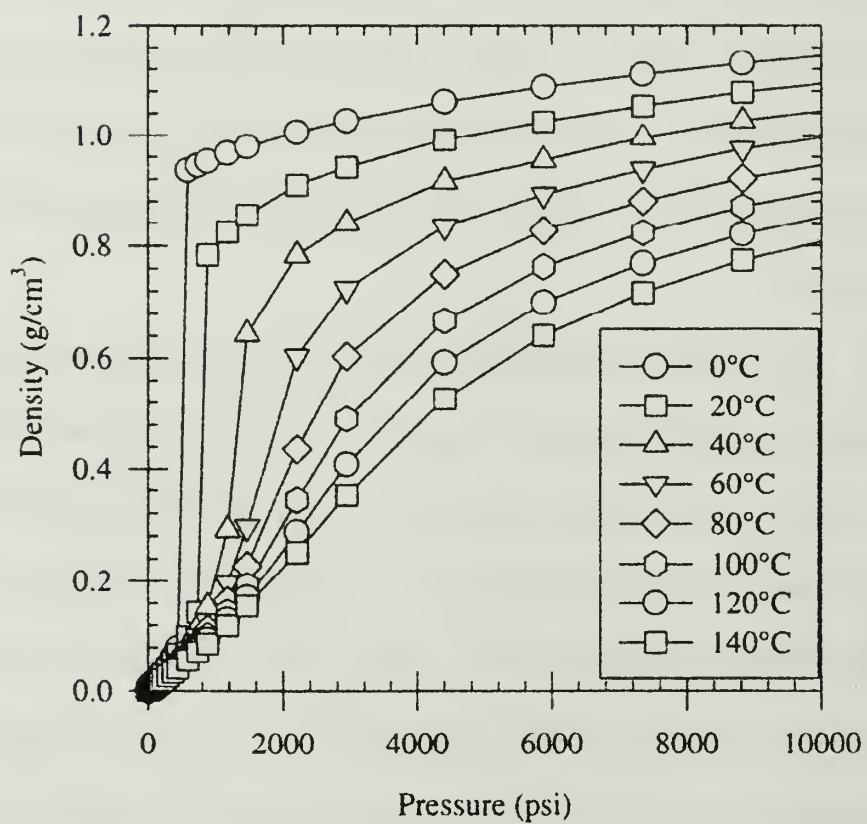
Figure 1.5. Pressure dependence of carbon dioxide density.[58]
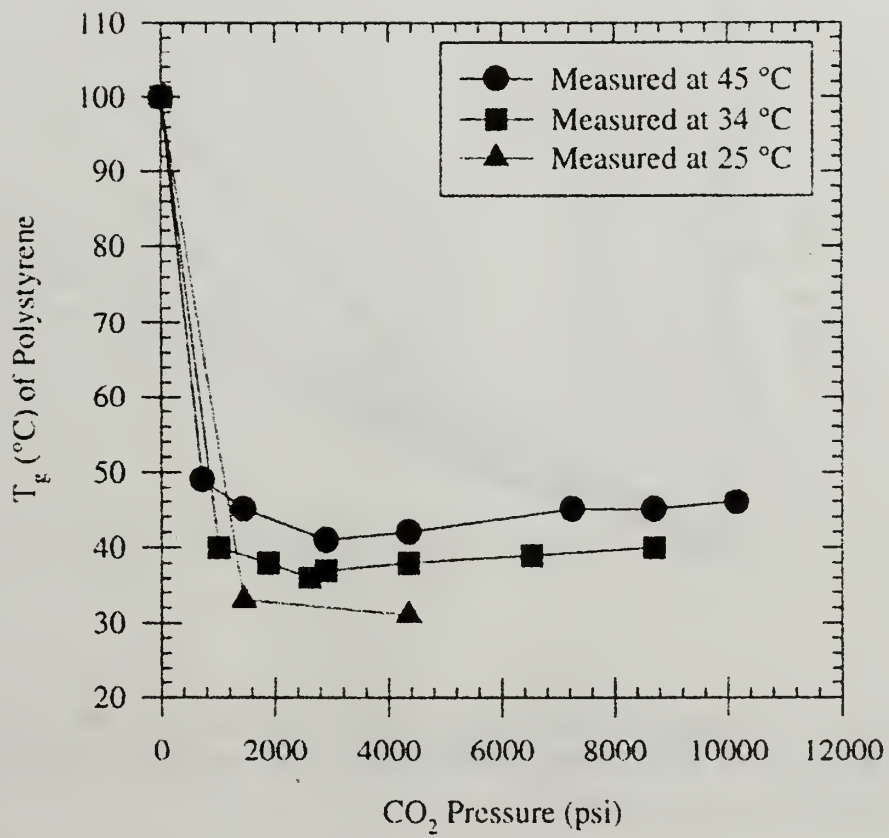
Figure 1.6. Depression of T_g in CO_2-plasticized polystyrene.[42]
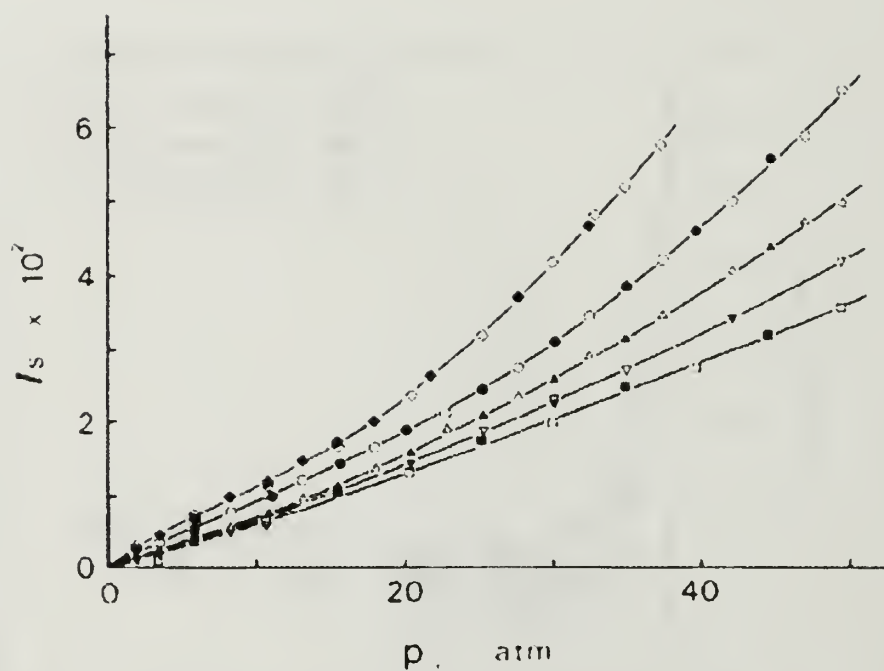
Figure 1.7. Elongation versus pressure for CO2 in PEMA at ($\Diamond,\blacklozenge$) at 15. ($\bigcirc,\bullet$) at 24. ($\triangle,\blacktriangle$) at 35. ($\triangledown,\blacktriangledown$) at 45. and ($\square,\blacksquare$) at 55 °C. Open and solid symbols correspond to sorption and desorption runs.[50]
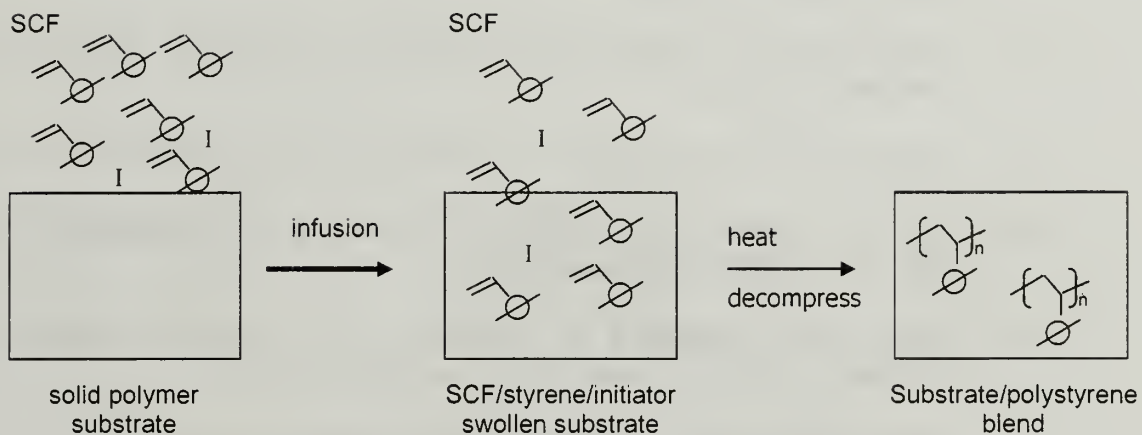
Figure 1.8. Scheme of new route to composite polymer materials.[52,53]
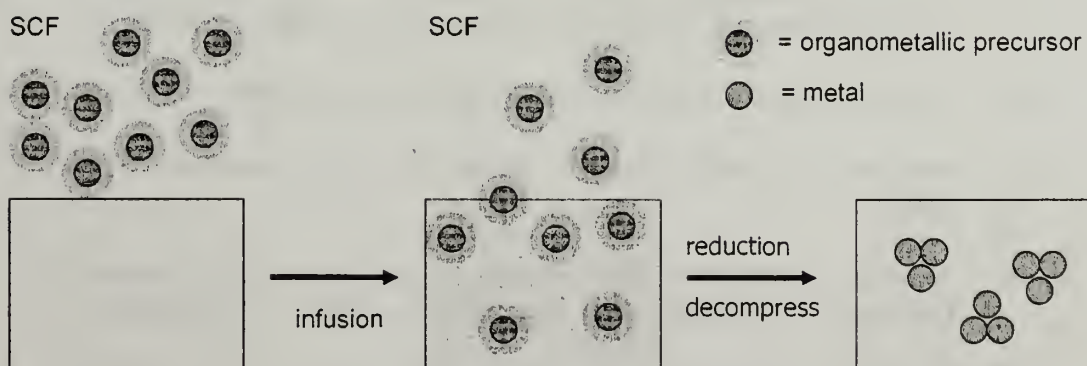
Figure 1.9. SCF strategy for preparing metal/polymer composites (OM=organometallic).[56]

1.5. References

(1)   Martin. C. *Science* **1994**, *266*, 1961.

(2)   Che. G.; Lakshmi. B. B.; Martin. C. R.; Fisher. E. R.; Ruoff. R. S. *Chem. Mater.* **1998**, *10*, 260-267.

(3)   Michailowski. A.; AlMawlawi. D.; Cheng. G. S.; Moskovits. M. *Chem. Phys. Lett.* **2001**, *349*, 1-5.

(4)   Park. S.; Lim. J. H.; Chung. S. W.; Mirkin. C. A. *Science* **2004**, *303*, 348-351.

(5)   Lee. S. B.; Mitchell. D. T.; Trofin. L.; Nevanen. T. K.; Soderlund. H.; Martin. C. R. *Science* **2002**, *296*, 2198-2200.

(6)   Steinhart. M.; Wendorff. J. H.; Greiner. A.; Wehrspohn. R. B.; Nielsch. K.; Schilling. J.; Choi. J.; Gosele. U. *Science* **2002**, *296*, 1997.

(7)   Moon. S. I.; McCarthy. T. J. *Macromolecules* **2003**, *36*, 4253.

(8)   Carvalho. B. L.; Thomas. E. L. *Phys. Rev. Lett.* **1994**, *73*, 3321-3324.

(9)   Milner. S. T.; Morse. D. C. *Phys. Rev. E* **1996**, *54*, 3793-3810.

(10)   Chakrabarti, A.; Chen. H. *J. Polym. Sci. Pol. Phys.* **1998**, *36*, 3127-3136.

(11)   Chen. H.; Chakrabarti. A. *J. Chem. Phys.* **1998**, *108*, 6897-6905.

(12)   Huang. E.; Mansky. P.; Russell. T. P.; Harrison. C.; Chaikin. P. M.; Register, R. A.; Hawker, C. J.; Mays, J. *Macromolecules* **2000**, *33*, 80-88.

(13)   Kim. H. C.; Russell. T. P. *J. Polym. Sci. Pol. Phys.* **2001**, *39*, 663-668.

(14)   Rockford. L.; Mochrie. S. G. J.; Russell. T. P. *Macromolecules* **2001**, *34*, 1487-1492.

(15)   Kellogg. G. J.; Walton. D. G.; Mayes. A. M.; Lambooy. P.; Russell, T. P.; Gallagher. P. D.; Satija. S. K. *Phys. Rev. Lett.* **1996**, *76*, 2503-2506.

(16)   Lambooy. P.; Russell. T. P.; Kellogg. G. J.; Mayes, A. M.; Gallagher, P. D.; Satija. S. K. *Phys. Rev. Lett.* **1994**, *72*, 2899-2902.

(17)   Menelle. A.; Russell. T. P.; Anastasiadis, S. H.; Satija. S. K.; Majkrzak, C. F. *Phys. Rev. Lett.* **1992**, *68*, 67-70.

(18)   Coulon. G.; Collin. B.; Chatenay. D.; Gallot. Y. *Journal De Physique Ii* **1993**, *3*, 697-717.

16

(19)   Koneripalli, N.; Singh, N.; Levicky, R.; Bates, F. S.; Gallagher, P. D.; Satija, S. K. *Macromolecules* **1995**, *28*, 2897-2904.

(20)   Park, C.; Cheng, J. Y.; Fasolka, M. J.; Mayes, A. M.; Ross, C. A.; Thomas, E. L.; De Rosa, C. *Appl. Phys. Lett.* **2001**, *79*, 848-850.

(21)   Tsyganenko, A. A.; Mardilovich, P. P. *J. Chem. Soc. Faraday T.* **1996**, *92*, 4843-4852.

(22)   Badley, R. D.; Ford, W. T.; Mcenroe, F. J.; Assink, R. A. *Langmuir* **1990**, *6*, 792-801.

(23)   Legrange, J. D.; Markham, J. L.; Kurkjian, C. R. *Langmuir* **1993**, *9*, 1749-1753.

(24)   Jansen, J.; Treiner, C.; Vaution, C.; Puisieux, F. *Int. J. Pharm.* **1994**, *103*, 19-26.

(25)   Brown, I. G.; Anders, A.; Dickinson, M. R.; MacGill, R. A.; Monteiro, O. R. *Surf. Coat. Tech.* **1999**, *112*, 271-277.

(26)   Textor, M.; Ruiz, L.; Hofer, R.; Rossi, A.; Feldman, K.; Hahner, G.; Spencer, N. D. *Langmuir* **2000**, *16*, 3257-3271.

(27)   Fadeev, A. Y.; McCarthy, T. J. *Langmuir* **1999**, *15*, 3759-3766.

(28)   Fadeev, A. Y.; McCarthy, T. J. *Langmuir* **2000**, *16*, 7268-7274.

(29)   Kono, M.; Sun, X.; Li, R.; Wong, K. C.; Mitchell, K. A. R.; Foster, T. *Surf. Rev. Lett.* **2001**, *8*, 43-50.

(30)   Abel, E. W.; Pollard, F. H.; Uden, P. C.; Nickless, G. *J. Chromatogr.* **1966**, *22*, 23-&.

(31)   Sander, L. C.; Wise, S. A. *Crit. Rev. Anal. Chem.* **1987**, *18*, 299-415.

(32)   Regnier, F. E.; Unger, K. K.; Majors, R. E. *J. Chromatogr.* **1991**, *544*, R9-R9.

(33)   Biernat, J. F.; Konieczka, P.; Tarbet, B. J. *Sep. Purif. Methods* **1994**, *23*, 77-348.

(34)   Stenger, D. A.; Georger, J. H.; Dulcey, C. S.; Hickman, J. J.; Rudolph, A. S.; Nielsen, T. B.; Mccort, S. M.; Calvert, J. M. *J. Am. Chem. Soc.* **1992**, *114*, 8435-8442.

(35)   Sofia, S. J.; Premnath, V.; Merrill, E. W. *Macromolecules* **1998**, *31*, 5059-5070.

(36)   Zhang, M. Q.; Desai, T.; Ferrari, M. *Biomaterials* **1998**, *19*, 953-960.

(37)   Ross, C. B.; Sun, L.; Crooks, R. M. *Langmuir* **1993**, *9*, 632-636.

(38)   Dulcey, C. S.; Georger, J. H.; Krauthamer, V.; Stenger, D. A.; Fare, T. L.;
        Calvert, J. M. *Science* **1991**, *252*, 551-554.

(39)   Xia, Y. N.; Zhao, X. M.; Whitesides, G. M. *Microelectron. Eng.* **1996**, *32*, 255-
        268.

(40)   Jeon, N. L.; Finnie, K.; Branshaw, K.; Nuzzo, R. G. *Langmuir* **1997**, *13*, 3382-
        3391.

(41)   McHugh, M. A.; Krukonis, V. J. *Supercritical Fluid Extraction*; Butterworth-
        Heinemann: Newton, 1994.

(42)   Wang, W. C. V.; Kramer, E. J.; Sachse, W. H. *J. Polym. Sci. Pol. Phys.* **1982**,
        20, 1371-1384.

(43)   Chiou, J. S.; Barlow, J. W.; Paul, D. R. *J. Appl. Polym. Sci.* **1985**, *30*, 2633-
        2642.

(44)   Wissinger, R. G.; Paulaitis, M. E. *J. Polym. Sci. Pol. Phys.* **1987**, *25*, 2497-2510.

(45)   Wissinger, R. G.; Paulaitis, M. E. *J. Polym. Sci. Pol. Phys.* **1991**, *29*, 631-633.

(46)   Condo, P. D.; Johnston, K. P. *J. Polym. Sci. Pol. Phys.* **1994**, *32*, 523-533.

(47)   Condo, P. D.; Paul, D. R.; Johnston, K. P. *Macromolecules* **1994**, *27*, 365-371.

(48)   Handa, Y. P.; Lampron, S.; Oneill, M. L. *J. Polym. Sci. Pol. Phys.* **1994**, *32*,
        2549-2553.

(49)   Kamiya, Y.; Hirose, T.; Mizoguchi, K.; Terada, K. *J. Polym. Sci. Pol. Phys.*
        1988, *26*, 1409-1424.

(50)   Kamiya, Y.; Mizoguchi, K.; Hirose, T.; Naito, Y. *J. Polym. Sci. Pol. Phys.* **1989**,
        27, 879-892.

(51)   Shieh, Y. T.; Su, J. H.; Manivannan, G.; Lee, P. H. C.; Sawan, S. P.; Spall, W.
        D. *J. Appl. Polym. Sci.* **1996**, *59*, 695-705.

(52)   Watkins, J. J.; Mccarthy, T. J. *Macromolecules* **1994**, *27*, 4845-4847.

(53)   Watkins, J. J.; Mccarthy, T. J. *Macromolecules* **1995**, *28*, 4067-4074.

(54)   Kung, E.; Lesser, A. J.; McCarthy, T. J. *Macromolecules* **2000**, *33*, 8192-8199.

(55)   Cao, C., Ph. D. Thesis, University of Massachusetts, 2002.

(56)   Watkins, J. J.; Mccarthy, T. J. *Chem. Mater.* **1995**, *7*, 1991-&.

(57)   Watkins, J. J.; Blackburn, J. M.; McCarthy, T. J. *Chem. Mater.* **1999**, *11*, 213-215.

(58)   Newitt, D. M. e. a. *Thermodynamic Functions of Gases*: Butterworths Scientific Publications: London, 1956; Vol. 1.

CHAPTER 2

FABRICATION OF ANODIZED ALUMINUM MEMBRANES

2.1. Introduction

Anodization of aluminum has been commercially used for 80 years for protection and decoration purpose. An anodic oxide film is formed on the surface of aluminum when it is anodized in an electrolytic cell with proper electrolyte and electric current. It was already known in 1950 s that anodic oxide films on aluminum could exist in two forms: nonporous and porous oxide.[1,2]

A nonporous anodic aluminum oxide, which is also called barrier-type film, is prepared when the electrolyte does not dissolve the formed oxide film completely. Neutral boric acid solution, ammonium borate or tartrate aqueous solutions (pH 5-7), ammonium tetraborate in ethylene glycol, citric acid, malic acid, and glycolic acid are examples for this case. A porous anodic aluminum oxide, which is also called porous-type film, is prepared when the electrolyte partly dissolves the formed oxide film. Sulfuric acid, oxalic acid, phosphoric acid, and chromic acid are examples for this case.[3]

Contrary to the nonporous oxide, porous oxide has had limited industrial application for the protection of aluminum. The discovery of regular nanoporous structures[1,4] has attracted attention for potential applications such as magnetic recording media,[5,6] optical devices,[7] functional electrodes,[8,9] and display devices.

Constant efforts have been made to fabricate porous alumina with better regularity, which means more homogeneous pore size and better packing regularity of

20

pores. An important step to improve the regularity of pores was made by Masuda and coworkers.[10,11] They anodized an aluminum foil for more than 10 hours and removed the oxide film to leave well-ordered pits on the aluminum surface. Reanodization from this surface produced aluminum oxide with perfectly hexagonal-packed pores in long range order since the anodization started from these pits. This process can be repeated. This method has been modified by them and other groups.[12-18] The Masuda group has also developed the nano-indent method of pressing an aluminum surface with pre-patterned SiC which was formed by electron beam lithography.[13]

Anodized aluminum oxide membranes with specific pore sizes are commercially available. Whatman Co. is currently selling membranes with 200 nm diameter pores. It is noted that their 20 nm pore membrane has that size only at the top surface, presumably these are manufactured by narrowing the pores from 200 nm pores by reducing voltage during the anodization in a detaching step.[19]

As stated in chapter 1, preparing anodic aluminum oxide with less than 200 nm pore size is important for the study of the morphology of block copolymer. In this chapter the preparation of AAO membrane with that size is described. The procedure is based on the one developed by Masuda group: electropolishing, first anodization, chemical etching, second anodization, aluminum removal and pore widening (Figure 2.1). Detailed procedures are explained in the following sections.

2.2. Background

Electro-polishing of aluminum

1st Anodization
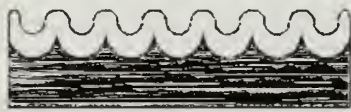
Chemical etching of alumina

2nd Anodization

Aluminum dissolving

Pore-opening

Figure 2.1. Procedure for well-ordered anodized aluminum membrane.

The mechanism of pore formation of porous-type anodic alumina film is not fully understood yet. There are some reviews on the mechanism of pore formation. According to Thomson and Wood, and Metzger *et al*, electropolishing provides a slightly scalloped surface of aluminum with an oxide film. which is composed of many pores that have several to tens of nanometer size diameters. as well as smoothing the surface macroscopically. During the anodization the initial pores are merged with each other to form major pores. The electric field and current density should be larger at the bottom of the pores than at other areas because of the thinner oxide film.

The pore formation during the anodization can be summarized as the equilibrium between oxide dissolution at the oxide/electrolyte interface and oxide growth at the metal /oxide interface (Figure 2.2). The oxide growth is due to the migration of oxygen containing ions. such as O^{2-}. OH^-. from the electrolyte through the oxide layer. and the oxide dissolution is due to the loss of Al^{3+} ions.
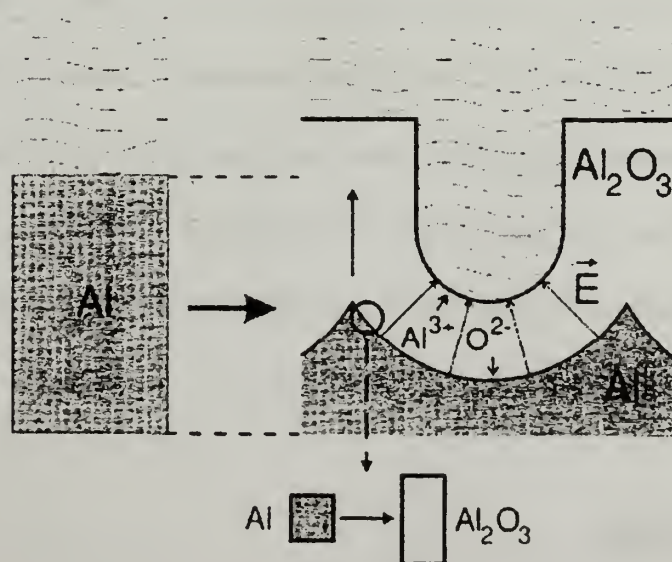
Figure 2.2. Pore formation during the anodization.[14]

At the aluminum/oxide interface. aluminum is oxidized to form aluminum ion. Al^{3+}. which migrates into the oxide film.

$$2Al(s) \rightarrow 2Al^{3+}(oxide) + 6e^-$$ (1)
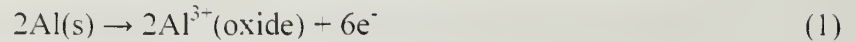
At the oxide/electrolyte interface. protons are produced by the hydrolysis of water and the dissociation of acid. competing with each other.

$$3H_2O(l) \rightarrow 6H^+(aq) + 3O^{2-}(oxide)$$ (2)

$$HC_2O_4^- (aq) \rightarrow C_2O_4^{2-}(oxide) + H^+(aq)$$ (3)
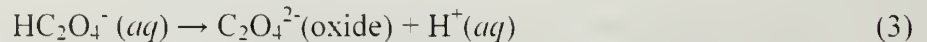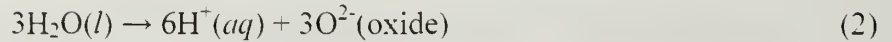
The protons can locally dissolve more oxide (equation (4)). or migrate to the cathode to form H_2 gas. completing the circuit (equation (5)).

$$Al_2O_3(s) + 3H^+(aq) \rightarrow Al^{3+}(aq) + 3H_2O(l)$$ (4)

$$6H^+(aq) + 6e^- \rightarrow H_2(g)$$ (5)
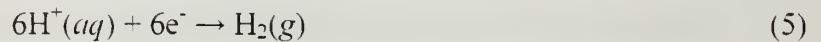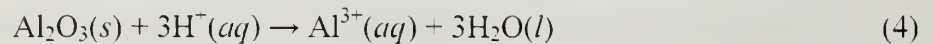
Oxide from equation (2) contributes to build sidewalls during the anodization. The reaction of equation (1) is faster than that of equation (4) to form pores. Equation (4) is the reaction that distinguishes the porous-type film from the barrier-type film. During the pore forming procedure. reaction of equation (4) occurs at the center of the bottom. where the electric field is higher than other areas due to the thinner oxide layer.

Metzger *et al* explained the formation of uniform pores by the provision of oxide at the intersection between sidewalls and the pore bottoms. At those area the reaction of equation (2) occurs. not that of equation (4).

2.3. Experimental

The electrochemical cell for anodization of aluminum is composed of an anode. a cathode. electrolyte solution. and a power supply (Figure 2.3). Platinum was purchased

from Aldrich and is used as the cathode. Aluminum foil with 99.99% and 99.999% purity were purchased from Aldrich or Alfa Aesar and used as the anode. Agilent DC E3616A and E3612A were used as power supplies for electropolishing and anodization, respectively.
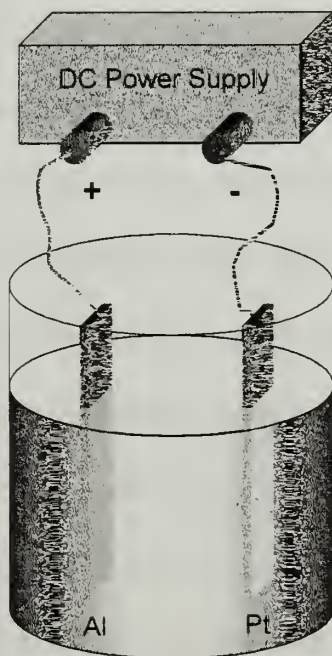
Figure 2.3. Electrochemical cell for the fabrication of AAO membrane.

Purchased aluminum foil was ground using sandpaper and rinsed with acetone, ethanol and then deionized water. It is important to make a smooth surface of aluminum by electropolishing before anodization for regular pore fabrication. This pretreated aluminum foil was electropolished in perchloric acid-ethanol solution (4:1 mixture of 70% perchloric acid and ethanol) at 20V for 10 minutes at 4 °C. The electropolished area of aluminum possessed a shiny surface. After electropolishing, the aluminum foil was rinsed with ethanol and deionized water.

This pretreated aluminum foil was moved to an electrochemical cell with 0.3M oxalic acid solution for the first anodization. The voltage ranged from 30V to 50V, and the temperature ranged from 4 °C to 15 °C. Voltages above 50V destroyed the aluminum foil during the anodization. The anodization time is between 6 and 12 hours.

The alumina film from the first anodization was removed by chemical etching, which is a procedure to dissolve oxide film selectively. The sample was dipped in a mixture of 0.2 M chromic acid and 0.4 M Phosphoric acid solution for 2 to 4 hours at 60 °C. The remaining aluminum was rinsed with deionized water.

The conditions for the second anodization were the same as the first anodization, including voltage and temperature. The anodization time is usually longer than the first anodization, between 8 to 20 hours, followed by rinsing with deionized water.

The sample at this step shows a long-range order with aluminum on one side. A membrane, which has open pores in both sides, can be obtained by dissolving the aluminum part with saturated mercuric chloride solution and pore-opening with 5% phosphoric acid solution. Saturated mercuric chloride was purchased from LabChem. Inc. After aluminum was dissolved, the remaining alumina film has thin barrier film on the side that was attached to the aluminum. This barrier film is dissolved by 5% phosphoric acid solution. The 5% phosphoric acid solution also can dissolve the wall of the pores, which leads to pore-widening.

2.4. Results

Figure 2.4 shows SEM images of oxide film after the first anodization and second anodization. The top surface of the oxide film after the first anodization shows

26
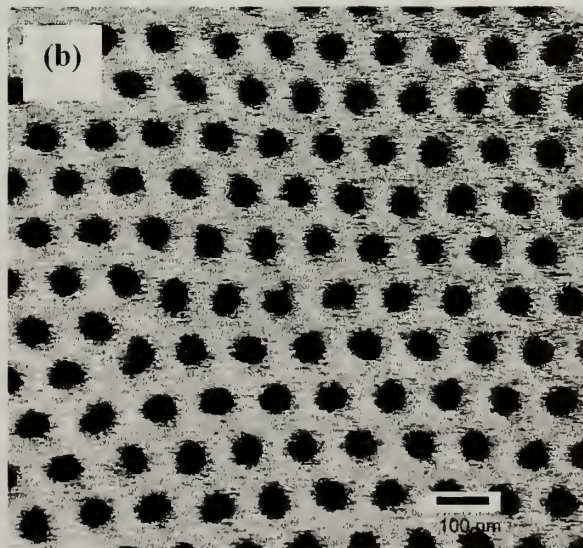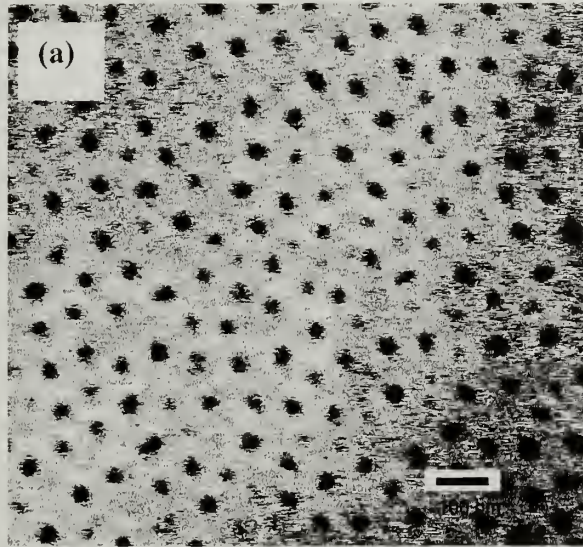
Figure 2.4. SEM images of AAO membrane surfaces after the first anodization (a), and the second anodization (b).

randomly located pores. and the surface of the oxide film after the second anodization shows well-ordered pores. It is noted that this reanodization procedure provides much improved regularity.

The size of the pores (D_p) and the distance between the pores (pore-to-pore distance. D_c) are two factors that can characterize AAO membrane (Figure 2.5). The pore size is the determining factor of commensurability of block copolymer inside the pores. The pore-to-pore distance can be important factor for potential purpose such as magnetic storage. and determines the maximum pore size during the pore-widening procedure.
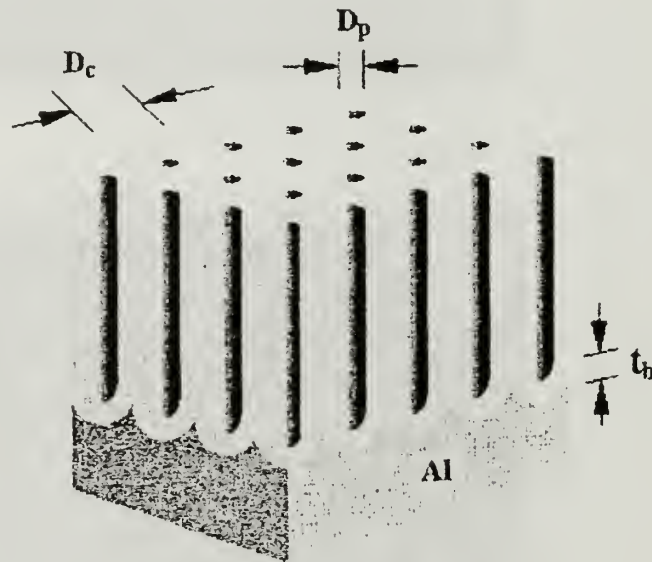
Figure 2.5. Ideal hexagonal porous alumina film.

Figure 2.6 shows SEM images of anodic alumina film after the second anodization at 4 °C at 30V. 40V. and 50V. The pore size was measured as 20 nm. 30 nm. and 40 nm. respectively, and the pore-to-pore distance was measured as 80 nm, 100 nm,

28

and 120 nm, respectively. In the case of anodization at 4 °C, both the pore size and the pore-to-pore distance increase as the voltage increase.

Figure 2.7 shows SEM images of anodic alumina film after the second anodization at 15 °C at 30V, 40V, and 50V. The pore size was measured to be 50 nm in every case, and the pore-to-pore distance was determined to be 80 nm, 100 nm, and 120 nm, respectively. In the case of anodization at 15 °C, the pore size was not affected by the voltage and the pore-to-pore distance increased as the voltage increased, similar to the case of 4 °C.

The different behavior of determining pore size at different temperature can be explained by measuring the current of the electrochemical cell. The current has been monitored during the anodization procedures. The current increases quickly right after the anodization starts, and decreases after several minutes, then stabilizes until the anodization fails. Figure 2.8 (a) shows the relationship between the current and the pore size, and Figure 2.8 (b) shows the relationship between the voltage and the pore-to-pore distance. The current is proportional to the pore size until the pore size reaches its maximum, and the voltage is proportional to the pore-to-pore distance in this range. As stated in section 2.2, the electric current plays an important role in the pore forming process by dissolving the oxide layer. Therefore, higher current produces larger pore size within a certain range.

After the second anodization, the aluminum is dissolved in a saturated mercuric chloride solution. The remaining anodic alumina has a thin barrier-film left on the aluminum-attached side. This film can be removed by 5% phosphoric acid solution. Figure 2.9 shows the anodic alumina after dissolving aluminum (a), and after dissolving

the thin barrier-film (b). Figure 2.10 shows an example of an anodic alumina membrane in different perspective.

In these experimental conditions, the maximum pore size was 50 nm after the second anodization. Therefore, an additional procedure was needed to produce anodic alumina membranes with greater than 50 nm pore size. The anodic alumina samples were treated with 5% phosphoric acid at 30 °C for between 20 minutes and 60 minutes, and the final pore size expanded up to 100 nm, proportional to the time. Figure 2.11 shows a result of pore-widening. The pore size was enlarged from 50 nm to 75 nm by treating with 5% phosphoric acid solution for 20 minutes.
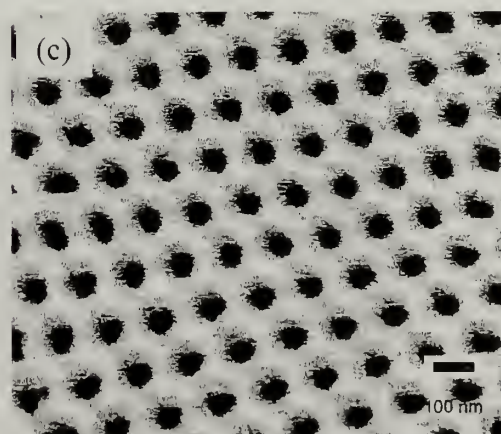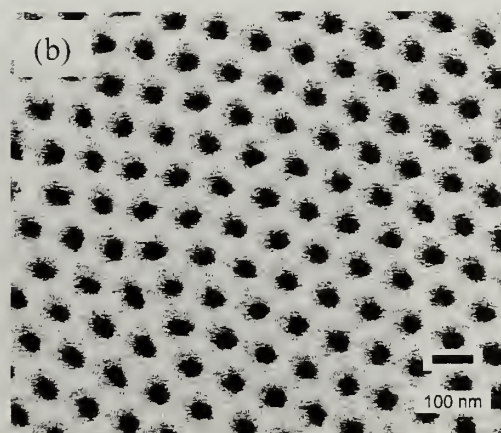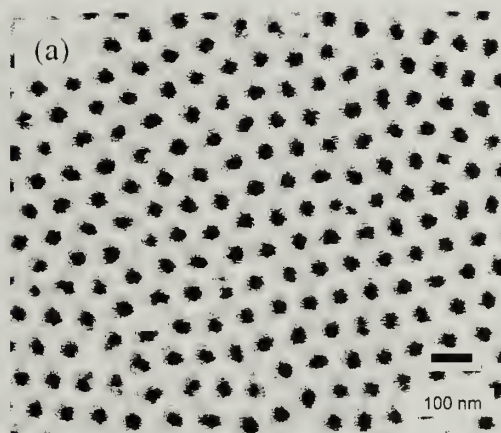
Figure 2.6. SEM images of AAO membrane surfaces under different voltage conditions at 4 °C in 0.3M oxalic acid solution at 30V (a), at 40V (b), and 50V (c).
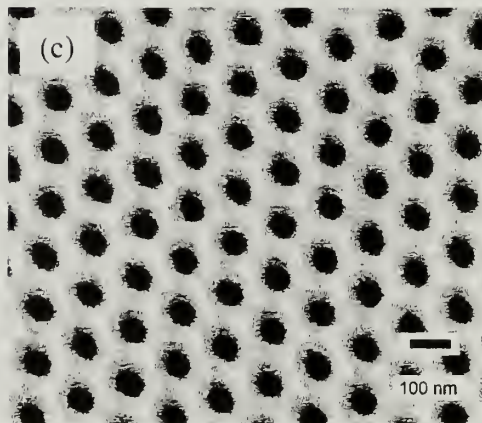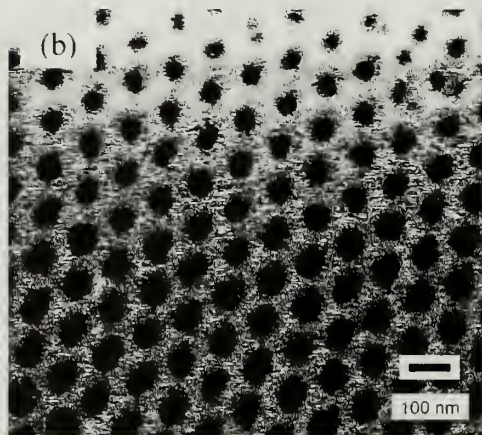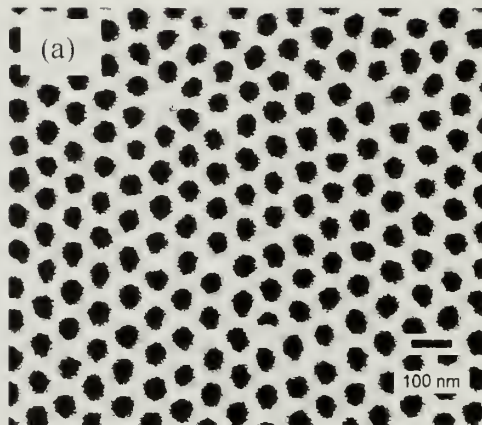
Figure 2.7. SEM images of AAO membrane surfaces under different voltage conditions at 15 °C in 0.3M oxalic acid solution at 30V (a), at 40V (b), and 50V (c).

(a)

(b)
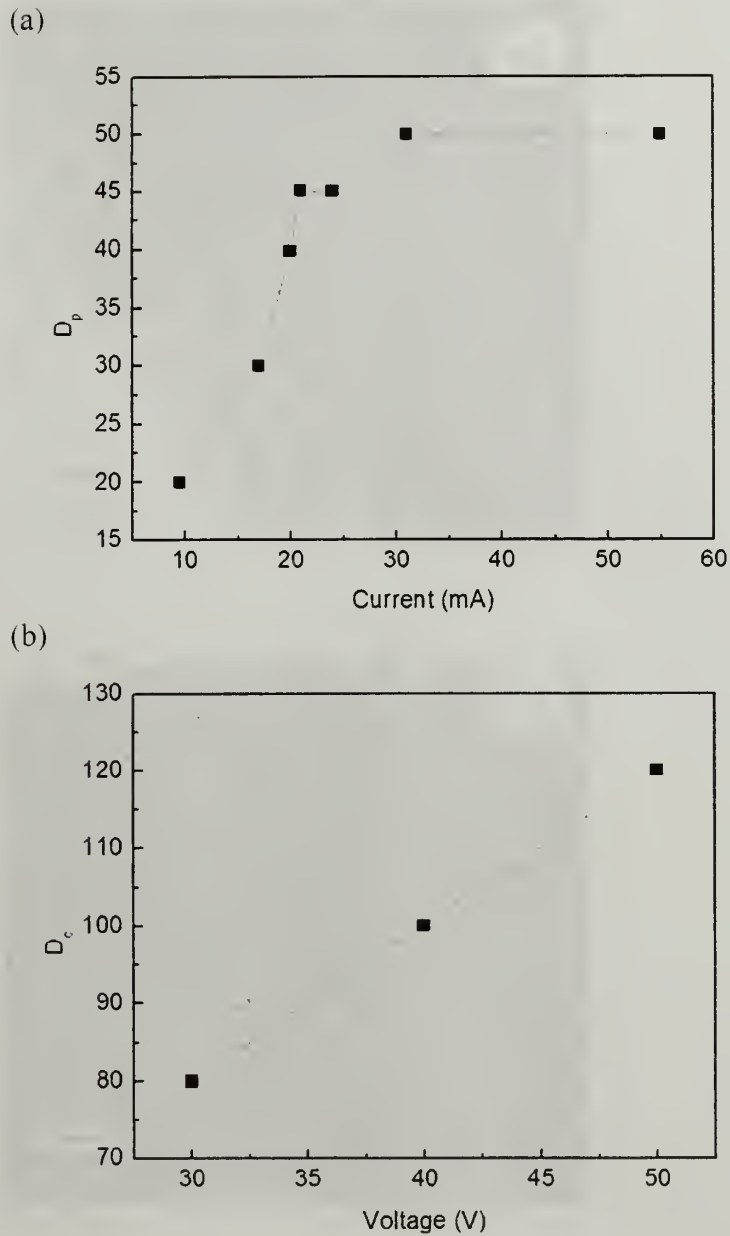
Figure 2.8. (a) Variation of pore diameters of AAO membranes as a function of current. (b) variations of pore-to-pore distances as a function of voltage.
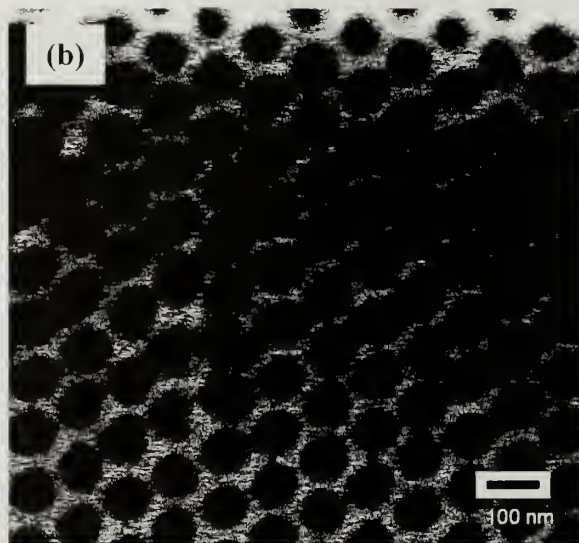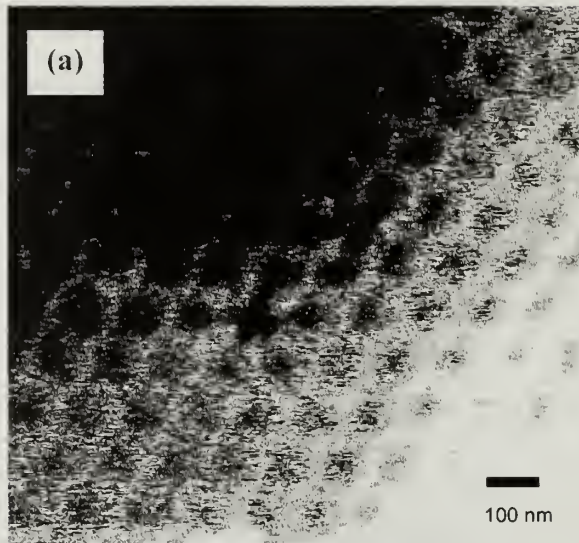
Figure 2.9. SEM images of AAO membrane surfaces before pore-opening (a) and after pore opening (b) using 5% phosphoric acid solution for 15 min.
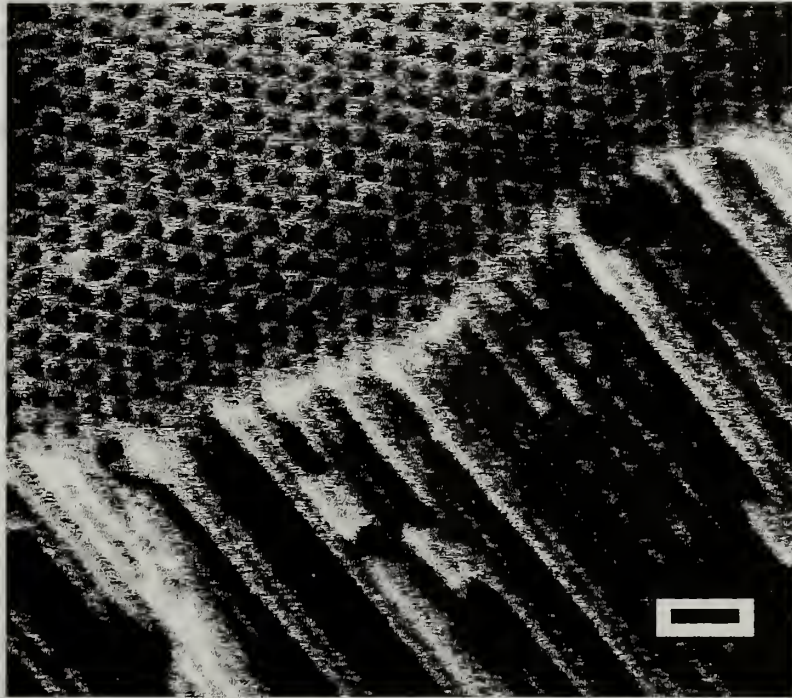
Figure 2.10. SEM image of an AAO membrane after dissolving aluminum using saturated mercuric chloride solution. Scale bar: 200 nm.
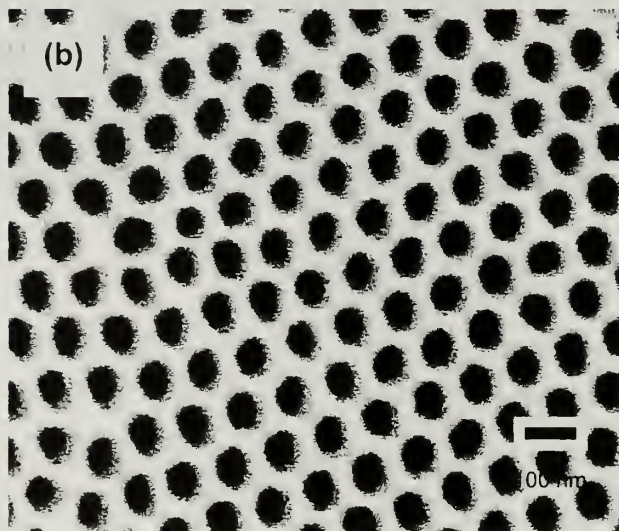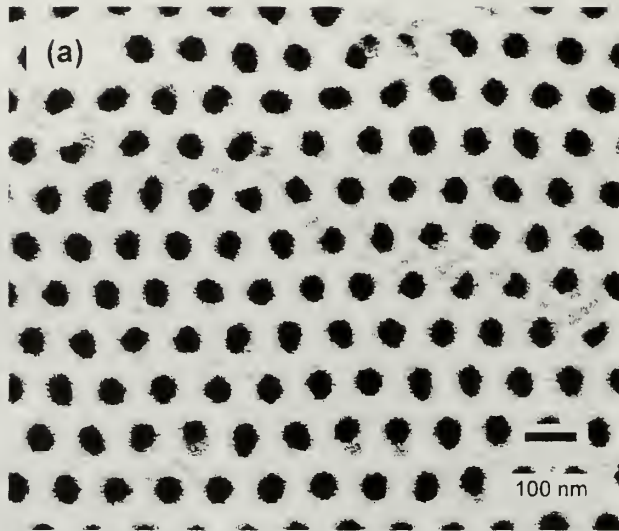
Figure 2.11. Pore widening procedure using 5% phosphoric acid solution for 20 min at 30 °C. (a) SEM image of AAO surface before pore-widening procedure. (b) SEM image of AAO surface after pore-widening procedure.

2.5. References

(1)   Keller, F.; Hunter, M. S.; Robinson, D. L. *J. Electrochem. Soc.* **1953**, *100*, 411-419.

(2)   Franklin, R. W. *Nature* **1957**, *180*, 1470-1471.

(3)   Diggle, J. W.; Downie, T. C.; Goulding, C. W. *Chem Rev* **1969**, *69*, 365-&.

(4)   Thompson, G. E.; Furneaux, R. C.; Wood, G. C.; Richardson, J. A.; Goode, J. S. *Nature* **1978**, *272*, 433-435.

(5)   Kawai, S.; Ueda, R. *J. Electrochem. Soc.* **1975**, *122*, 32-36.

(6)   Shiraki, M.; Wakui, Y.; Tokushima, T.; Tsuya, N. *IEEE Trans. Magn.* **1985**, *21*, 1465-1467.

(7)   Saito, M.; Kirihara, M.; Taniguchi, T.; Miyagi, M. *Appl. Phys. Lett.* **1989**, *55*, 607-609.

(8)   Miller, C. J.; Majda, M. *J. Am. Chem. Soc.* **1985**, *107*, 1419-1420.

(9)   Tierney, M. J.; Martin, C. R. *J. Electrochem. Soc.* **1990**, *137*, 3789-3793.

(10)   Masuda, H.; Fukuda, K. *Science* **1995**, *268*, 1466-1468.

(11)   Masuda, H.; Satoh, M. *Jpn J Appl Phys 2* **1996**, *35*, L126-L129.

(12)   Masuda, H.; Hasegwa, F.; Ono, S. *J. Electrochem. Soc.* **1997**, *144*, L127-L130.

(13)   Masuda, H.; Yamada, H.; Satoh, M.; Asoh, H.; Nakao, M.; Tamamura, T. *Appl. Phys. Lett.* **1997**, *71*, 2770-2772.

(14)   Jessensky, O.; Muller, F.; Gosele, U. *Appl. Phys. Lett.* **1998**, *72*, 1173-1175.

(15)   Jessensky, O.; Muller, F.; Gosele, U. *J. Electrochem. Soc.* **1998**, *145*, 3735-3740.

(16)   Li, A. P.; Muller, F.; Birner, A.; Nielsch, K.; Gosele, U. *J. Appl. Phys.* **1998**, *84*, 6023-6026.

(17)   Li, A. P.; Muller, F.; Birner, A.; Nielsch, K.; Gosele, U. *Adv. Mater.* **1999**, *11*, 483-+.

(18)   Li, F. Y.; Zhang, L.; Metzger, R. M. *Chem. Mater.* **1998**, *10*, 2470-2480.

(19)   Furneaux, R. C.; Rigby, W. R.; Davidson, A. P. *Nature* **1989**, *337*, 147-149.

CHAPTER 3

POLYSTYRENE-POLYBUTADIENE BLOCK COPOLYMER NANORODS

3.1. Introduction

The microphase-separated phases of block copolymers have been widely studied

from both theoretical and experimental perspectives, and with regard to various

applications. The factors which determine the phases of a block copolymer include the

interaction parameter χ and the degree of polymerization N. The simplest form of block

copolymer is a diblock copolymer, which is a linear polymer composed of two different

blocks that can form various morphologies in the bulk: body-centered cubic spheres,

hexagonally-packed cylinders, bi-continuous gyroids, and alternating lamellae.[1]

These various morphologies can acquire additional possibilities by locating the

block copolymers under certain boundary conditions: novel structures can form due to the

confinement. The most widely studied confinement is a one-dimensional surface type,

either on a flat surface with open air or between parallel walls. Böltau et al. showed that

the structures of polymer blends can be determined by the pre-patterned surface

structure.[2] Lambooy et al. investigated the structure of lamella-forming block copolymers

confined on silicon wafers.[3] Another confined structures, such as cylindrical pores or

spheres, can be useful for special purposes.

When block copolymers are confined geometrically, their structures should be

affected by the confinement and surface interactions. For example, when a symmetric

block copolymer is introduced into cylindrical pores, a concentric ring structure is

expected, owing to the shape of the pore. In this case, there are additional factors that need to be considered over those for a bulk block copolymer. First, the interaction between polymer segments and the alumina surface is expected to play a roll in determining phase behavior. Second, the commensurability of the block copolymer needs to be considered because a block copolymer is located in a confined pore, the diameter of which can affect the block copolymer morphology.

One of the fundamental scientific interests of microphase-separated block copolymers in confined systems lies in the breaking of symmetry in the structure and the role of commensurability, as introduced in Chapter 1. Examples of block copolymers in one dimensional confinement, sandwiched between two planes, and two dimensional confinement, confined in trough were explained. Cylindrical confinement is of particular interest since many situations are met in nature where such confinement influences phase behavior. In addition to confinement, cylindrical nanopores force a curvature on the morphology. So both commensurability between the pore diameter and natural period and the imposed curvature can strongly influence the morphology of the confined system.

Molecular modeling or computer simulation has been a powerful tool for predicting the structure of block copolymers in confined geometry. The number of interaction pairs between segments and/or surface inside confinement is much smaller than that of bulk, which reduces the calculation time. He *et al.* showed that a symmetric block copolymer forms stripe, circle, core-multishell, and multibarrel-layer structure depending on the boundaries using a Monte Carlo simulation method.[4] Sevink *et al.* predicted that a symmetric block copolymer can form two different structures inside cylindrical pores depending on the interaction between wall and polymer using a dynamic

density functional method: slab morphology for neutral interaction and dartboard morphology for stronger preferential interaction.[5] Li *et al.* expanded the possible structure of diblock copolymers inside cylindrical pores using self-consistent mean field theory.[6] (Figure 3.1) Yu et al. predicted structures of asymmetric diblock copolymers inside cylindrical pores using a lattice model.[7] (Figure 3.2)
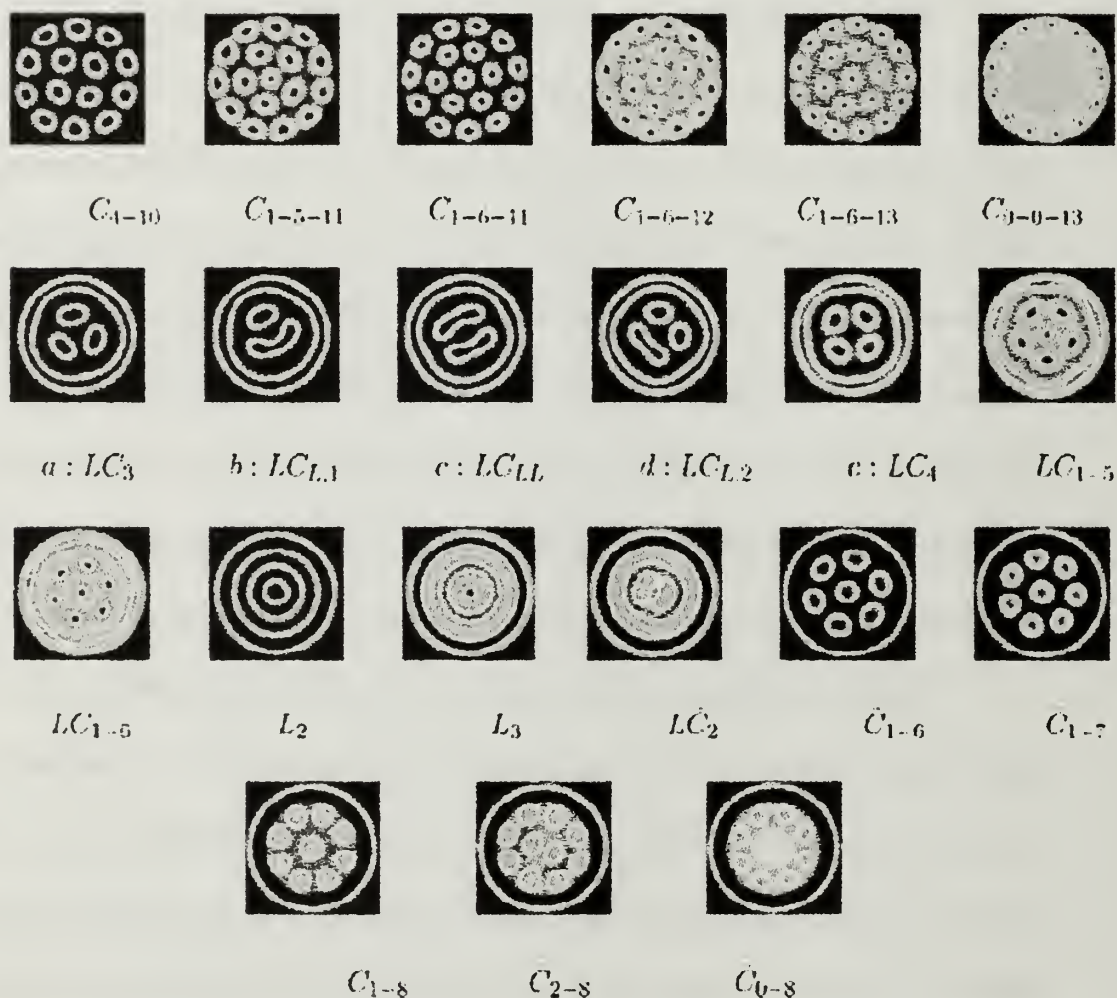
Figure 3.1. Monomer density plots of the 21 nanostructured phases formed in the 8.5 Rg radius pores.[6]
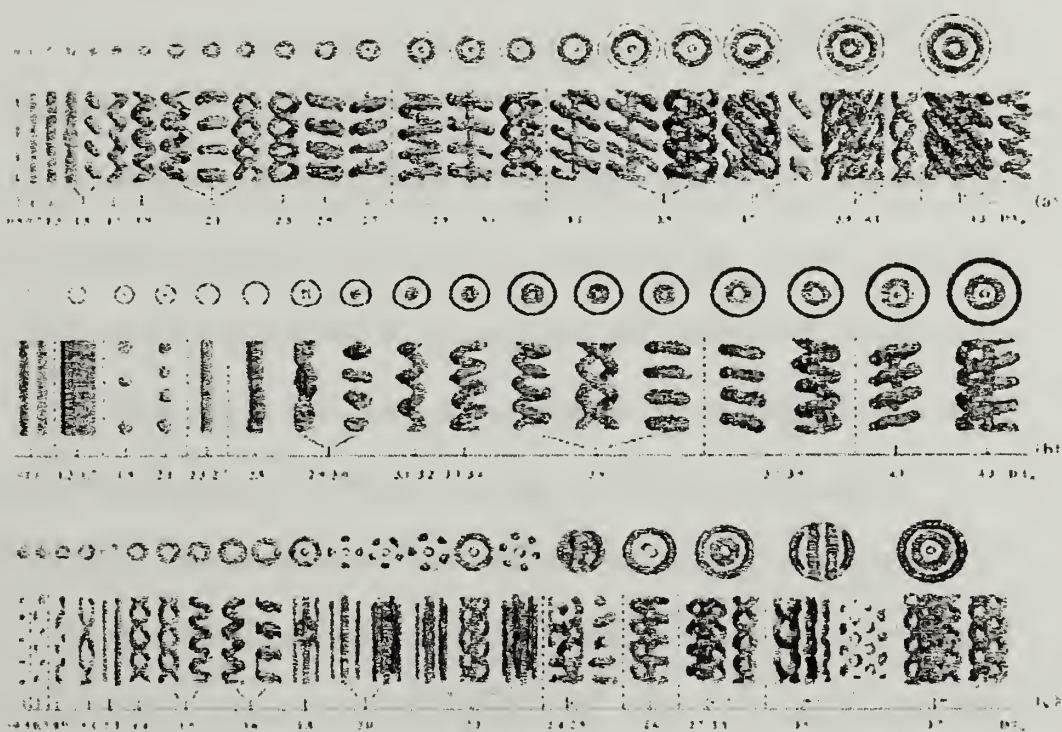
Figure 3.2. Self-assembled morphologies as a function of the ratio D/L_0 for different wall-polymer interactions.[7]

The purpose of this chapter is to investigate the structures of diblock copolymers inside cylindrical nanopores. Polystyrene-*b*-polybutadiene (PS-*b*-PBD) nanorods were prepared using membranes of various size pores, including both commercial and self-prepared membranes. It is noted that the surface energy of PBD is lower than that of PS (Table 4.1) and neither has preferential interaction with the alumina surface. Therefore, the research was focused on their commensurability, not the effect from surface. The morphology of diblock copolymers, both symmetric and asymmetric, confined in cylindrical nanopores, is addressed. At some ratios of the pore diameter to the natural period of the copolymer, new morphologies are found that cannot be accessed by any other means and have potential use for the fabrication of isolated nanostructures.

3.2. Experimental

Anodized aluminum membranes. Anodisc 0.2 μm, were purchased from Whatman, Inc. These membranes are free-standing discs with a diameter of 13 mm and a thickness of 60 μm. The membranes are comprised of straight, cylindrical pores, oriented normal to the disc surface. The pores range in diameter from ~100 nm to ~350 nm. Some pores impinge on one another forming larger, non-circular pores.

Symmetric and asymmetric diblock copolymers of styrene and butadiene (PS-*b*-PBD) were purchased from Polymer Sources. The asymmetric PS-*b*-PBD had a number average molecular weight, M_n, of 42,000 and a polydispersity, M_w/M_n, of 1.03 with a volume fraction of ~0.3 PBD. The bulk morphology consists of PBD cylinders in a PS matrix with a cylinder-to-cylinder distance of ~29.1 nm, as measured by small angle X-ray scattering (SAXS). The symmetric PS-*b*-PBD had a M_n of 42,000 with M_w/M_n of 1.03 with a volume fraction of ~0.5 PBD. The bulk morphology was lamellar with an equilibrium period of ~29.6 nm (SAXS).

Figure 3.3 shows a schematic diagram of the process used to introduce the copolymer into the cylindrical alumina pores. Films (~15 μm in thickness) of the copolymers were solvent cast from toluene solutions onto glass slides and dried. The aluminium oxide membrane was then placed on top of the copolymer film. The assembly was heated to 125 °C, which is above the glass transition temperatures of both blocks. The copolymer melt entered into the pores of the membrane via capillary action. After annealing for 24 h under vacuum, the copolymer/membrane assembly was quenched to room temperature. The alumina membrane was removed using 5 *wt*% sodium hydroxide (water/methanol-8v:2v), leaving an array of copolymer nanorods protruding from the
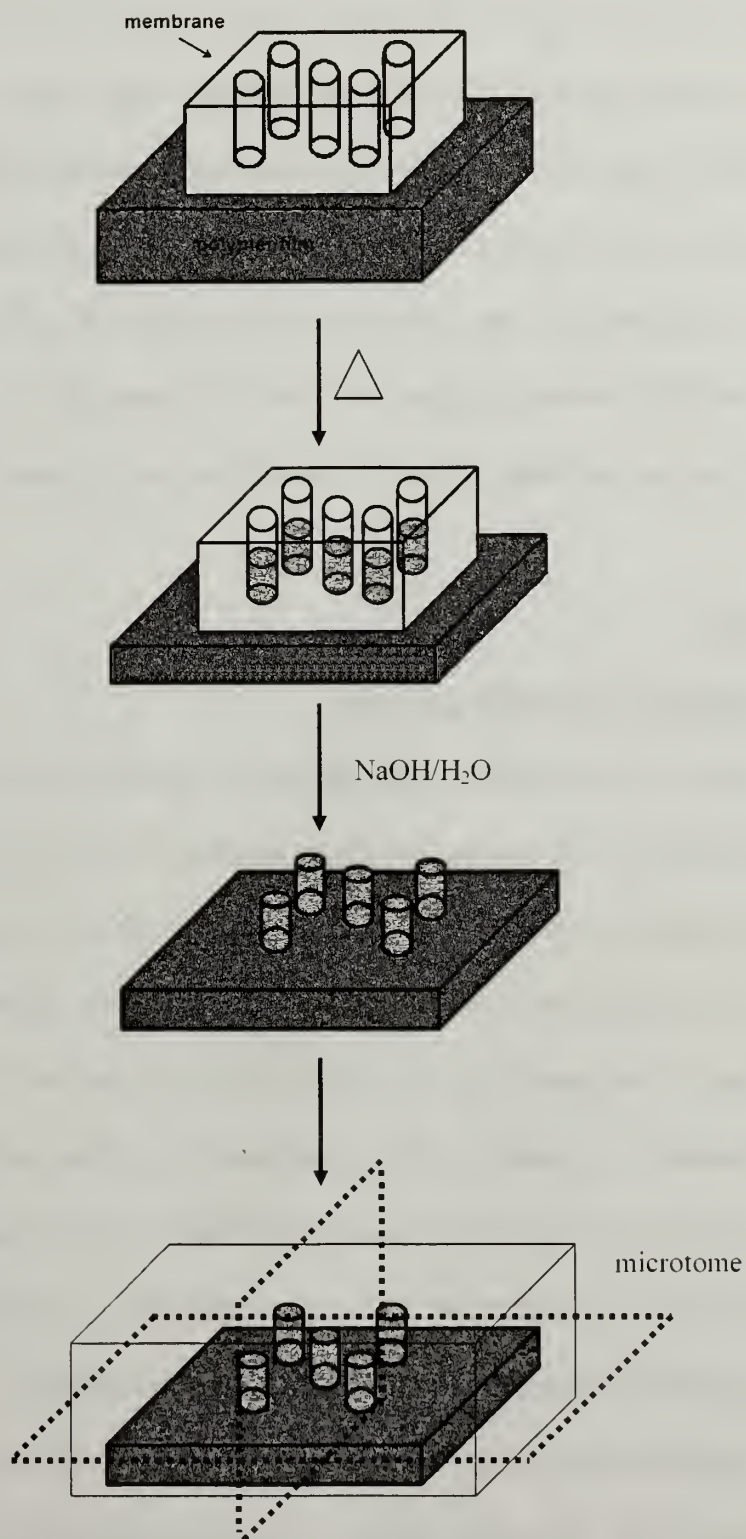
Figure 3.3. Preparation of block copolymer nanorods using AAO membrane.

copolymer film like the bristles of a brush.[8] The morphology of the copolymer nanorods was investigated using a JEOL 6320 model scanning electron microscope at an accelerating voltage of 5 kV. Bright field transmission electron microscopy (TEM) studies were conducted with a JEOL 100CX TEM operating at an accelerating voltage of 100 kV. To prepare TEM specimens. the copolymer film with protruding nanorods was stained with OsO_4. embedded in an epoxy resin. and cured at 60 °C for 24 h. Ultrathin sections were prepared using a Leica Ultracut microtome equipped with a diamond knife.

3.3. Results

3.3.1. Formation of PS-*b*-PBD nanorods

Figure 3.4 shows SEM micrographs of the asymmetric copolymer nanorods after complete removal of the alumina membrane template. As can be seen. the surfaces of the nanorods are smooth and of uniform length. The nanorods have a high aspect ratio, ~ 15:1. and after being freed from the nanoporous template, the nanorods could not stand perpendicular to the remaining copolymer film. but collapsed onto each other. When shorter columns (~ 5:1 aspect ratio) were prepared by reducing the time allowed for the copolymer to be pulled into the nanopores. individual copolymer nanorods could be observed (as shown in Figure 3.4). The surface layer of the copolymer nanorods was PBD (as discussed later). Since PBD has a glass transition temperature ~ - 95 °C, the surfaces of the nanorods are tacky at room temperature and the nanorods are seen to cluster together at their tips, like stacks of wheat. At higher magnifications, the top surfaces of the columns are dark. suggesting a depression in center of the nanorod ends.
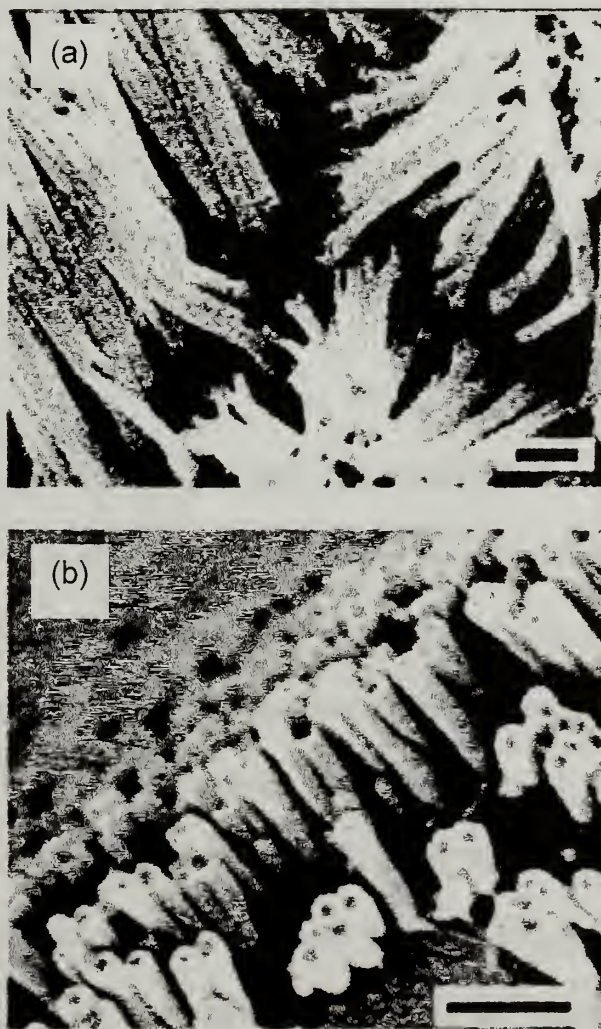
Figure 3.4. SEM micrographs of PS-*b*-PBD nanorods after removing alumina membrane
Scale bars: 500 nm (a) and 1 μm (b).[9]

This depressed center is consistent with a meniscus at the end of the nanorod, indicating that the copolymer wet the pore walls.

The generation of the nanorods uses capillary force to drive the copolymer melt into the cylindrical nanopores. The capillary force originates from a reduction in free energy by replacing the air/wall interface with a copolymer/wall interface. If the capillary force is positive, i.e. if the contact angle between the copolymer melt and the capillary wall is less than 90°, the copolymer spontaneously fills the capillary.[10] The maximum height the copolymer melt can rise within the capillary can, to a first approximation, be obtained by[11]

$$h_{max} = (2\ \gamma_{copolymer/air}\ \cos\theta)\ /\ (\rho g r)$$ (1)

where h_{max} is the maximum height, $\gamma_{copolymer/air}$ is the surface tension at the polymer/air interface, θ is the contact angle at the copolymer/capillary wall interface, ρ is the density of the copolymer, g is the gravitational constant, and r is the pore radius. The contact angle, estimated from the meniscus seen in the cross-sectional TEM image (discussed later), is ~ 80°. The surface tension of polybutadiene is ~ 30 mN/m. Using a PS-b-PBD density of 0.95 g/cm^3 and pore diameter 200 nm, a maximum height of 11.2 m is obtained from Equation 1. This result indicates that the length and aspect ratio of the copolymer nanorods may be made quite large.

The time required to fill the nanopores with the copolymer can be estimated by[10,11]

$$t = 2\eta z^2\ /\ (R\ \gamma_{copolymer/air}\ \cos\theta)$$ (2)

where t is the time, η the viscosity of the copolymer melt, z is the length of the capillary, and R the hydraulic radius (the cross-sectional area of a stream divided by the wetted

perimeter, here $R = 0.5\,r$). The viscosity of PS-*b*-PBD is about 10^6 Pa·s.[11] According to

Equation 2, t is ~ 26 h for the copolymer melt to fill the cylindrical pores to a height of ~

5 μm. It should also be noted that in the above calculation, the microphase separation of

the block copolymer melt was not considered and the PS-*b*-PBD is in the strong

segregation limit. The microphase separation should retard or even stop the flow of the

copolymer melt into the nanopores. Taking these points into consideration, the calculated

time is in remarkably good agreement with the actual time of 24 h used experimentally.

3.3.2. Symmetric PS-*b*-PBD nanorods

The morphology of symmetric block copolymer is expected as multibarrel-layers,

with a concentric ring structure normal to the axis cut. Concentric structures with

commensurate condition inside cylindrical pores are illustrated in Figure 3.5. It is noted

that the phase in the middle is the same as the outermost phase when D/L_0 is an even

number and the phase in the middle is different from the outermost phase when D/L_0 is an

odd number.

a)   b)

$2L_0$ $3L_0$

$D/L_o = 2$ $D/L_o = 3$
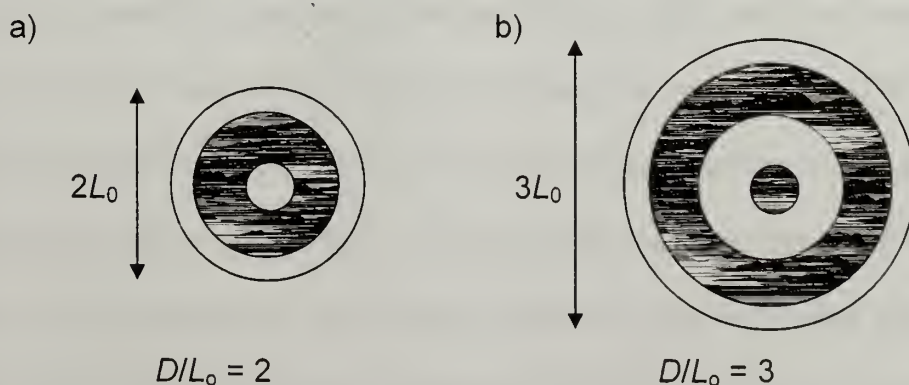
Figure 3.5. Schematic illustrations of expected structure of bulk lamellar-forming block
copolymers inside cylindrical pores under commensurate condition. a) In case of $D/L_0 = 2$, the number of cylinders becomes 2. b) In case of $D/L_0 = 3$, the number of cylinders
becomes 3.

Figure 3.6 shows TEM cross-sectional images of samples, microtomed normal to the nanorod axis and along the nanorod axis, for nanorods of symmetric PS-*b*-PBD s. Alternating dark (PBD) and bright (PS) lines parallel to the nanorod axis were observed from the view along the nanorod axis (Figure 3.6 (a)), with PBD preferentially located at the interface with the pore wall. When the lamellar PS-*b*-PBD nanorods were cut normal to the nanorod axis, a morphology composed of concentric rings was seen, as shown in Figure 3.6 (b). The outermost ring in contact with the pore wall was PBD, consistent with the other cross-section. These results indicate that under this cylindrical confinement, where the diameter of the confining pore is large in comparison to the period, the symmetric PS-*b*-PBD copolymer forms a concentric multi-cylinder or multi-barrel morphology, with one component preferentially segregated to the walls. This result is consistent with the molecular simulation results introduced in section 3.1.

Due to the variation in pore diameter of the commercial membrane, a morphology change was observed as the pore diameter changed, as shown in Figure 3.7. The outermost layer contacting the pore wall was always PBD. However, the phase in the center could be either PS or PBD, depending on the pore diameter, indicating the number of PS or PBD layers, as demonstrated in Figure 3.5. Figure 3.8 shows a plot of the number of cylinders as a function of the ratio of the pore diameter to the equilibrium period of the copolymer in the bulk, D/L_0. As the pore diameter decreases, the number of rings decreases uniformly, and the concentric ring morphology with an outermost PBD layer is maintained. However, the number of rings undergoes a series of discrete decreases from $n + 1$ to n cylinders where n is an integer. The apparent repeat period is measured by dividing the diameter of the nanorods by the number of periods. For the

Figure 3.6. TEM cross-sectional images of lamellar PS-*b*-PBD nanorods. (a) View along the nanorod axis (b) View normal to the nanorod axis. Scale bars: 200 nm.[9]

Figure 3.7. TEM images of bulk lamellar-forming PS-*b*-PBD structures in pores of various diameter. Scale bars: 100 nm.[9]
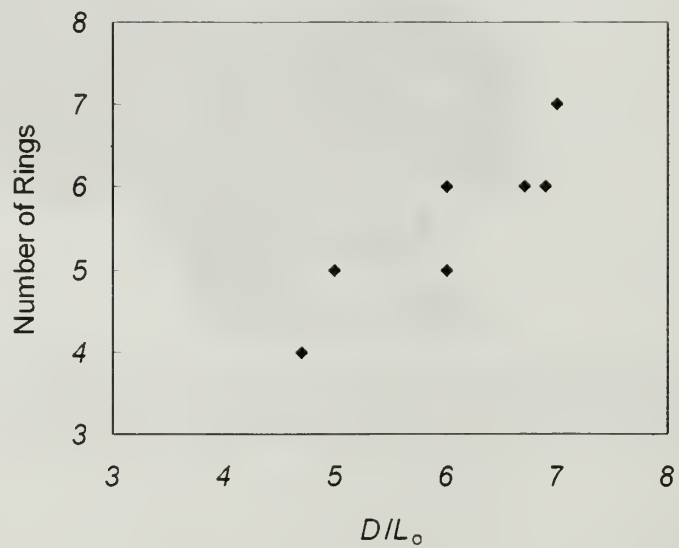
Figure 3.8. Number of cylinders vs. pore diameter normalized by the equilibrium repeat period.

TEM images shown in Figure 3.7, all the measured apparent repeat periods are greater than the bulk equilibrium period of 29.1 nm, and a maximum of ~44 nm is measured when the number of cylinders is four and a minimum of ~32 nm when the number of cylinders is seven. This result indicates that the confinement causes a perturbation of the fundamental period of the copolymer and, the smaller the pore, the more significant is the perturbation. This, of course, must be the case, since the confinement can be distributed over more layers in the thicker nanorods and the amount of the distortion to each period decreases with an increasing number of layers.

A novel morphology forms in the pores when the pore diameter is made smaller than those of commercial membranes, becoming comparable to the equilibrium period L_0 and when D/L_0 is not an integer (i.e. incommensurate). TEM images of lamellar PS-b-PBD (L_0 = 17.6 nm) in 45 nm diameter pores (D / L_0~ 2.6) are shown normal to and along the pore axes (Figures 3.9 (a) and (c), respectively). Here, D and L_0 are incommensurate. With planar surfaces, a compressed lamellar morphology would be seen. However, in the cylindrical geometry, the high degree of curvature imposed on the planar lamellae morphology produces a fundamental change in the structure. Normal to the rod axis, concentric layers are observed with PBD located at the centers and walls of the nanorods. Along the axes of the nanorods, a stacked PS lamellar structure is seen, with a central spine and outer edges of PBD. Thus, a morphological transition from a lamellar to a stacked disc or torus-type structure is seen. This morphology, forced on the block copolymer by curvature and incommensurability represents a fundamentally new morphology that is not accessible by other means.

Figure 3.9. TEM cross-sectional images of bulk lamellar-forming PS-*b*-PBD nanorods. (a. b) Views across nanorod axis: (c. d) Views along the nanorod axis: (a. c) $D/L_0 = 2.6$: and (b. d) $D/L_0 \sim 1.9$. Scale bars: 50 nm.[12,13]

As the D/L_0 further decreases. another transfer in morphology occurs. Shown in Figures 3.9 (b) and (d) are TEM images of PS-b-PBD (L_0 = 17.6 nm) in 45 nm pores (d/L_0~1.9). Here. only a central core of PS. surrounded by a layer of PBD. is observed. The formation of only one period in the pore of d/L_0~1.9 requires a significant deformation of the block copolymer chains but. due to the strong immiscibility of PS and PBD and favorable interfacial interactions of PBD with the pore walls. a lamellar morphology persists.

3.3.3. Asymmetric PS-b-PBS nanorods

Figure 3.10 (a) shows the cross-sectional TEM images both along the nanorod axis and normal to the nanorod axis of bulk cylinder-forming PS-b-PBD confined within the cylindrical nanopores. A meniscus is clearly seen at the end of the copolymer nanorods. which is the signature of the capillary rise. Within the nanorods. the microphase-separated morphology of the copolymer was well developed. It can be seen that the PBD preferentially segregated to both the interface with the nanopore wall and the free surface. highlighting the edges of the columns. Within the columns. the PBD cylinders appeared as dark lines parallel to the axes of the nanorods. At the top of the nanorods is an air surface and a change in the orientation of the cylindrical domains occurred. as evidenced by the dark dots for the PBD cylinders.

Figure 3.10 (b) shows a cross-sectional TEM image for the PS-b-PBD nanorods cut normal to the nanorod axis. A rim of PBD is seen around the edges of the sections. which is consistent with the sections cut along the nanorod axis. and within the rim are circularly shaped PBD domains. These results indicate an orientation of PBD cylinders
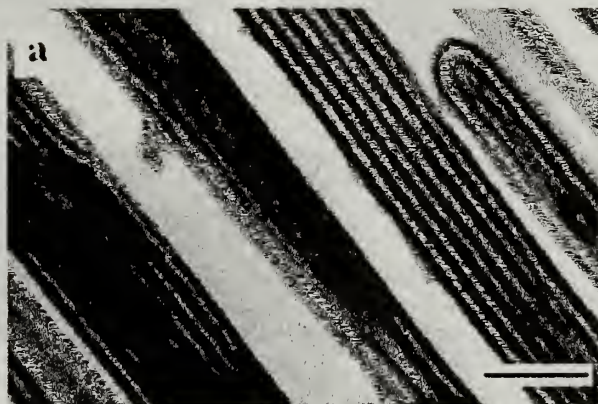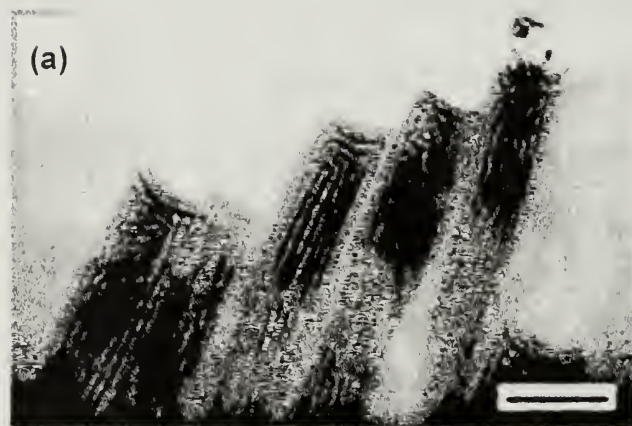
Figure 3.10. TEM cross-sectional images of bulk cylinder-forming PS-*b*-PBD nanorods. (a) Along the nanorod axis. (b) Normal to the nanorod axis. Scale bars: 200 nm.[9]
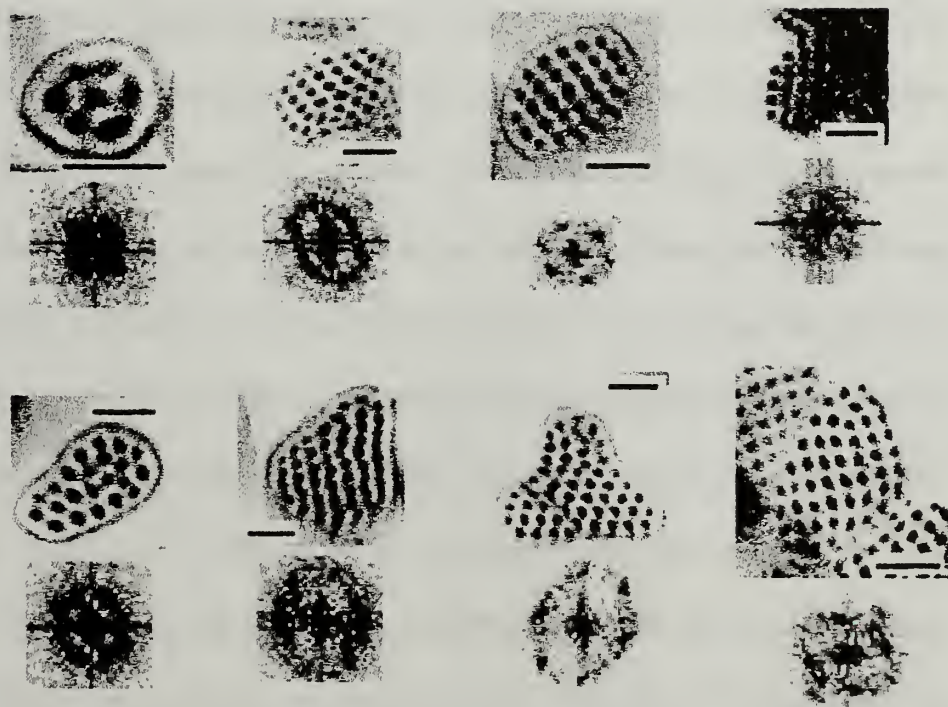
Figure 3.11. TEM cross-sectional images of bulk cylinder-forming PS-*b*-PBD nanorods in different diameter along with the corresponding fast Fourier transforms. Scale bars: 100 nm.[9]

along the pore axes. As stated in chapter 3.3.2. the shape and size of the nanopores of the commercial alumina template are not uniform. Consequently, the structure of the copolymer nanorods also varied in different pores. This variation provided a means to probe the identical sample under different confinement conditions. Figure 3.11 shows some of the morphologies observed for the bulk cylinder-forming PS-*b*-PBD confined within the nanopores having different geometry. For each image, a fast Fourier was obtained to analyze the packing of the cylindrical microdomains. It can be seen that the hexagonal packing of the cylinders was maintained but some deformation of the microdomains and grain boundaries were seen due to the shape of the pores. However, for nearly circular pores, only one grain was found for the cylindrical microdomains. As the pore diameter decreased, fewer cylinders were confined in the pores, and for a pore diameter of about 120 nm ($D/L_0 \sim 4.1$), only seven cylinders were formed within the pore.

If the pore diameter decreases to ~56~66 nm ($D/L_0 = \sim1.9$ - 2.3), a single PBD cylinder domain in the center and a PBD rim contacting the pore wall were observed, as shown in Figure 3.12 (a) and (c). Viewing along the nanorod axis, Figure 3.12 (a), shows clearly an undulation along the interface of PS domains with PBD center and rim. This undulation arises from the severe geometric confinement and is a precursor for a change in the morphology. For the cases with pore diameters of ~33 - 45 nm ($D/L_0 = 1.1 \sim 1.5$), the cross-sectional TEM images in Figure 3.12 (b) and (d) show that the microphase-separated morphology of the copolymer is well-developed with the lower surface-energy PBD domain still located at the pore walls, highlighting the edges of the nanorods. However, the alignment of cylindrical domains along the rod axis, which occurs when $D/L_0 > 4.1$, is no longer observed. Rather, dark lines are seen at a constant angle with

respect to the nanorod axis, indicating that PBD forms a helical structure, while maintaining contact with the pore walls. The pitch is measured to be ~30 nm, quite close to L_0. Figure 3.12 (b) shows a TEM image normal to the nanorod axis of the PS-b-PBD prepared in ~33-45 nm diameter pores. The structure of the cross-section consists of only two domains, PS at center and a PBD ring outside. At the inner interface of the PBD rings, two to four small PBD protrusions are seen, evenly distributed around the PS center. This indicates that, depending on D/L_0, multiple helices are formed. It is, however, clear that the morphology has changed from simple cylinders oriented along the axis of the nanorods to a morphology that is helical in nature.

The morphology of bulk sphere-forming copolymers confined within the cylindrical nanopores was also investigated. For cases with $D/L_0 > 3.2$, the PBD phase preferentially segregates to the pore wall, with spherical PBD domains aligned along the nanorod axis (Figure 3.13 (a)). However, a fluctuation is clearly seen along the interface between outmost PBD layer and the PS phase. In the bulk, the morphology consists of PBD spheres in a PS matrix. Within the nanopores, PBD adsorbs to the curved walls of the alumina pores, forcing the opposite curvature on the PS domain. When the pore diameter is decreased to $D/L_0 \sim 3.2$, the reduction in surface energy by wetting the pore walls with a PBD layer cannot balance the energy loss in deforming the spherical PBD domains and force an opposite curvature on the PS domain. Hence, unlike the lamellar and cylindrical copolymers under severe cylindrical confinement, the outmost PBD layer is no longer observed for the spherical microdomain case (Figure 3.13 (b)). Rather, two lines of PBD spheres are seen making a constant angle with respect to the nanorod axis, possibly indicating the formation of a helical string of PBD spheres.
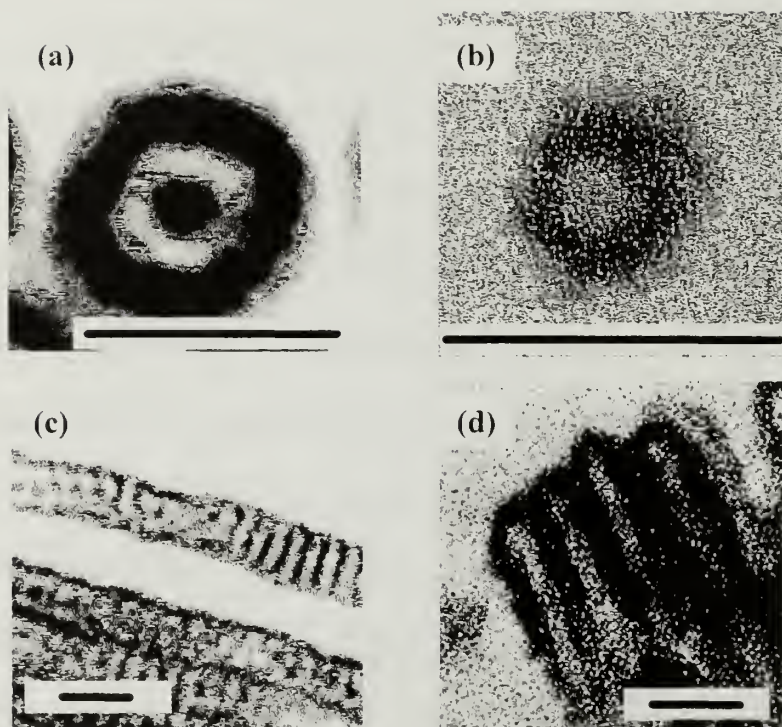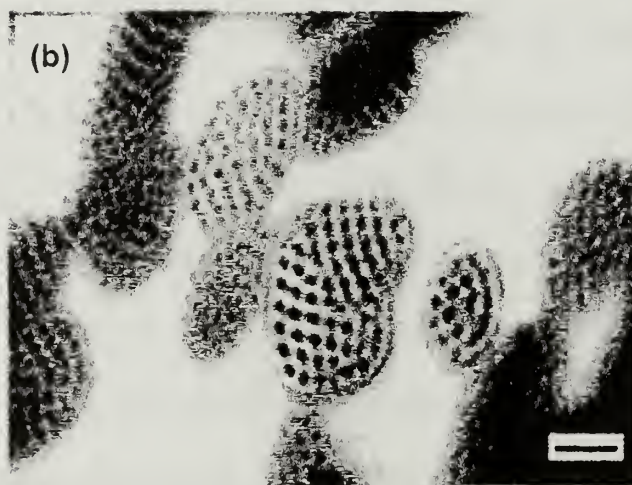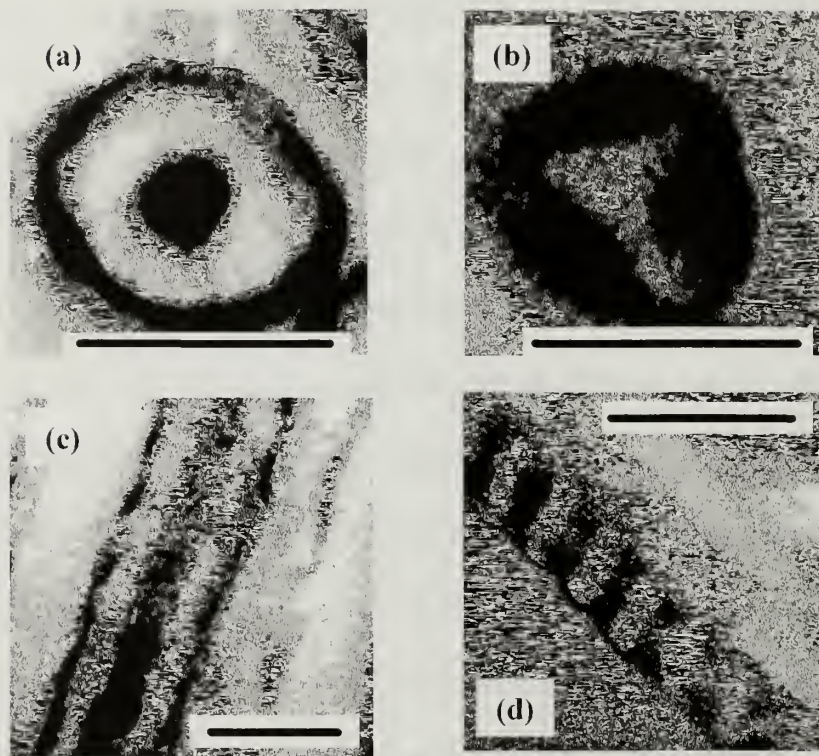
Figure 3.12. TEM cross-sectional images of bulk cylinder-forming PS-*b*-PBD nanorods. (a. b) Views normal to the nanorod axis: (c. d) Views along the nanorod axis: (a. c) D/L_0 = 1.9-2.3; and (b. d) D/L_0 = 1.1-1.5. Scale bars: 50 nm.[12]
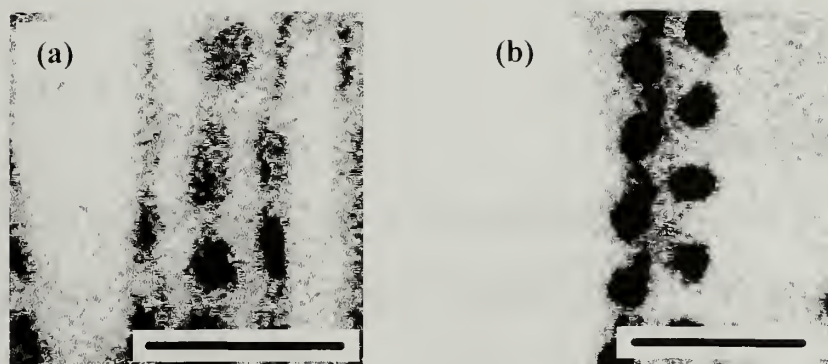
Figure 3.13. TEM cross-sectional images of bulk sphere-forming PS-*b*-PBD nanorods. Views along nanorod axis; (a) $D/L_0 > 3.2$; (b) $D/L_0 = 3.2$. Scale bars: 50 nm.[12]

3.4. Conclusions

Self-assembly under cylindrical geometric confinement was discussed for PS-*b*-PBB diblock copolymers that form lamellar, cylindrical, and spherical microdomain morphologies. Under this cylindrical confinement, the microphase-separation is well developed. At larger ratios of the pore diameter to the copolymer natural period D/L_0, the copolymers retain their alternating lamellar, hexagonal-packed cylindrical, and body-centered cubic spherical morphologies, respectively, and the microdomains align along the pore axis due to the preferential wetting of the pore wall with the PBD block. However, confinement effects are found to distort the natural packing of the microdomains and cause an apparent deviation of the repeat period from the bulk values. Under severe confinement, where the pore diameters are comparable to the equilibrium period of the copolymer, morphologies different than those observed in the bulk are seen. Stacked toruses, helical cylinders, and helical strings of spherical structures were seen for lamellar, cylindrical, and spherical copolymers, respectively. These morphologies, forced

59

on the block copolymer by curvature and incommensurability. are not accessible by other means.

3.5. References

(1)   Bates. F. S.: Fredrickson. G. H. *Phys Today* **1999**. *52*. 32-38.

(2)   Boltau. M.: Walheim. S.: Mlynek. J.: Krausch. G.: Steiner. U. *Nature* **1998**. *391*. 877-879.

(3)   Lambooy. P.: Russell. T. P.: Kellogg. G. J.: Mayes. A. M.: Gallagher. P. D.: Satija. S. K. *Phys. Rev. Lett.* **1994**. *72*. 2899-2902.

(4)   He. X. H.: Song. M.: Liang. H. J.: Pan. C. Y. *J. Chem. Phys.* **2001**. *114*. 10510-10513.

(5)   Sevink. G. J. A.: Zvelindovsky. A. V.: Fraaije. J. G. E. M.: Huinink. H. P. *J. Chem. Phys.* **2001**. *115*. 8226-8230.

(6)   Li. W. H.: Wickham. R. A.: Garbary. R. A. *Macromolecules* **2006**. *39*. 806-811.

(7)   Yu. B.: Sun. P. C.: Chen. T. C.: Jin. Q. H.: Ding. D. T.: Li. B. H.: Shi. A. C. *Phys. Rev. Lett.* **2006**. *96*. -.

(8)   Moon. S. I.: McCarthy. T. J. *Macromolecules* **2003**. *36*. 4253.

(9)   Xiang. H. Q.: Shin. K.; Kim. T.: Moon. S. I.; McCarthy, T. J.; Russell. T. P. *Macromolecules* **2004**. *37*. 5660.

(10)   Kim. E.: Xia. Y. N.: Whitesides. G. M. *Nature* **1995**. *376*. 581-584.

(11)   Suh. K. Y.; Kim, Y. S.: Lee. H. H. *Adv. Mater.* **2001**. *13*. 1386-1389.

(12)   Xiang. H.: Shin. K.: Kim. T.: Moon. S. I.: McCarthy. T. J.; Russell, T. P. *Macromolecules* **2005**. *38*. 1055-1056.

(13)   Shin. K.: Xiang. H. Q.: Moon. S. I.: Kim. T.; McCarthy. T. J.: Russell, T. P. *Science* **2004**, *306*, 76.

CHAPTER 4

POLYSTYRENE-POLYMETHYLMETHACRYLATE BLOCK COPOLYMER NANORODS

4.1. Introduction

The microphase-separated structures of block copolymers under cylindrical confinement have been discussed for the case of PS-*b*-PBD in Chapter 3. The commensurability of the block copolymer domains and the large curvature of pores play the roles in developing novel structures which have not been accessed by other means. In the case of PS-*b*-PBD, the interaction between the polymer blocks and the template surface is not a changeable factor. The surface energy of PBD at the processing temperature is lower than that of PS, and provides preferential affinity of PBD to the alumina surface (Table 4.1). The novel structures of PS-*b*-PBD are based on this condition.

Another important factor for the PS-*b*-PBD system is that this block copolymer is in the strong segregation regime, which means that χN of the system is much larger than 1. The interaction between the blocks should be one of the factors which determine the structure of block copolymers inside the nanopores along with commensurability, interface chemistry and large curvature.

PS-*b*-PMMA is an interesting material for its features relative to PS-*b*-PBD. First, PS-*b*-PMMA is in the weak segregation regime, therefore the microphase-separated structures inside cylindrical pores are expected to be different from those of PS-*b*-PBD at the same conditions. Second, the surface energy of PS and PMMA at the processing

temperature is quite similar (Table 4.1) and the affinity of one block to the alumina surface is determined by the pendant groups, not by surface energy differences. In this case, the carbonyl group makes PMMA relatively more polar than PS with a phenyl pendant group. Polar PMMA has an affinity to the polar alumina surface with aluminols; hydrogen bonding can be envisioned. Third, one component of PS-b-PMMA can be eliminated with ease. PMMA can be eliminated by being exposed to UV and treated with acetic acid. The empty space can be filled with other material, such metals with magnetic properties, and the composites can expand their potential applications based on the various structures of block copolymer microphase separation.

Table 4.1. Surface tension of polystyrene, polybutadiene, and polymethylmethacrylate (γ, mN/m = dyn/cm).[1]

	20 °C	150 °C	200 °C
PS			
M_v=44000	40.7	31.4	27.8
M_n=9300	39.4	31.0	27.7
M_n=1700	39.3	29.2	25.4
PBD			
M_n=5400	43.1	28.8	23.3
PMMA			
M=3000	41.1	31.2	27.4

The interaction between each block of the block copolymer and the surface of the template, which is alumina in this experiment, can be controlled in many ways. In the case of PS-b-PMMA, the factor which differentiates one block from the other is polarity.

Therefore, changing polarity is a way to control the phase of PS-*b*-PMMA inside the alumina pores.
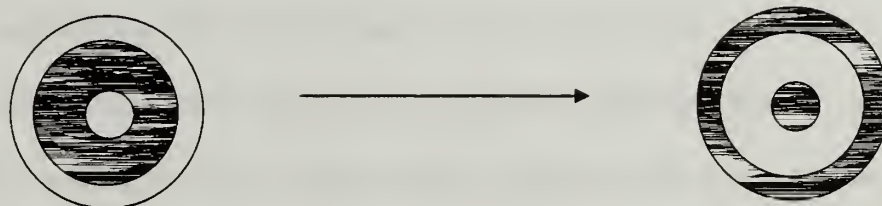
Figure 4.1. Schematic illustration of the expected phase-inversion of bulk-lamellar forming block copolymers inside cylindrical pores. In both cases, D/L_0 is 2.

Figure 4.1 shows a schematic illustration of phase inversion of bulk lamellar-forming block copolymer inside cylindrical pores. Bulk lamellar-forming diblock copolymer is expected to form multibarrel-layer structures as was described in Chapter 3. It is assumed that the affinity to the template surface is changed from one block (white one) to the other (grey one) by changing the surface properties of the alumina template. The morphologies in Figure 4.1 are basically the same structure, but have different outermost layer and middle phases. In both cases, D/L_0 is 2 and the commensurate condition is in force.

The alumina surface properties were changed by forming a self-assembled monolayer of octyltrimethoxysilane (OTMS) by silylation. OTMS has advantages over alkyltrichlorosilanes (Section 1.3) and the octyl group is not too bulky to prevent self-assembled monolayer formation in the convex curvature environment of pores, nor too short to change the polarity of the surface by covering with methyl groups. Figure 4.2 shows an illustration of self-assembled monolayer formation of OTMS on a flat alumina surface.

The purpose of this chapter is to investigate the structures of PS-*b*-PMMA inside cylindrical nanopores and the effect of the template surface properties on these block copolymer morphology. PS-*b*-PMMA nanorods were prepared using two kinds of membranes with different polarity: an untreated, polar alumina membrane and an OTMS-treated, non-polar alumina membrane. The research observed in this chapter was focused on the effects of surface properties of the template, as well as the block copolymer commensurability. The morphology of symmetric and asymmetric PS-*b*-PMMA confined in cylindrical nanopores of both untreated and OTMS-treated alumina membranes is addressed.
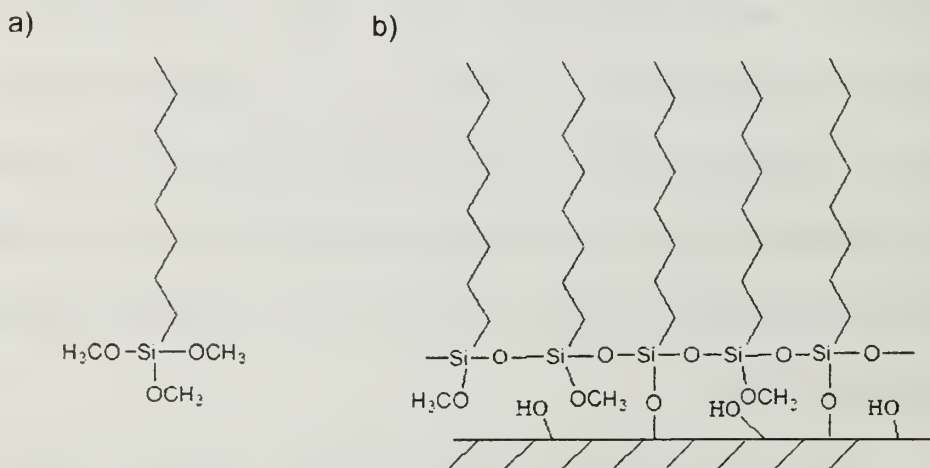
Figure 4.2. a) Octyltrimethoxysilane (OTMS). b) Self-assembled structure of OTMS on metal oxide surface.

4.2. Experimental

A symmetric PS-*b*-PMMA was purchased from Polymer Sources, Inc. with M_n of 51,000. The volume fraction of PS in the copolymer is 0.49 with a polydispersity of 1.09. The bulk morphology was lamellar with an equilibrium period of ~32.0 nm, as measured

by SAXS. Asymmetric PS-b-PMMA s with a PS volume fraction of ~0.7 were synthesized by anionic polymerization. having an M_n of 178.000. 76.200 and 56.800. The bulk morphology consists of PMMA cylinders in a PS matrix with a cylinder-to-cylinder distance of ~51.0 nm. ~35.0 nm. and ~32.0 nm. respectively (SAXS).

Alumina membranes with 200 nm pore diameters were purchased from Whatman. Inc.. as stated in chapter 3.2. In order to prepare alumina membranes with non-polar properties. alumina membranes were treated with octyltrimethoxysilane (OTMS). following a method for surface modification of silicon wafers.[2] Plasma-cleaned alumina membranes were held in a custom designed slotted holder and placed inside a flask with 0.5 ml of OTMS. The reaction was carried out at 70 °C for three days. The modified membranes were rinsed with toluene. hexane and ethanol and dried overnight under vacuum at 60 °C. OTMS was purchased from Aldrich and used as received.

The preparation of PS-b-PMMA nanorods using alumina membrane is similar to that of PS-b-PBD (Figure 3.3). The block copolymer was dissolved in toluene and cast on a slide glass. The film was dried at 170 °C under vacuum for 2 days to remove the solvent. The membrane was then placed on the dried block copolymer film and the assembly was heated to ~ 210 °C to allow the polymer melt to be drawn into the pores by capillary action. The polymer inside the membrane was annealed at 170 °C for 2.5 days under vacuum, and then the membrane was dissolved in an 80:20 mixture of 5% aqueous NaOH solution and methanol. respectively.

A JEOL 6320 FXV field emission scanning electron microscope (FESEM) was used to examine the nanorods. Free standing copolymer nanorods on a supporting film were immersed in an epoxy resin for microtoming. Thin sections were stained with

ruthenium tetroxide solution to selectively stain PS. A JEOL 100CX transmission electron microscope (TEM) was used to observe the morphology within the nanorods. The surface layers of the nanorods were analyzed by X-ray photoelectron spectroscopy (XPS). A Physical Electronics Quantum 2000 spectrometer with an Al Kα X-ray source was used at a spot size of 200 μm at 41.4 W. Spectra were acquired at 45° take-off angles.

4.3. Results

4.3.1. Modification of alumina membrane

Silylation of a flat alumina surface allows many ways to characterize the formation of the silane layer and the surface properties, including XPS, ellipsometry, contact angle, and AFM. There is no simple method to characterize the modified pore surface of alumina membranes due to their shape and accessibility. The only way was to break the untreated and treated membranes and analyze the broken surfaces by XPS. Figure 4.3 shows XPS spectra of the membrane pore surfaces. The Si_{2s} peak of the treated membrane demonstrates that the alumina surface is modified by silanes. It is noted that the cross sectioned surface is composed of both the treated pore surface and the untreated, newly exposed membrane surface. Therefore, the results are only qualitative, not quantitative interpretations. The modification of a flat aluminium surface using the same silane coupling agent and its analysis was also performed, and is described in Appendix.

4.3.2. Formation of PS-*b*-PMMA nanorods
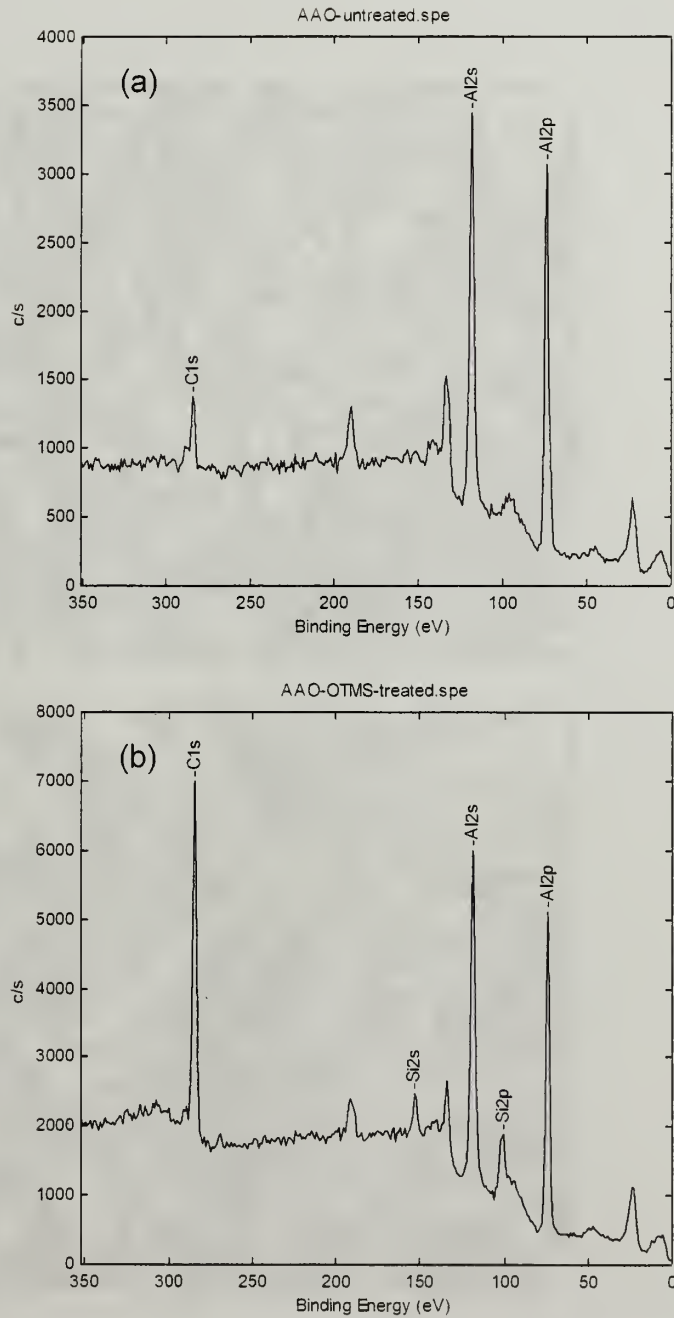
Figure 4.3. XPS spectra of the inside surface of the alumina membranes: (a) untreated alumina membrane, (b) OTMS treated membrane.
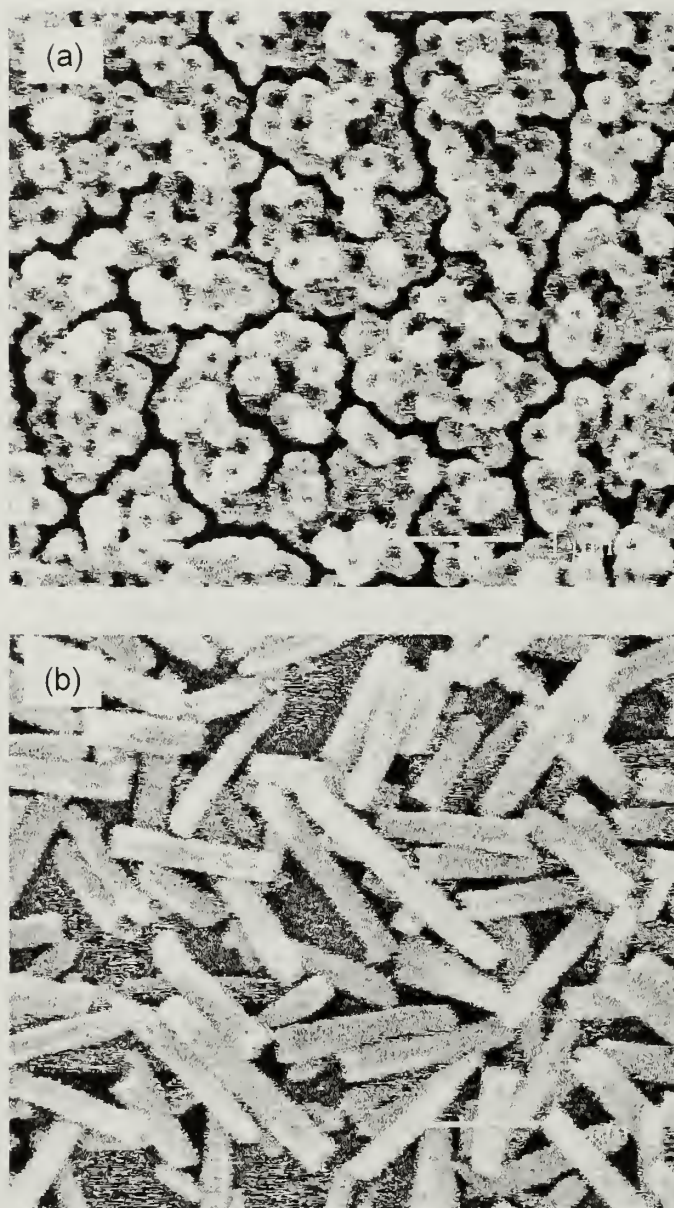
Figure 4.4. SEM micrographs of PS-*b*-PMMA nanorods: (a) before ultrasound treatment. (b) after ultrasound treatment.

Figure 4.4 shows SEM micrographs of the symmetric PS-*b*-PMMA nanorods after complete removal of the alumina membrane template (a), and separated nanorods from the substrate film (b). The nanorods show smooth surfaces and polydispersity in length, which is the result of ultrasound treatment. From Figure 4.4 (a), menisci are observed on the rods tops in the form of dark depressions, which indicate that the rods were formed due to a capillary force, like the case of PS-*b*-PBD (chapter 3.3.1). The nanorods, which were separated using ultrasound, show an aspect ratio ~ 8:1, and also show menisci at one end of some nanorods.

4.3.3. Symmetric PS-*b*-PMMA nanorods

Figure 4.5 shows TEM cross-sectional images of specimen microtomed normal to the nanorod axis and along the nanorod axis, for nanorods of symmetric PS-*b*-PMMA made using a commercial AAO membrane. Alternating dark (PS) and bright (PMMA) rings were observed from the view normal to the nanorod axis (Figure 4.5 (a)), with PMMA preferentially located at the interface with the pore wall. When these nanorods were cut normal to the nanorod axis, lines parallel to the nanorod axis were seen, as shown in Figure 4.5 (b). The outermost line in contact with the pore wall was PMMA, consistent with the other cross-section. These results indicate that the symmetric PS-*b*-PMMA copolymer forms a concentric multi-cylinder or multi-barrel morphology with PMMA preferentially segregated to the walls. The diameter of the confining pore is large in comparison to the period, as in the case of symmetric PS-*b*-PBD (Section 3.3.2).

The relationship between the number of cylinders and the ratio of the pore diameter to the equilibrium period of the copolymer in the bulk, D/L_0 was also
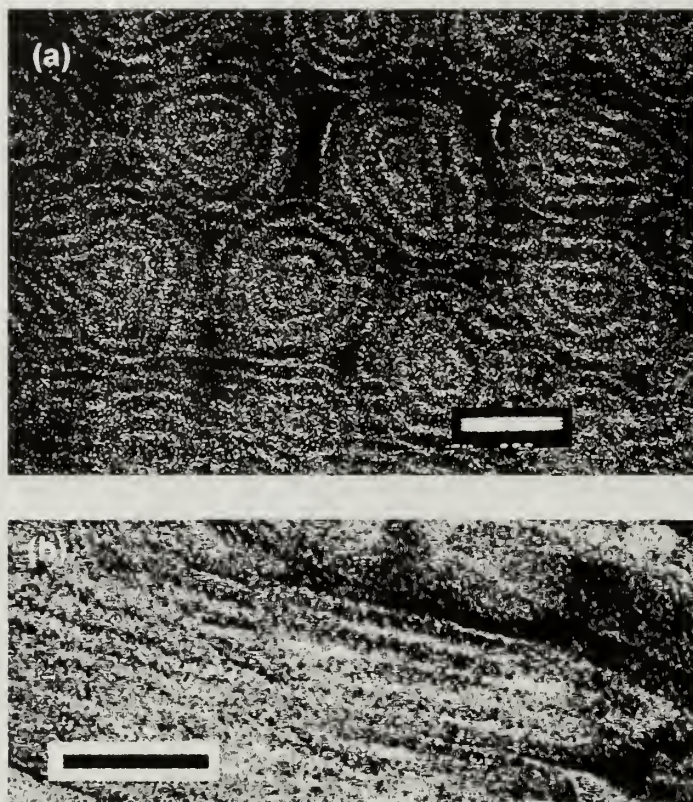
Figure 4.5. TEM cross-sectional images of symmetric PS-*b*-PMMA nanorods made using an untreated alumina membrane. (a) View normal to the nanorod axis. (b) View along the nanorod axis. Scale bars: 200 nm.
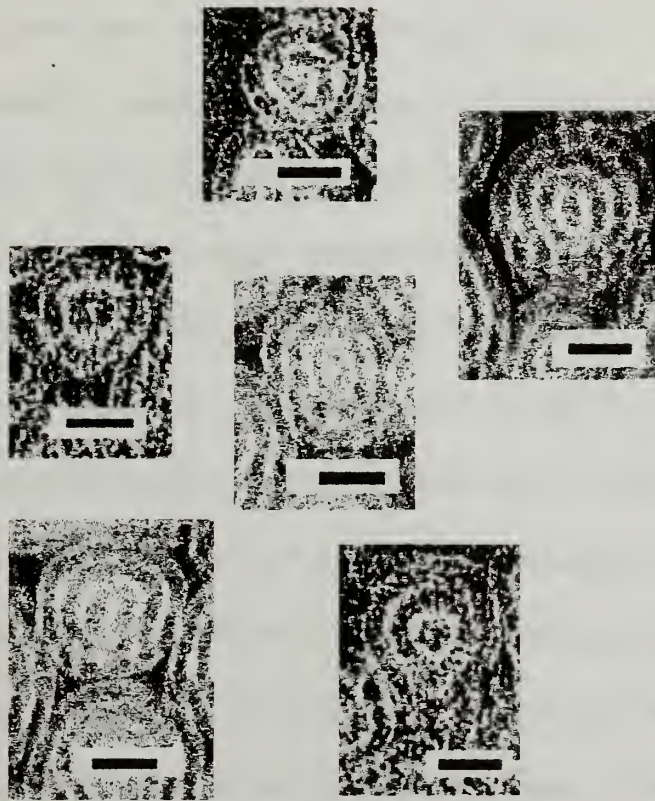
Figure 4.6. TEM images of symmetric PS-*b*-PMMA inside pores of various diameter. Scale bars: 100 nm.
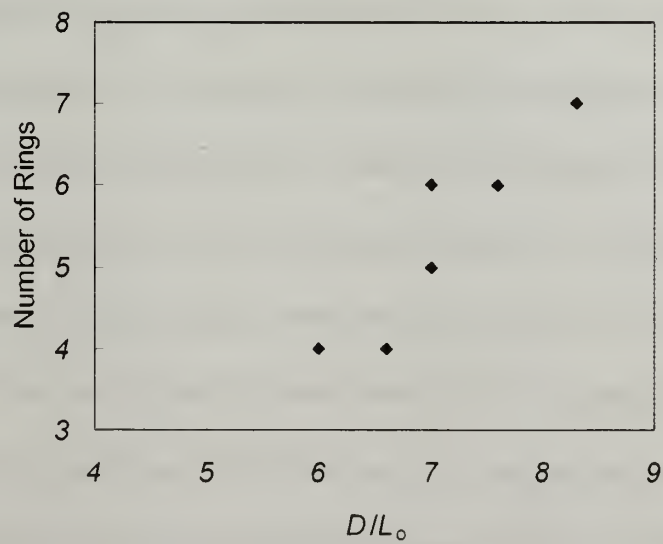
Figure 4.7. Number of cylinders vs. pore diameter normalized by the equilibrium repeat period.

investigated. The variation in pore diameter of the commercial membrane provides a morphology change as a function of the pore diameter. The outermost layer contacting the pore wall was always PMMA. However, the phase in the center could be either PS or PMMA, depending on the pore diameter, hence the number of PS or PMMA layers, as demonstrated in Figure 4.6. Figure 4.7 shows a plot of the number of cylinders as a function D/L_0. As the pore diameter decreases, the number of rings decreases uniformly, while the number of rings undergoes a series of discrete decreases from $n + 1$ to n cylinders. The apparent repeat period is measured by dividing the diameter of the nanorods by the number of periods. For the TEM images shown in Figure 4.6, the apparent periods vary from 38 nm to 50 nm within the pores, while a period of 32 nm is observed for bulk samples. As discussed in Chapter 3, these increases of periods indicate a perturbation of the fundamental period of the copolymer caused by confinement and curvature of the nanopores.

Figure 4.8 shows the TEM cross-sectional images for nanorods of symmetric PS-b-PMMA s made using OTMS treated commercial AAO membrane from two different perspectives. Compared with Figure 4.5, note that the dark PS layer is located outermost in both perspectives. Besides this phase inversion, other features are the same as those of PS-b-PMMA microphase structure formed inside untreated commercial AAO membrane.

This phase inversion is confirmed XPS analysis by verifying the outermost layer. For a comparison purpose, C_{1s} peaks of PMMA and PS are shown in Figure 4.9 (a) and (b), respectively.[3] The C_{1s} peak from PMMA shows a carbonyl group signal around 289 eV and the C_{1s} peak from PS shows the $\pi \rightarrow \pi^*$ shake-up satellite peak around 292 eV.
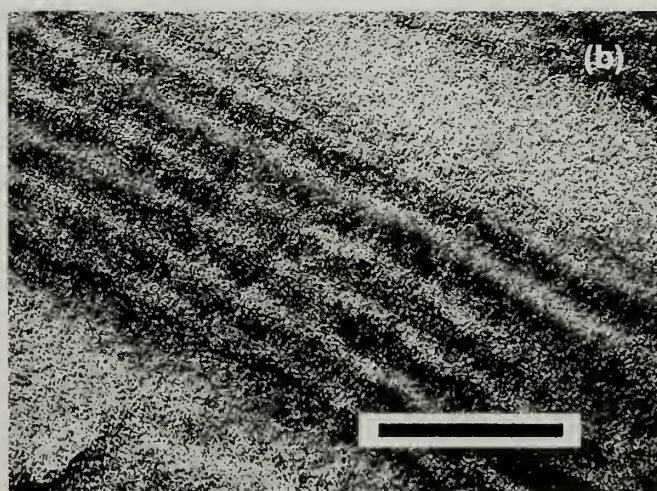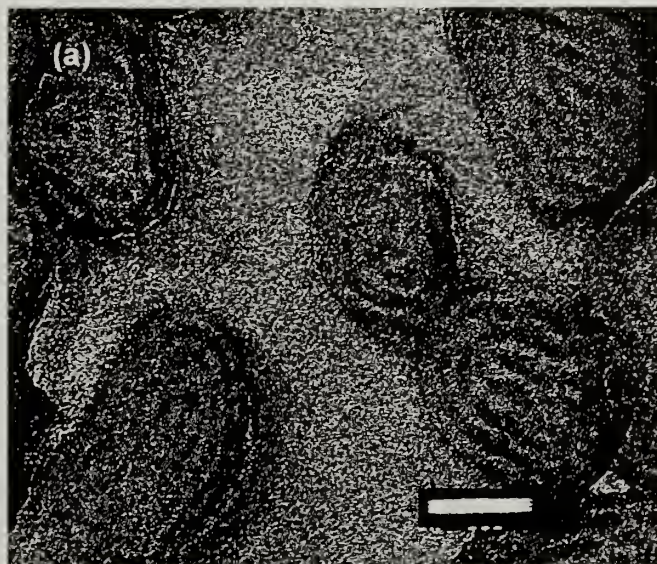
Figure 4.8. TEM cross-sectional images of symmetric PS-*b*-PMMA nanorods made using OTMS treated membrane. (a) View normal to the nanorod axis. (b) View along the nanorod axis. Scale bars: 200 nm.
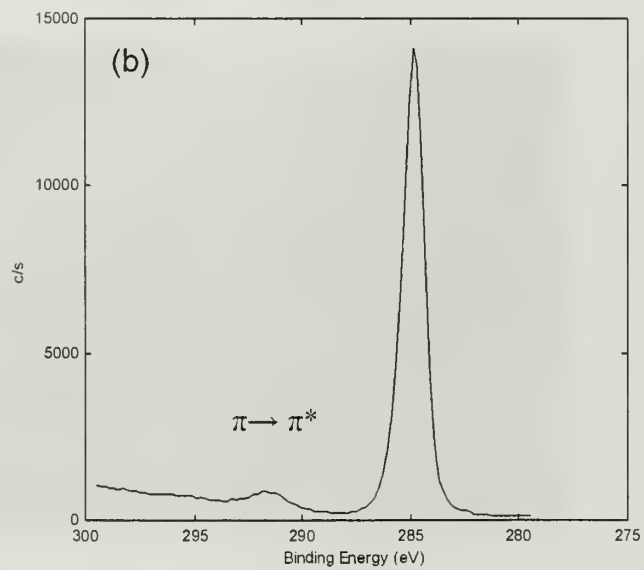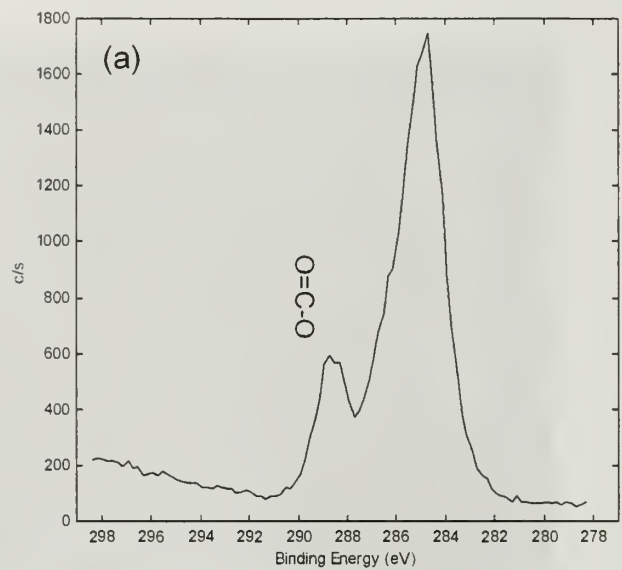
Figure 4.9. C_{1s} peaks of the surface of homogenous PS and PMMA: (a) PMMA (b) PS.
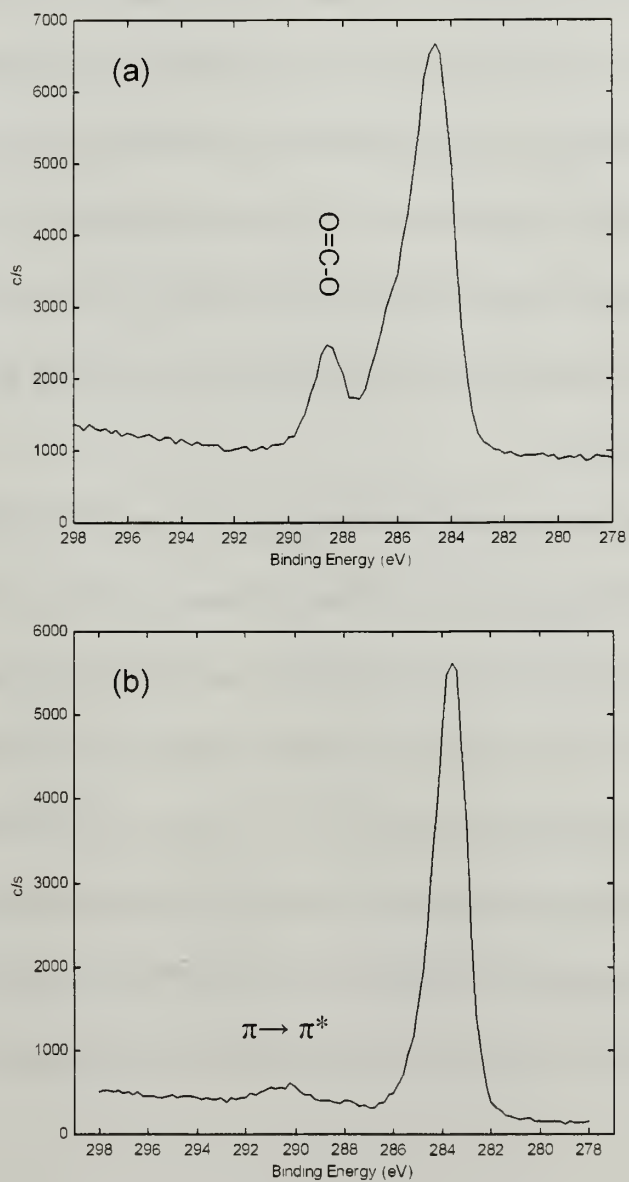
Figure 4.10. C_{1s} peaks of the surface of symmetric PS-*b*-PMMA nanorods. (a) From untreated membrane. (b) From OTMS treated membrane.

Figure 4.10 (a) and (b) shows C_{1s} peak of PS-*b*-PMMA nanorods made from untreated commercial AAO membrane, and from OTMS treated commercial AAO membrane, respectively. The comparison of C_{1s} peak of PS-*b*-PMMA in Figure 4.10 with the reference C_{1s} peak in Figure 4.9 indicates that the PS-*b*-PMMA nanorods made from untreated commercial AAO membrane have a PMMA outermost layer, and the PS-*b*-PMMA nanorods made from an OTMS-treated commercial AAO membrane have a PS outermost layer, consistent with the TEM results. This change in preferential segregation arises from the change in interfacial interaction by changing the polarity of alumina membrane surface.

Microphase-separated structures of symmetric PS-*b*-PMMA morphology were investigated when the D/L_0 is less than 4. Figure 4.11 shows TEM cross-sectional images for nanorods of symmetric PS-*b*-PMMA s made using home made AAO membranes. When D/L_0 is ~ 3.75, number of cylinder is three with PS located outermost. The number of cylinders becomes two when D/L_0 is 2.2 and 1.6, with PS located outermost. In all cases, multi-barrel structures were maintained, although some fluctuation was observed. No novel structures were observed as for PS-*b*-PBD. This phase inversion is believed to be due to the loss of selective surface affinity from the frustration caused by large curvature.

4.3.4. Asymmetric PS-b-PMMA nanorods

Figure 4.12 (a) and (b) show cross-sectional TEM images normal to the nanorod axis and along the nanorod axis, respectively, of asymmetric, bulk cylinder-forming PS-*b*-PMMA with M_n of 56,800 confined within an untreated commercial membrane. It can
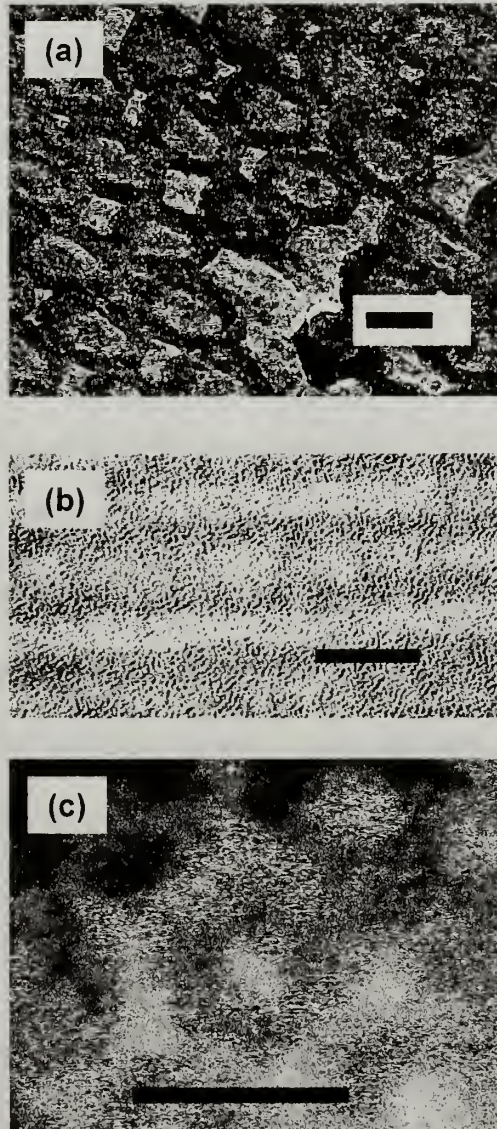
Figure 4.11. TEM cross-sectional images of symmetric PS-*b*-PMMA nanorods. (a) D/L_0 ~ 3.75. View across nanorod axis. Scale bar: 100nm; (b) D/L_0 ~ 2.2. View along the nanorod axis. Scale bar: 50 nm; (c) D/L_0 ~ 1.6. View normal to the nanorod axis. Scale bar: 50 nm.

be seen that the PMMA (bright) is preferentially segregated to the interface with the nanopore wall to form a rim. and the PMMA cylinders are hexagonally packed in a PS matrix (dark) along the nanorod axis inside the rim. Figure 4.12 (c) and (d) shows the cross-sectional TEM images normal to the nanorod axis and along the nanorod axis of asymmetric PS-*b*-PMMA confined within an OTMS-treated commercial membrane. It is observed that PS is preferentially segregated to the interface with the nanopore walls and that the PMMA cylinders are hexagonally packed in the PS matrix (dark) along the nanorod axis. This phase inversion is also confirmed by XPS. Figure 4.13 (a) and (b) show C_{1s} peaks of PS-*b*-PMMA nanorods made using untreated commercial membrane and OTMS-treated commercial membrane. respectively. The results indicate that the outermost layer of asymmetric PS-*b*-PMMA nanorods from untreated membrane is PMMA and the outermost layer from OTMS treated membrane is PS. consistent with the TEM results. This phase inversion is due to the change of polarity of alumina surface by modifying with OTMS. as in the case of symmetric PS-*b*-PMMA (Section 4.3.3).

In this case, D/L_0 is larger than 5. A smaller D/L_0 case was investigated by using a higher molecular weight asymmetric PS-*b*-PMMA. with M_n of 178,000 and L_0 of ~ 51 nm. In this case, D/L_0 is less than 5. Figure 4.14 (a) and (b) show the cross-sectional TEM images normal to the nanorod axis and along the nanorod axis. respectively. of asymmetric PS-*b*-PMMA with M_n of 178,000 confined within an untreated commercial membrane pores. and Figure 4.14 (c) and (d) show the cross-sectional TEM images normal to the nanorod axis and along the nanorod axis. respectively. of the same block copolymer confined within an OTMS-treated membrane. In comparison with Figure 4.5 and Figure 4.8. it should be noted that the PS is located at the membrane walls in both
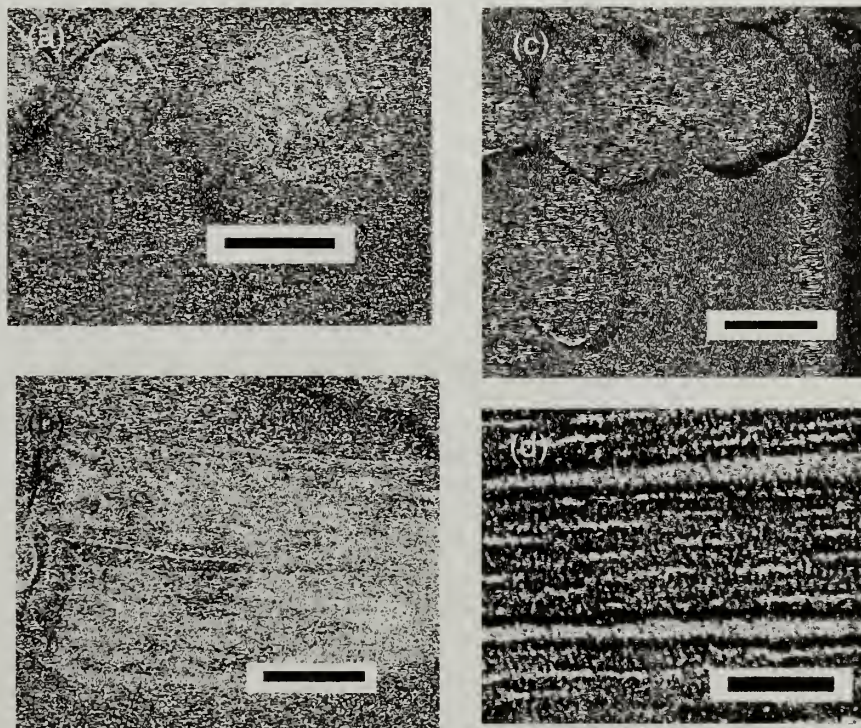
Figure 4.12. TEM cross-sectional images of bulk cylinder-forming PS-*b*-PMMA nanorods when $D/L_0 > 5$. (a, b) From untreated membrane. (c, d) From OTMS-treated membrane. (a, c) Views normal to the nanorod axis. (b, d) Views along the nanorod axis. Scale bars: 200 nm.
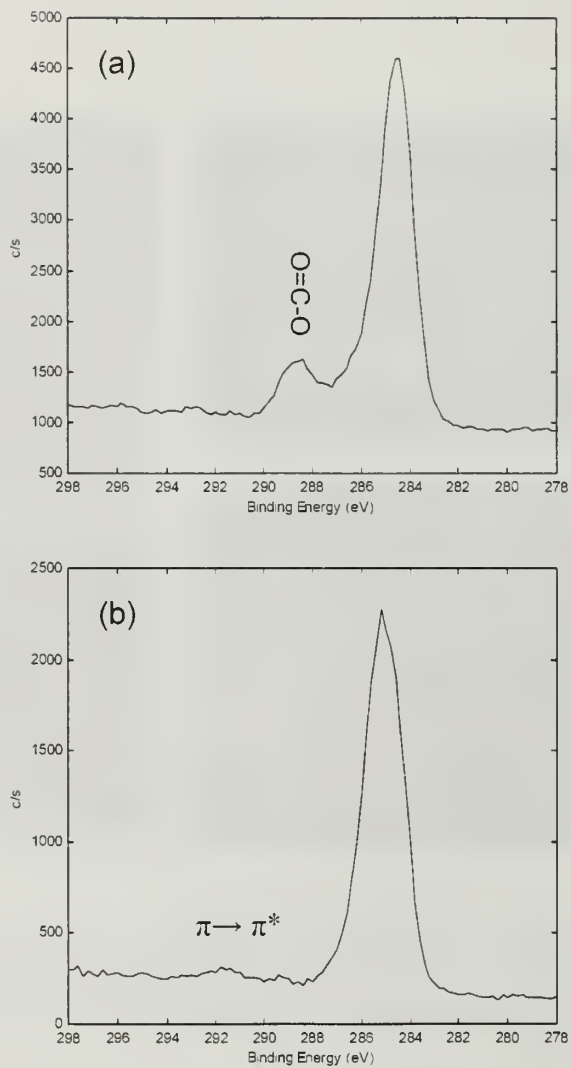
Figure 4.13. C_{1s} peaks of the surface of asymmetric PS-*b*-PMMA nanorods with M_n of 56.800. (a) From untreated commercial membrane. (b) From OTMS-treated commercial membrane.

cases. Aside from this, the morphology is unchanged. XPS experiments confirm this result. Figure 4.15 shows that the asymmetric PS-*b*-PMMA nanorods with M_n of 178.000 have PS outermost layers when made using both untreated and OTMS-treated commercial membrane.

In the case of OTMS-treated membrane. both a larger volume fraction of PS and the affinity of PS to the modified alumina surface have a synergistic effect to form a structure with a PS outermost layer. In the case of the untreated membrane. volume fraction. which is an entropic term and surface affinity. which is an enthalpic term. have conflicting effects on the formation of the outermost later. A larger volume of PS leads to a PS outermost layer. and the affinity of polar PMMA to the untreated alumina membrane surface leads to a PMMA outermost layer. The result indicates that the surface affinity of PMMA to the alumina template sufficient to overcome the entropic preference for PS to form a contacting layer to alumina surface.

The same phenomenon is observed when the pore size is smaller than 100 nm so that D/L_0 is less than 5. Figure 4.16 (a) and (b) show the cross-sectional TEM images normal to the nanorod axis and along the nanorod axis. respectively. of asymmetric PS-*b*-PMMA with M_n of 76,200 confined within an untreated home made membrane with 70 nm pore size. The D/L_0 becomes ~ 2. It is observed that one string of PMMA is buried in PS matrix, contacting PS to the pore wall. This structure has a possibility of potential application for nanotubes or patterns for storage device. The XPS result confirms that PS layer is located outermost (Figure 4.17).

4.4. Conclusions
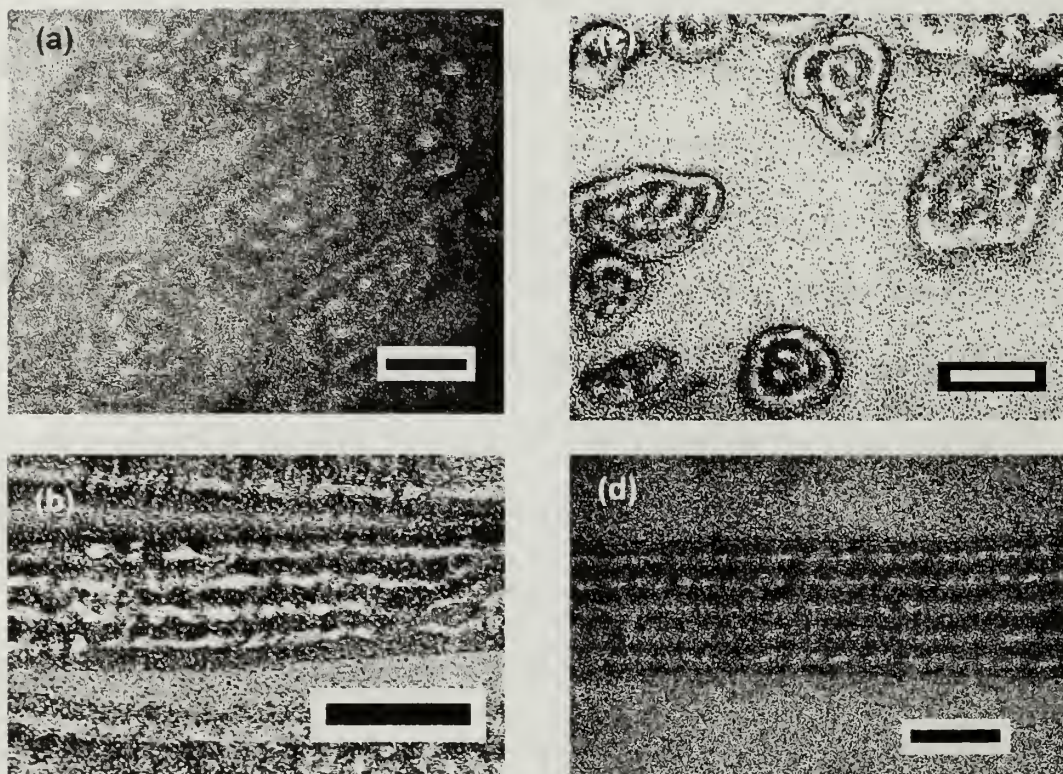
Figure 4.14. TEM cross-sectional images of bulk cylinder-forming PS-*b*-PMMA nanorods when $D/L_0 < 5$. (a, b) From untreated membrane. (c, d) From OTMS treated membrane. (a, c) Views across the nanorod axis. (b, d) Views along the nanorod axis. Scale bars: 200 nm.
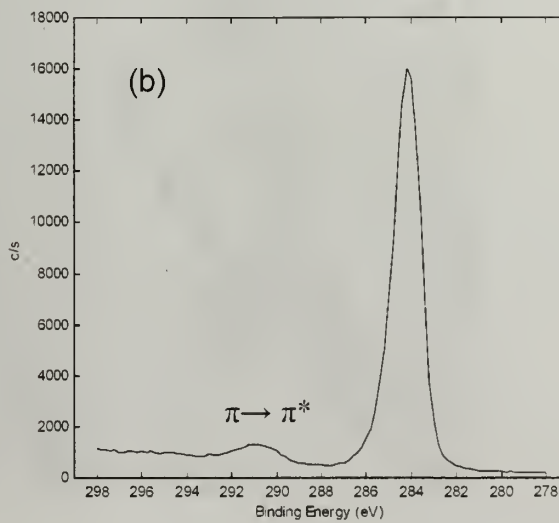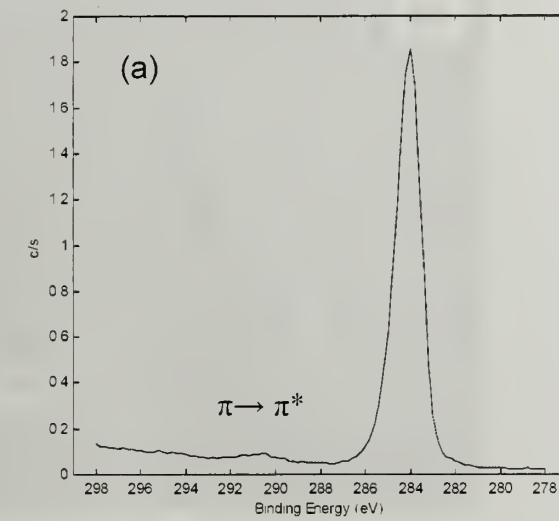
Figure 4.15. C_{1s} peaks of the surface of asymmetric PS-*b*-PMMA nanorods with M_n of 178,000. (a) From untreated commercial membrane. (b) From OTMS treated commercial membrane.
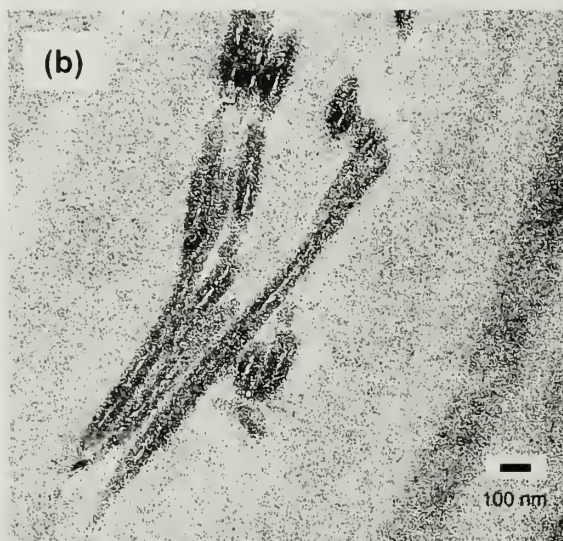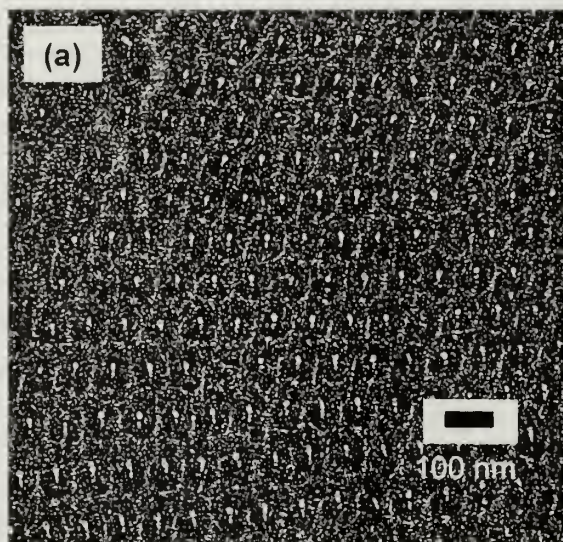
Figure 4.16. TEM cross-sectional images of bulk cylinder-forming PS-*b*-PMMA nanorods when D/L_0 is ~ 2.0. (a) View cross the nanorod axis. (b) View along the nanorod axis.
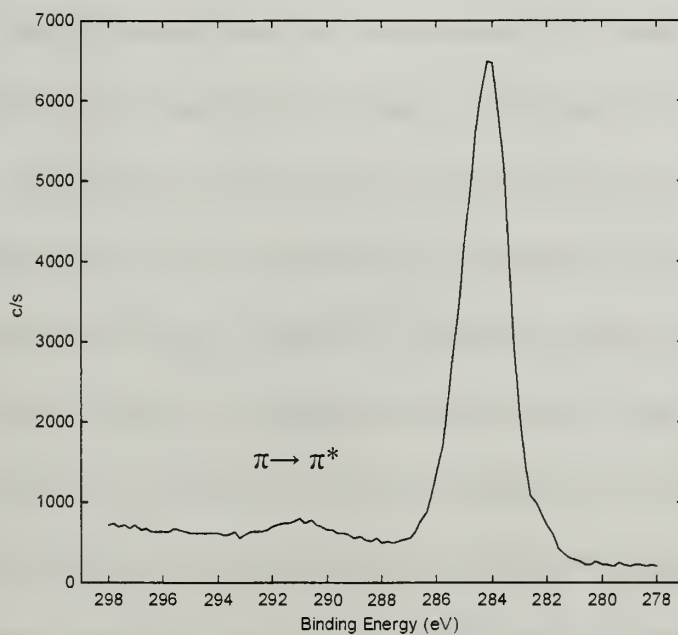
Figure 4.17. C_{1s} peak of the surface of asymmetric PS-*b*-PMMA nanorods from untreated home made membrane, with $D/L_0 \sim 2.0$.

Self-assembly under cylindrical geometric confinement was discussed for PS-*b*-PMMA diblock copolymers that form lamellar and cylindrical morphologies. At larger ratios of the pore diameter to the copolymer natural period D/L_0, the copolymers retain their alternating lamellar and hexagonal-packed cylindrical morphologies, respectively, with a PMMA layer contacting the pore wall. These phases can be inverted by alumina surface modification with OTMS. This is due to the change of the polarity of template surface by forming nonpolar monolayer on polar alunina surface.

However, at smaller D/L_0 condition, the surface affinity of PMMA to the polar alumina surface is not as strong as the larger D/L_0 condition. The lamellar forming PS-*b*-PMMA exhibits PS outermost layers when D/L_0 is less than 5 inside untreated alumina pores, and the cylinder-forming PS-*b*-PMMA nanorods have a PS outermost layer when D/L_0 is less than 5 inside untreated alumina pores, which is counter to what would be observed if the polar interaction between PMMA and the alumina surface dominated. The case of asymmetric PS-*b*-PMMA is explained that the enthalpic term due to the affinity by polar interaction is not sufficient to overcome the system s entropy, which is controlled by the volume fraction of the block copolymer.

4.5. References

(1)   Brandrup, J.; Immergut, E. H.; Grulke, E. A. *Polymer Handbook*, 4th ed.; John Wiley & Sons, Inc., 1999.

(2)   Fadeev, A. Y.; McCarthy, T. J. *Langmuir* **2000**, *16*, 7268-7274.

(3)   Ton-That, C.; Shard, A. G.; Teare, D. O. H.; Bradley, R. H. *Polymer* **2001**, *42*, 1121-1129.

CHAPTER 5

PREPARATION OF COMPOSITE NANORODS USING CARBON DIOXIDE

5.1. Introduction

In Chapters 3 and 4, two kinds of block copolymer nanorods were prepared using AAO membranes and their microphase separated structures inside cylindrical pores were investigated. These diblock copolymers developed various novel structures inside cylindrical pores and suggested possibilities of potential applications. In this case, the AAO membrane plays a role as a template to form a structured block copolymer. As stated in Section 1.1, nanorods composed of two-components, or multi-components, have wider possibilities for both theoretical research and application than homogeneous nanorods.[1]

Nanorods or nanotubes can be prepared using AAO membrane from many materials besides block copolymers, including dendrimers[2] and polyelectrolytes.[3,4] Semicrystalline polymers are another interesting nano-template material which can form nanorods. Semicrystalline polymers are composed of two phases: a crystalline phase of thin (order 10 nm) lamellar-shaped crystals and an amorphous phase consisting of inter-lamellar tie chains, connecting adjacent crystal lamellae.

Crystallization can be considered as a molecular self-assembly process. The growth of crystals and their final structures are affected by chain folding, lamellar thickening, fractionation, or chain diffusion.[5] When a polymer is confined with solid surface, the ordering can be modified or frustrated. Most studies have focused on thin

films on the solid substrates.[5-9] Semicrystalline polymers confined inside cylindrical nanopores provide unique opportunity to research the effect of substrates on the crystallization kinetics and morphology.

Another interesting possibility of a multi-component nanorod is that this material can be a template for preparing new composite materials while preserving original nano-structures by selective deposition of another material to one of the components. Preparing composite materials has been a traditional method for developing materials with new properties, avoiding much effort to synthesize a new molecule. The preparation of nano-composite materials from polymers can be accomplished by traditional methods. A target material, such as carbon nanotubes[10-12] or inorganic particles,[13-15] could be mixed with polymer or chemically attached to the polymer backbones.

As stated in chapter 1.4, using liquid or supercritical carbon dioxide as a medium is a unique method to prepare composite materials starting from solid polymers. The polymer/polymer composite material is prepared by polymerizing a different monomer inside a solid polymer substrate. The properties of the substrate are thus modified because the final product is actually a mixture of two polymers. Polymer/metal composites can be prepared by introducing a metal precursor and reducing it to form metal clusters. The final product can have additional properties because of the metal addition to the substrate.

An interesting feature of semicrystalline polymers as nano-templates is that CO_2 normally swells only in the amorphous region of the semicrystalline polymer, and therefore subsequent reaction and modification occurs only in the amorphous regions. This results in nano-composite materials original structure preserved, for instance lamella of crystalline stacks in the amorphous/polymer mixture matrix.[16]

The purpose of the research described in this chapter was to prepare two types of composite nanorods from semicrystalline polymer using CO_2 as reaction medium: polymer/polymer nanorods by polymerization of monomer and polymer/metal nanorods by metal deposition inside semicrystalline polymer nanorods. Poly(4-methyl-1-pentene) (PMP) nanorods are used as the substrate. For the preparation of polymer/polymer nanorods. norbornene is polymerized in the amorphous regions of PMP nanorods by ring-opening metathesis polymerization (ROMP). The reaction scheme is shown in Figure 5.1. ROMP of norbornene in liquid and supercritical CO_2 using Grubbs catalyst and Schrock s catalyst was studied by Fürstner et al..[17,18] and the preparation of PMP/polynorbornene was studied by Cao et al.[16]
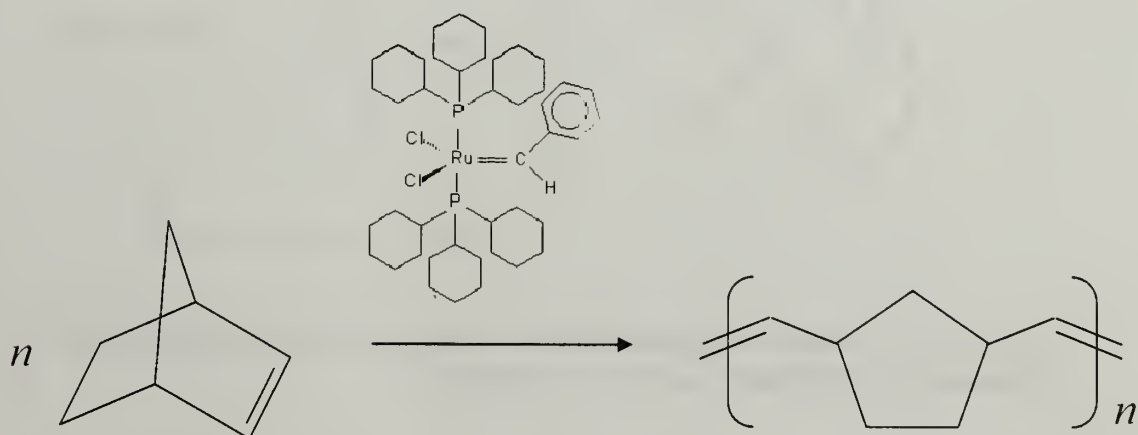
Figure 5.1. Reaction scheme of polymerization of norbornene using Grubbs catalyst.

The polymerization of norbornene inside PMP was chosen for a particular reason. The density of the crystalline and amorphous regions of PMP is too similar to show sufficient contrast in TEM observation. The selective staining of the polynorbornene

89

embedded in the amorphous region of PMP by OsO_4 enables the observation of crystalline/amorphous phases of the original PMP.

For the preparation of polymer/metal nanorods. a typical organometallic precursor for Pt deposition. dimethyl(cyclooctadiene)platinum(II) (CODPtMe$_2$). was used. It has several attractive features as a precursor for Pt deposition in supercritical carbon dioxide (Sc CO$_2$). It is known that this precursor is reduced by hydrogen to give high purity Pt. This reduction is autocatalytic as described in Figure 5.2. producing high Pt content of 58.5%. Its low toxicity and heptane solubility indicate its good solubility in CO_2 and hydrocarbon polymers such as PMP.[19]
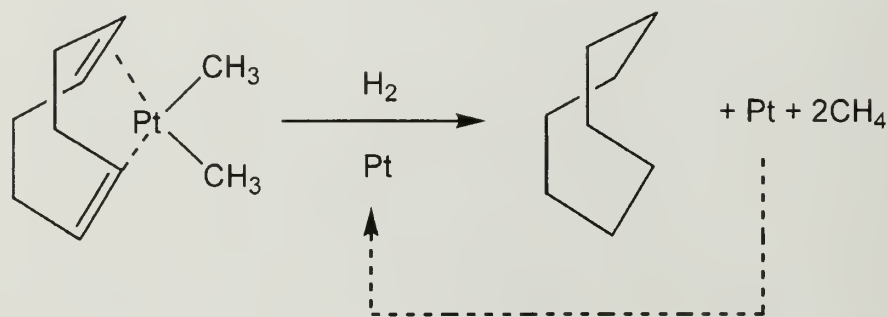
Figure 5.2. Reduction of organometallic Pt precursor. dimethyl(cyclooctadiene) platimun(II) (CODPtMe$_2$). to Pt cluster using H$_2$.[20]

5.2. Experimental

5.2.1. Materials

Poly(4-methyl-1-pentene) (PMP) of 26 g/10 min melt index was obtained from Scientific Polymer Products. Inc. The procedure for the preparation of thin films from the PMP pellets followed previous research.[16] The PMP pellets were melt-pressed into

0.1mm thick films at 260 °C and 25.000 psi. cooled down to 100 °C by air and then by cool water below 100 °C. The final film was transparent and not very flexible. These films were cut into proper sized specimen, usually 20 mm x 20 mm, larger than a commercial alumina membrane (13 mm diameter). Commercial alumina membranes of 200nm pore size were purchased from Whatman. Inc.

Norbornene and Bis(tricyclohexylphosphine)benzylidineruthenium(IV) dichloride (Grubbs catalyst) were obtained from Aldrich and used as received. Methylene chloride was purified following a reported procedure[21] and stored under nitrogen in a dark area. Ethyl vinyl ether and ethanol were obtained from Aldrich and used as received. Dimethyl(cyclooctadiene)platinum(II) ($CODPtMe_2$) was obtained from Aldrich and used as received. Aqua regia was prepared by mixing 1:4 concentrated nitric acid and concentrated hydrochloric acid, respectively. Carbon dioxide (Coleman grade 99.99 %, Merriam Graves) was passed through activated alumina and Q-5 catalyst (Englehard Industries) to remove water and oxygen, respectively. A 100DM high-pressure syringe pump (Isco Inc.) fitted with a heating/cooling jacket was used to deliver CO_2 at the required pressure and temperature.

5.2.2. Preparation of PMP nanorods

A commercial alumina membrane was placed on a PMP film and the assembly was placed in the gap of glass vacuum chamber. which is designed to place the assembly on the hot plate under vacuum to avoid thermal degradation. (Figure 5.3) The whole set was heated at 265 °C to induce capillary action of the PMP melt for 20 minutes under vacuum. It is noted that the range of the processing temperature for a semicrystalline

91

polymer is much narrower that that for an amorphous polymer, because the viscosity of semicrystalline polymer drops dramatically around its melting temperature.
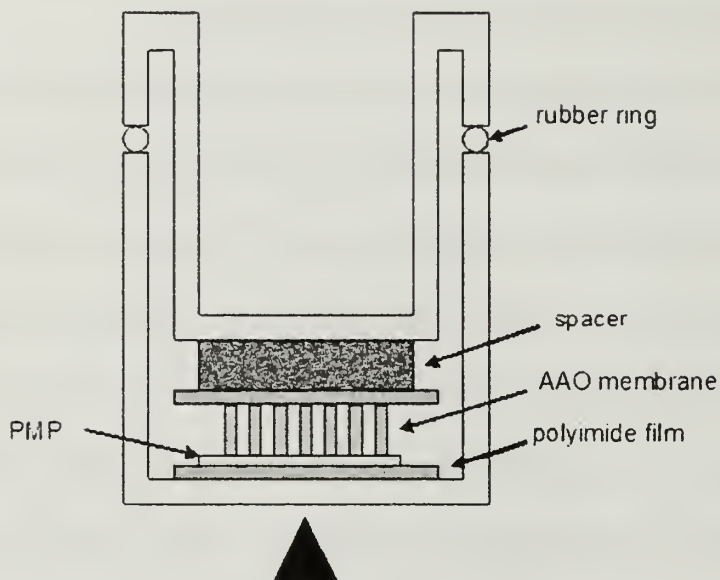
Figure 5.3. Experimental setup for the preparation of semicrystalline polymer nanorods using AAO membrane under vacuum.

5.2.3. Preparation of PMP/polynorbornene nanorods using liquid CO_2

After the alumina membrane was dissolved in a basic solution (Section 2.2), the free-standing polymer nanorods attached to film were soaked in a 4 mg/ml solution of Grubbs catalyst in CH_2Cl_2 for two hours. After soaking, the sample was rinsed with CH_2Cl_2 to remove any surface-adsorbed catalyst, and dried under vacuum to remove the solvent inside the sample. The sample was then sealed in a stainless-steel reaction vessel with norbornene, and CO_2 was introduced into the vessel at 2000 psi and 23°C. After 8 hours of reaction, CO_2 was vented into ethanol, and the sample was extracted with CO_2

92

several times to remove all unreacted norbornene. Ethyl vinyl ether was added at the same time to deactivate the remaining catalyst.

A JEOL 6320 FXV field emission scanning electron microscopy (FESEM) was used to examine the nanorods. Free standing PMP/polynorbornene nanorods on a supporting film were immersed in an epoxy resin for microtoming. Thin sections were stained with osmium tetroxide vapor to selectively stain polynorbornene. A JEOL 100CX or 2000FX transmission electron microscope (TEM) was used to observe the morphology within the nanorods.

5.2.4. Preparation of PMP/Pt nanorods using Sc CO_2

The PMP nanorods with substrate film were obtained after dissolving alumina membrane as chapter 5.2.2. The sample was sealed in a reaction vessel with a certain amount of $CODPtMe_2$ powder and CO_2 was introduced at 2000 psi at 40 °C. After 8 hours H_2 was introduced into the reaction vessel at 3500 psi at the same temperature. After 4 hours of reaction, CO_2 was vented into ethanol, and the sample was rinsed with aqua regia to remove Pt clusters on the surface.

A JEOL 6320 FXV field emission scanning electron microscopy (FESEM) was used to examine the nanorods. Free standing PMP/Pt nanorods on a supporting film were immersed in an epoxy resin for microtoming. A JEOL 100CX or 2000FX transmission electron microscope (TEM) was used to observe the morphology within the nanorods.

5.3. Results

5.3.1. PMP/polynorbornene nanorods
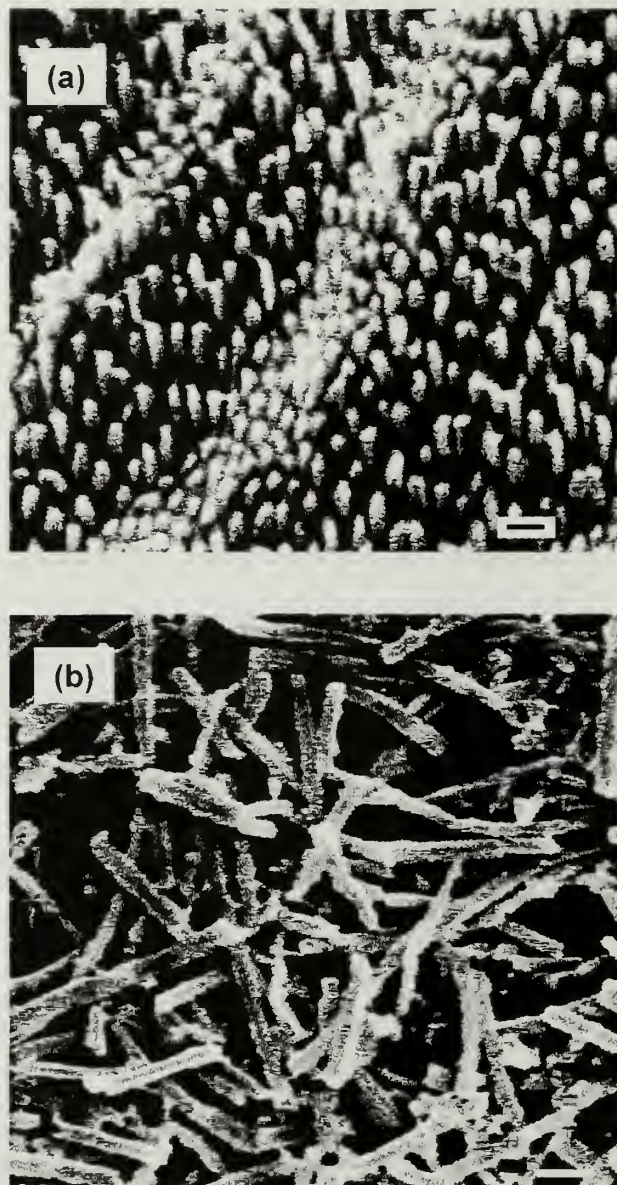
Figure 5.4. SEM micrographs of PMP nanorods. (a) Before ultrasound treatment. (b) After ultrasound treatment. Scale bars: 2 μm (a): 1 μm (b).

Figure 5.4 shows SEM micrographs of the PMP nanorods after complete removal of the alumina membrane template (a), and separated nanorods from the substrate film (b). These semicrystalline polymer nanorods stand straight from the film, contrary to the amorphous polymer nanorods. The nanorods show smooth surfaces and polydispersity in length. This polydispersity can be either the result of ultrasound treatment or narrow processing temperature range.

Figure 5.5 shows the TEM cross-sectional images for a bulk PMP/polynorbornene composite. It is noted that norbornene can enters into amorphous and inter-lamellar regions. The polymerization of norbornene monomer is initiated by the pre-embedded catalyst. OsO_4 stains the polynorbornene in these regions black. The white lines in the TEM images have uniform thickness, indicating a lamellar structure. It is also noted that this lamellar structure is formed in a nano-composite material, which is basically blend because there is no chemical grafting between PMP and polynorbornene. This polymer/polymer composite achieves its nano-structure not by a thermodynamic process or by chemical linking, but by using one polymer as a template.[16]

Figure 5.6 shows TEM cross-sectional images of a specimen microtomed normal to the nanorod axis and along the nanorod axis, for PMP/polynorbornene nanorods made using a commercial AAO membrane. Dispersed dark spots were observed in the bright matrix from the view normal to the nanorod axis (Figure 5.6 (a)) and aligned dark spots were observed inside the nanorods from the view along the nanorod axis (Figure 5.6. (b)). These results indicate that spherical amorphous regions are formed inside crystalline regions, forming lines along the nanorods. There can be two different expectations of

95
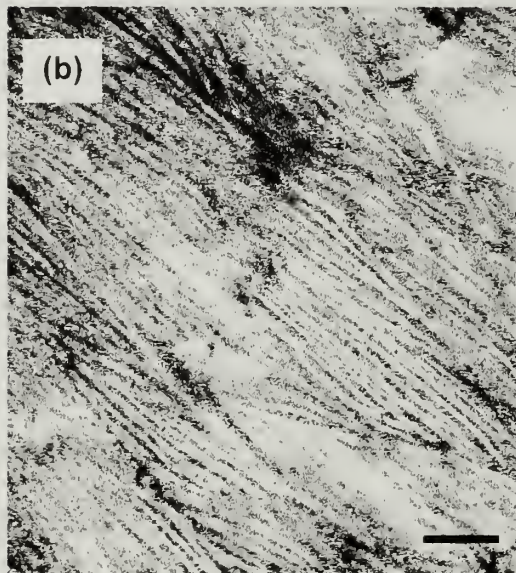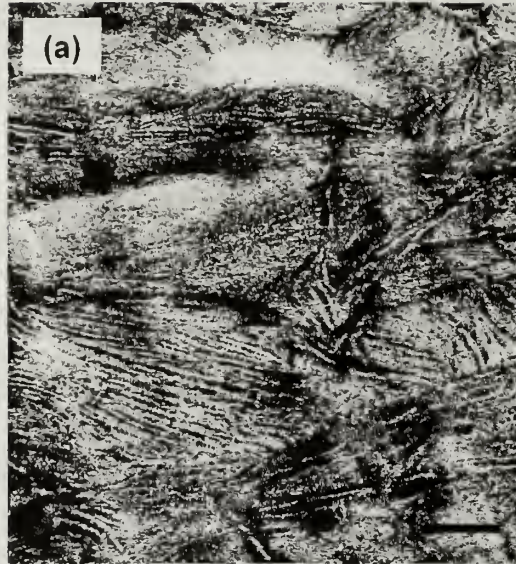
Figure 5.5. TEM micrographs of PMP/Polynorbornene nanocomposite. Polynorbornene stained by OsO_4 helps observation of lamellar stack. Scale bars: 400 nm (a): 200 nm (b).

Figure 5.6. TEM micrographs of PMP/Polynorbornene nanorods. (a) View normal to the nanorod axis. (b) View along the nanorod axis. Scale bars: 200 nm.

bulk lamellar-forming crystalline phases inside cylindrical pores. First, a multi-barrel type structure is expected as in the case of symmetric block copolymer (Section 3.3.2 and Section 4.3.2), which is the result of geometric confinement of lamellar structure. Second, a spoke-like radial structure of crystal lamellar is expected, because the crystallization starts from the surface, which is called trans-crystallization or epitaxial crystallization.[22,23] The result is interpreted as either a combination of these two effects or frustrated trans-crystallization due to the curvature of the cylindrical pores.

5.3.2. PMP/Pt nanorods

Figure 5.7 shows SEM micrographs of the PMP/Pt nanorods after complete removal of the alumina membrane and rinsing with aqua regia solution to remove any Pt clusters on the surface. The PMP/Pt nanorods show smooth surfaces and no remaining Pt clusters are observed.

Figure 5.8 shows TEM cross-sectional images for bulk PMP/Pt composites, prepared with different $CODPtMe_2$ concentrations in CO_2. The sample shown in Figure 5.8 (a) was prepared with 11.85 mg/ml $CODPtMe_2$ in Sc CO_2 (sample A) and the sample shown in Figure 5.8 (b) was prepared with 63.3 mg/ml $CODPtMe_2$ in Sc CO_2 (sample B). Pt clusters are shown as black dots in the TEM micrographs and dispersed throughout the samples. The size of Pt clusters formed at higher concentration of $CODPtMe_2$ is larger than that formed at lower concentration of $CODPtMe_2$. The Pt clusters formed inside sample A have ~ 10 nm diameters and the Pt clusters formed inside sample B diameters greater than 200 nm. The Pt clusters in sample A can be formed in amorphous and inter-

lamellar regions, while the Pt clusters in the sample B can only be formed in the amorphous region due to the their size.
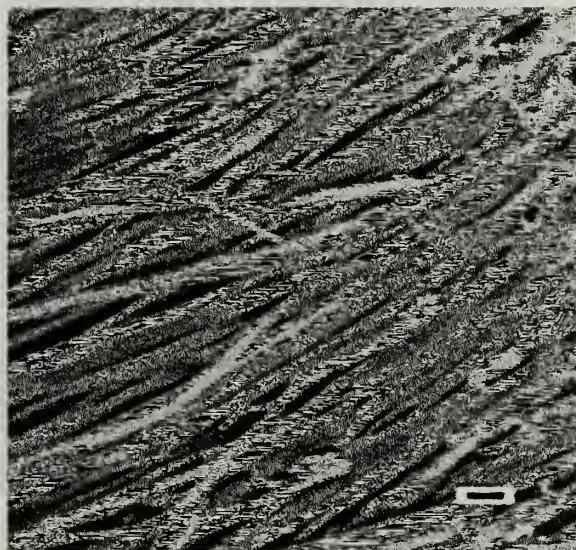
Figure 5.7. SEM micrograph of PMP/Pt nanorods after rinsing with aqua regia. Scale bar: 1 μm.

The presence of Pt clusters is also confirmed by Selected Area Electron Diffraction (SAED) in conjunction with TEM. Figure 5.9 shows the result of SAED for sample B. showing concentric rings corresponding to the d spacings [110], [200], and [220] of fcc platinum (International Center for Diffraction Data, #04-0802). The ring corresponding to the d spacing of [311] is vague in this experiment.[24]

Figure 5.10 shows TEM cross-sectional images of a specimen microtomed normal to the nanorod axis and along the nanorod axis. for PMP/Pt nanorods made using a commercial AAO membrane. The sample was prepared with 11.85 mg/ml CODPtMe$_2$ in Sc CO$_2$. Aligned dark spots were observed inside the nanorods from the view along the nanorod axis (Figure 5.10. (a)) and dispersed dark spots were observed inside the
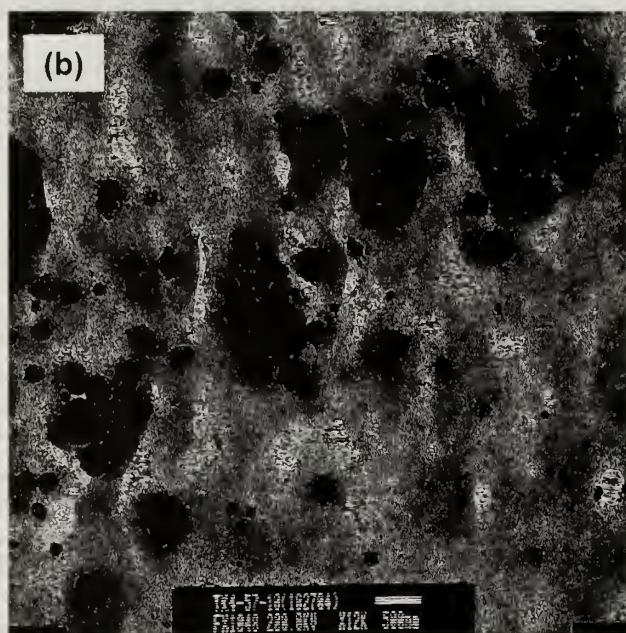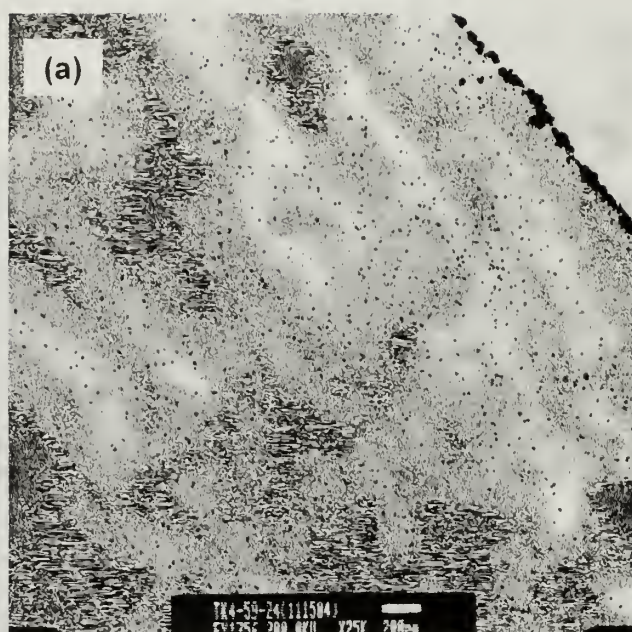
Figure 5.8. TEM micrographs of PMP/Pt nanocomposite with different organometallic precursor concentration. (a) 11.85 mg/ml. (b) 63.3 mg/ml. Scale bars: (a) 200 nm. (b) 500 nm.
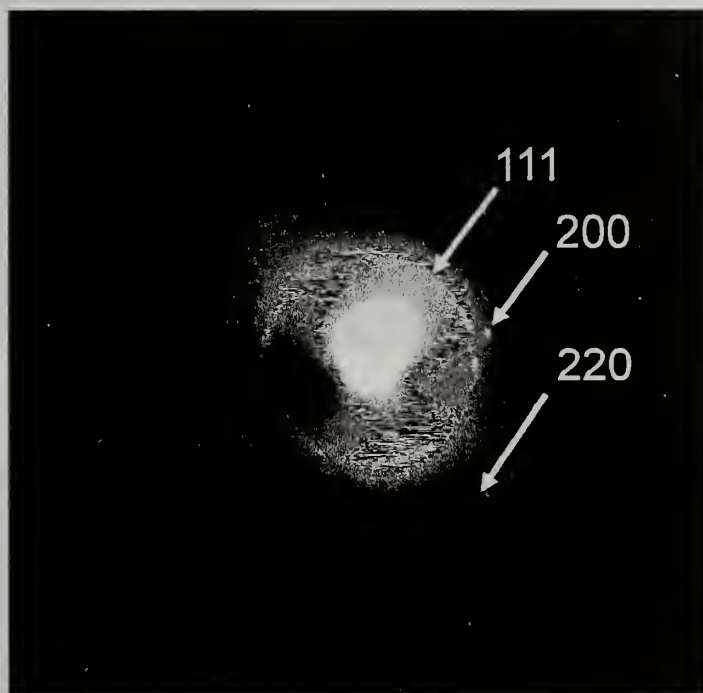
Figure 5.9. Selected Area Electron Diffraction of Pt clusters reduced by H2 under Sc CO2. The diffraction pattern indicates that the Pt clusters have typical fcc crystal structure.
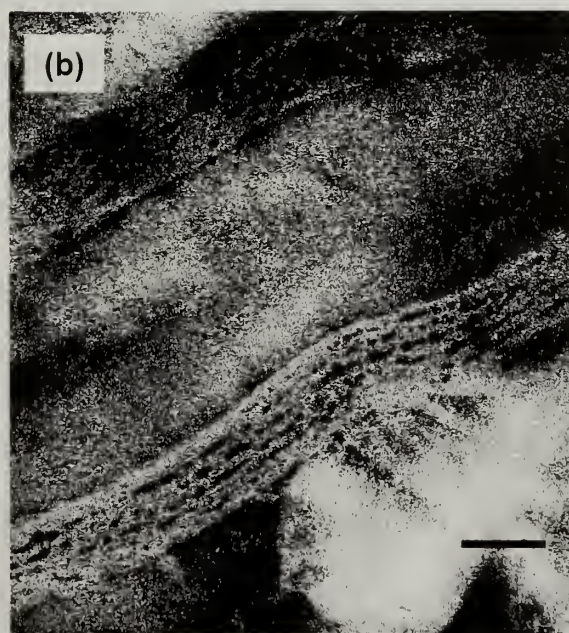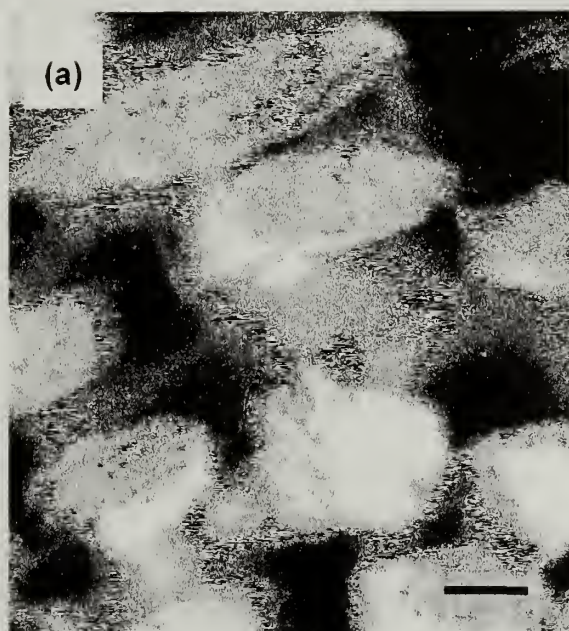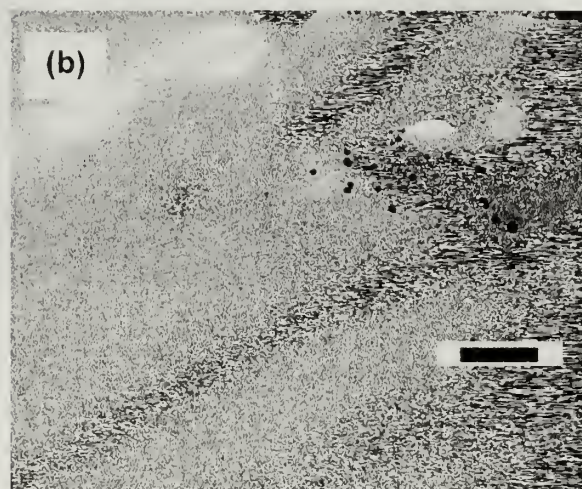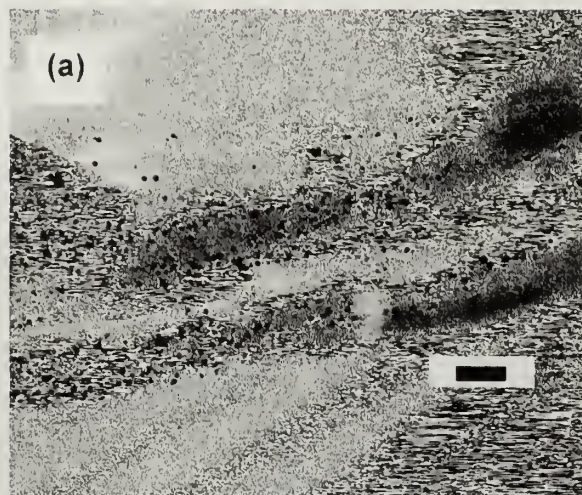
Figure 3.10. TEM micrographs of PMP/Pt nanorods. (a) View along the nanorod axis. (b) View normal to the nanorod axis. Scale bars: 200 nm.

102

nanorods from the view normal to the nanorod axis (Figure 5.10 (b)). Combined with the results for PMP/Polynorbornene nanorods. these results indicate that the Pt nanoclusters are formed in the amorphous or inter-lamellar regions.

5.4. Conclusions

Two types of composite nanorods were prepared from semicrystalline polymer nanorods by selective deposition of another polymer or metal using CO_2: polymer/polymer nanorods and polymer/metal nanorods. respectively. PMP/polynorbornene nanorods were prepared by polymerization of norbornene in liquid CO_2. TEM results indicate that the amorphous or inter-lamellar composite regions are formed as aligned spots along the nanorods. This morphology is interpretated as the result of frustrated trans-crystallization due to the curvature of cylindrical pores while the semi-crystalline polymer nanorods are formed inside alumina membrane.

PMP/Pt nanorods were prepared by introducing $CODPtMe_2$ into PMP nanorods using Sc CO_2 and reducing it to form Pt nanoclusters. TEM experiments verified that the Pt clusters are formed along the nanorod axis, which means they are formed in the amorphous or inter-lamellar regions of PMP nanorods.

5.5. References

(1)   Park, S.; Lim, J. H.; Chung. S. W.; Mirkin. C. A. *Science* **2004**. *303*. 348-351.

(2)   Kim, D. H.; Karan. P.; Goring. P.; Leclaire, J.; Caminade. A. M.; Majoral. J. P.; Gosele. U.; Steinhart. M.; Knoll, W. *Small* **2005**. *1*. 99-102.

(3)   Hou. S. F.; Harrell. C. C.; Trofin. L.; Kohli. P.; Martin. C. R. *J. Am. Chem. Soc.* **2004**. *126*. 5674-5675.

(4)   Ai. S. F.; Lu. G.; He. Q.; Li. J. B. *J. Am. Chem. Soc.* **2003**, *125*, 11140-11141.

(5)   Reiter. G.; Sommer. J. U. *Phys. Rev. Lett.* **1998**, *80*, 3771-3774.

(6)   Frank. C. W.; Rao. V.; Despotopoulou. M. M.; Pease. R. F. W.; Hinsberg. W. D.; Miller. R. D.; Rabolt. J. F. *Science* **1996**, *273*, 912-915.

(7)   Despotopoulou. M. M.; Frank. C. W.; Miller. R. D.; Rabolt. J. F. *Macromolecules* **1996**, *29*, 5797-5804.

(8)   Billon. N.; Magnet. C.; Haudin. J. M.; Lefebvre. D. *Colloid Polym. Sci.* **1994**, *272*, 633-654.

(9)   Billon. N.; Escleine. J. M.; Haudin. J. M. *Colloid Polym. Sci.* **1989**, *267*, 668-680.

(10)   Ajayan. P. M.; Stephan. O.; Colliex. C.; Trauth. D. *Science* **1994**, *265*, 1212-1214.

(11)   Qian. D.; Dickey. E. C.; Andrews. R.; Rantell. T. *Appl. Phys. Lett.* **2000**, *76*, 2868-2870.

(12)   Shaffer. M. S. P.; Windle. A. H. *Adv. Mater.* **1999**, *11*, 937-+.

(13)   Wetzel. B.; Haupert. F.; Zhang. M. Q. *Compos. Sci. Technol.* **2003**, *63*, 2055-2067.

(14)   Rong. M. Z.; Zhang. M. Q.; Zheng. Y. X.; Zeng. H. M.; Walter. R.; Friedrich, K. *Polymer* **2001**, *42*, 167-183.

(15)   Yu. Y. Y.; Chen. C. Y.; Chen. W. C. *Polymer* **2003**, *44*, 593-601.

(16)   Cao. C. In *Polymer Science and Engineering*; University of Massachusetts, 2002.

(17)   Furstner. A.; Koch. D.; Langemann. K.; Leitner. W.; Six. C. *Angew. Chem. Int. Edit.* **1997**, *36*, 2466-2469.

(18)   Furstner. A.; Ackermann, L.; Beck, K.; Hori, H.; Koch. D.; Langemann, K.; Liebl, M.; Six. C.; Leitner, W. *J. Am. Chem. Soc.* **2001**, *123*, 9000-9006.

(19)   Watkins. J. J. In *Polymer Science and Engineering*; University of Massachusetts, 1997.

(20)   Watkins. J. J.; Mccarthy. T. J. *Chem. Mater.* **1995**, *7*, 1991-&.

(21)   Armarego. W. L.; Perrin. D. D. *Purification of Laboratory Chemicals*; Butterworth-Heinemann: Oxford, 1996.

(22)   Ishida. H.; Bussi. P. *Macromolecules* **1991**, *24*, 3569-3577.

(23)   Stocker. W.; Schumacher. M.; Graff. S.; Thierry. A.; Wittmann. J. C.; Lotz.
        B. *Macromolecules* **1998**. *31*. 807-814.

(24)   Zoval. J. V.; Lee. J.; Gorer. S.; Penner. R. M. *J. Phys. Chem. B* **1998**. *102*.
        1166-1175.

APPENDIX

SURFACE MODIFICATION OF FLAT ALUMINA

Introduction

In Chapter 4, the surface of an alumina membrane was modified using a silane coupling agent in order to investigate the effect of the surface properties on the morphology of a block copolymer inside membrane pores. Specifically an alumina membrane was treated with octyltrimethoxysilane (OTMS), and microphase-separated morphologies of PS-*b*-PMMA made from this modified membrane and an untreated membrane was studied. The surface properties of OTMS-treated membrane pores couldn t be measured due to their size and shape by many methods that can be used for the analysis of flat surfaces, i.e. contact angle measurement, ellipsometry, etc. Only XPS analysis for the broken surface of OTMS-treated membranes was performed. Here, a flat alumina surface was treated with the same silane coupling agent at the same conditions and its surface properties are analyzed for comparative purposes.

Experimental

A flat alumina surface was prepared by aluminum vapor deposition on a silicon wafer. A silicon wafer was obtained from International Wafer Service (100 orientation, P/B doped, resistivity from 20 to 40 Ω cm). A disk of silicon wafer was rinsed with toluene, ethanol, and water and plasma cleaned. Aluminum was deposited on this silicon wafer by thermal deposition at 10^{-6} torr. Disks were cut into 1.5 cm x 1.5 cm

106

square pieces. These aluminum-deposited silicon wafer samples were rinsed with toluene, ethanol, and water and then plasma cleaned. These samples were held in a custom designed slotted holder and placed inside a closed flask with 0.5 ml of OTMS at 70 °C for three days. The modified samples were rinsed with toluene, hexane and ethanol and dried overnight under vacuum at 60 °C.
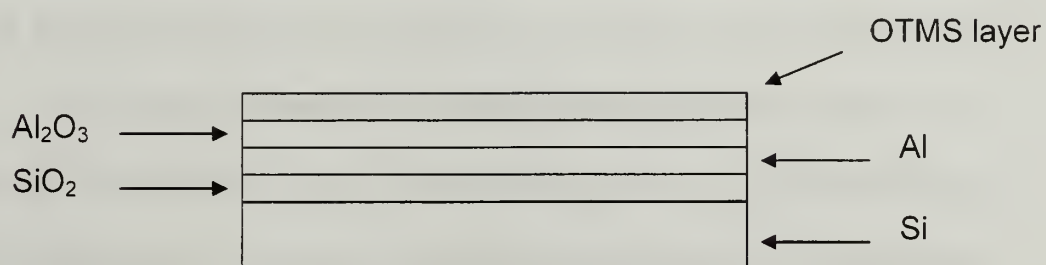
Figure A.1. Schematic illustration of OTMS-treated aluminum-deposited silicon wafer.

Characterization

Layer Thickness. The schematic illustration of the final sample is shown in Figure A.1. The thickness of OTMS, aluminum oxide, and aluminum layers were measured by SOPRA GES-5 Variable Angle Spectroscopic Ellipsometry (VASE). The energy of the incident light varied from 1.5eV to 6.0eV. The optical model was built following Figure A.1, and the Marquatdt-Levenberg algorithm was used to fit the obtained tan Ψ and cos Δ data to the optical mode.[1,2] Table A.1 shows the thickness of the layers. The thickness of the deposited aluminum layer is ~ 30 nm, which has enough thickness to change the surface of silicon wafer. The OTMS layer has ~ 2 nm, which is close to the thickness of a self-assembled monolayer.

Table A.1. Thicknesses of each layer of OTMS treated Al deposited silicon wafer.

Layer	Thickness (Å)
OTMS	20.2
Al_2O_3	44.4
Al	297.8

Wettability. The water contact angle data for this sample and the OTMS-treated silicon wafer is shown in Table A.2. The water contact angles for the OTM- treated silicon wafer is quite similar to those for the self-assembled monolayer of octyltrichlorosilane on a silicon wafer, which is θ_A of 110° and θ_R of 95.[3] The advancing contact angle for the OTMS-treated aluminum oxide surface is larger than that for OTMS-treated silicon wafer, and the receding contact angle for the sample is smaller than that for the OTMS-treated silicon wafer.[4] This discrepancy is thought to be due to the different hydroxyl group densities between these two surfaces, or could also be ascribed to roughness increasing hysteresis.

Table A.2. Water contact angle data for OTMS-treated aluminum oxide surface and OTMS treated silicon wafer.

	θ_A	θ_R
Al_2O_3	Spread	Spread
OTMS-Al_2O_3	115	87
SiO_2	Spread	Spread
OTMS-SiO_2	110	97

XPS Analysis. The surfaces of the aluminum coated silicon wafer and the OTMS-treated aluminum deposited silicon wafer were analyzed by X-ray photoelectron

108

spectroscopy. Figure A.2 shows Al$_2$p peaks of the aluminum-coated silicon wafer at 15 degree (lower peak) and 75 degree (upper peak) take-off angles. The 75 degree take-off angle shows an Al$_{2p}$ peak from aluminum and aluminum oxide, while the 15 degree take-off angle spectrum indicates no aluminum. This indicates that a thin (~ 2nm) aluminum oxide layer was formed on the aluminum, which is consistent with the ellipsometry result.
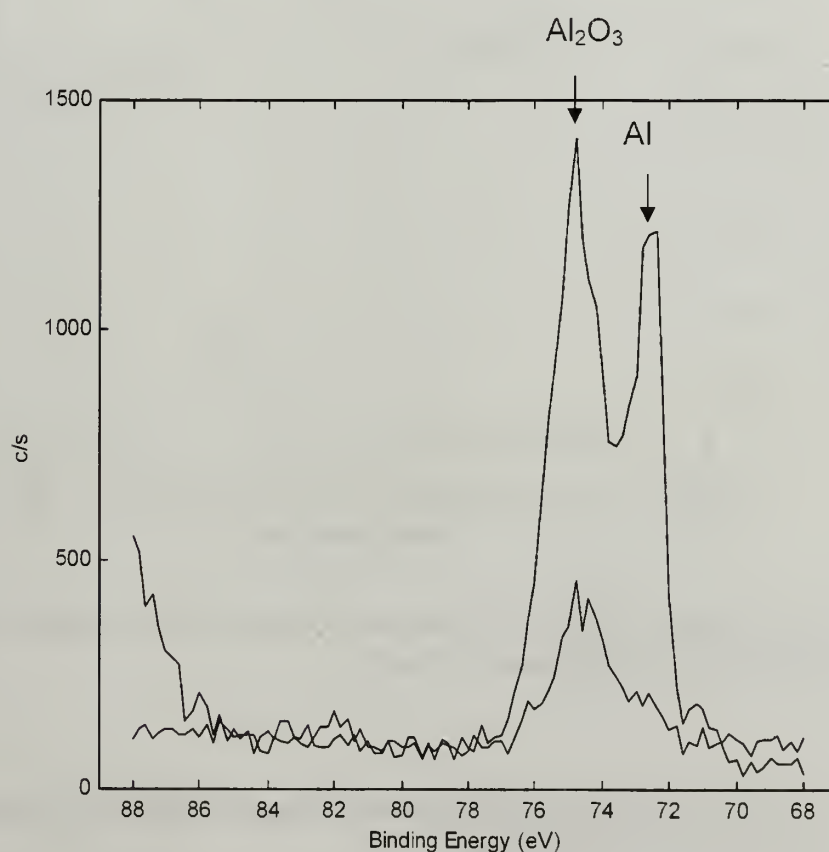
Figure A.2. Al$_{2p}$ peak from aluminum deposited silicon wafer at 15 degree (lower) and 75 degree take-off angle.

The XPS data for the OTMS-treated aluminum oxide shows a Si_{2p} peak, which is from the silane coupling agent (Figure A.3.) The atomic composition of carbon, oxygen, aluminum, and silicon are listed in Table A.3.
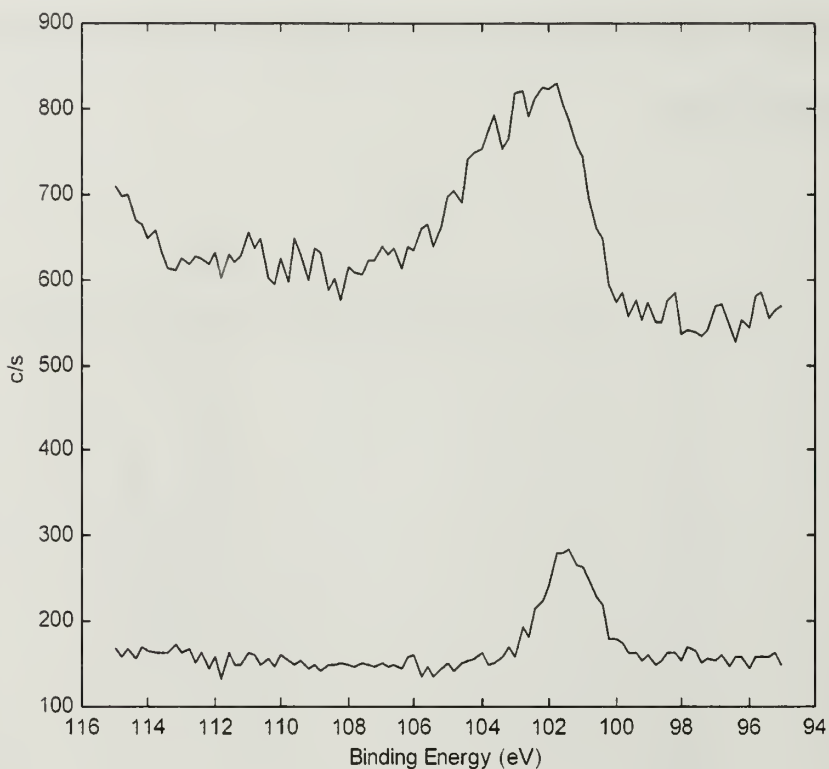
Figure A.3. Si_{2p} peak from the OTMS-treated aluminum oxide surface at 15 degree (lower) and 75 degree (upper) take-off angle.

Table A.3. Atomic composition of the OTMS-treated aluminum oxide surface from XPS (15 degree take-off angle) data.

	Atomic %
C	40.7
O	37.9
Al	18.3
Si	3.1

References

(1)   Woollam, J. A.; Snyder, P. G. *Mat. Sci. Eng. B-Solid* **1990**, *5*, 279-283.

(2)   Goncalves, D.; Irene, E. A. *Quim. Nova* **2002**, *25*, 794-800.

(3)   Fadeev, A. Y.; McCarthy, T. J. *Langmuir* **2000**, *16*, 7268-7274.

(4)   Wang, D. H.; Ni, Y. H.; Huo, Q.; Tallman, D. E. *Thin Solid Films* **2005**, *471*, 177-185.

BIBLIOGRAPHY

Abel, E. W.: Pollard, F. H.: Uden, P. C.: Nickless, G., *J. Chromatogr.* **1966**, 22, 1, 23.

Ai, S. F.: Lu, G.: He, Q.: Li, J. B., *J. Am. Chem. Soc.* **2003**, 125, 37, 11140.

Ajayan, P. M.: Stephan, O.: Colliex, C.: Trauth, D., *Science* **1994**, 265, 5176, 1212.

Alexandridis, P.: Holzwarth, J. F.: Hatton, T. A., *Macromolecules* **1994**, 27, 9, 2414.

Armarego, W. L.: Perrin, D. D., *Purification of Laboratory Chemicals.* ed.: Butterworth-Heinemann: Oxford, 1996: 'Vol.' p.

Badley, R. D.: Ford, W. T.: Mcenroe, F. J.: Assink, R. A., *Langmuir* **1990**, 6, 4, 792.

Bates, F. S., *Science* **1991**, 251, 4996, 898.

Bates, F. S.: Fredrickson, G. H., *Annu. Rev. Phys. Chem.* **1990**, 41, 525.

Bates, F. S.: Fredrickson, G. H., *Physics Today* **1999**, 52, 2, 32.

Biernat, J. F.: Konieczka, P.: Tarbet, B. J., *Sep. Purif. Methods* **1994**, 23, 2, 77.

Billon, N.: Escleine, J. M.; Haudin, J. M. *Colloid Polym. Sci.* **1989**, 26⁷, 668-680.

Billon, N.: Magnet, C.: Haudin, J. M.: Lefebvre, D. *Colloid Polym. Sci.* **1994**, 2⁷2, 633-654.

Boltau, M.: Walheim, S.: Mlynek, J.: Krausch, G.: Steiner, U., *Nature* **1998**, 391, 6670, 877.

Brandrup, J.: Immergut, E. H.: Grulke, E. A., *Polymer Handbook.* 4th ed.; John Wiley & Sons, Inc.: 1999.

Brown, I. G.: Anders, A.: Dickinson, M. R.; MacGill, R. A.; Monteiro, O. R., *Surf. Coat. Tech.* **1999**, 112, 1-3, 271.

Buck, E.: Fuhrmann, J., *Macromolecules* **2001**, 34, 7, 2172.

Cao, C. Ph. D. Thesis, University of Massachusetts, 2002.

Carvalho, B. L.: Thomas, E. L., *Phys. Rev. Lett.* **1994**, 73, 24, 3321.

Chakrabarti, A.: Chen, H., *J. Polym. Sci. Pol. Phys.* **1998**, 36, 17, 3127.

Che, G.; Lakshmi, B. B.; Martin, C. R.; Fisher, E. R.; Ruoff, R. S., *Chem. Mater.* **1998,** 10, 1, 260.

Che, G. L.; Lakshmi, B. B.; Fisher, E. R.; Martin, C. R., *Nature* **1998,** 393, 6683, 346.

Chen, H.; Chakrabarti, A., *J. Chem. Phys.* **1998,** 108, 16, 6897.

Chiou, J. S.; Barlow, J. W.; Paul, D. R., *J. Appl. Polym. Sci.* **1985,** 30, 6, 2633.

Condo, P. D.; Johnston, K. P., *J. Polym. Sci. Pol. Phys.* **1994,** 32, 3, 523.

Condo, P. D.; Paul, D. R.; Johnston, K. P., *Macromolecules* **1994,** 27, 2, 365.

Coulon, G.; Collin, B.; Chatenay, D.; Gallot, Y. *Journal De Physique Ii* **1993,** *3,* 697-717.

Despotopoulou, M. M.; Frank, C. W.; Miller, R. D.; Rabolt, J. F. *Macromolecules* **1996,** *29,* 5797-5804.

Diggle, J. W.; Downie, T. C.; Goulding, C. W., *Chem. Rev.* **1969,** 69, 3, 365.

Discher, B. M.; Won, Y. Y.; Ege, D. S.; Lee, J. C. M.; Bates, F. S.; Discher, D. E.; Hammer, D. A., *Science* **1999,** 284, 5417, 1143.

Dulcey, C. S.; Georger, J. H.; Krauthamer, V.; Stenger, D. A.; Fare, T. L.; Calvert, J. M., *Science* **1991,** 252, 5005, 551.

Fadeev, A. Y.; McCarthy, T. J., *Langmuir* **1999,** 15, 11, 3759.

Fadeev, A. Y.; McCarthy, T. J., *Langmuir* **2000,** 16, 18, 7268.

Feng, X.; Fryxell, G. E.; Wang, L. Q.; Kim, A. Y.; Liu, J.; Kemner, K. M., *Science* **1997,** 276, 5314, 923.

Frank, C. W.; Rao, V.; Despotopoulou, M. M.; Pease, R. F. W.; Hinsberg, W. D.; Miller, R. D.; Rabolt, J. F. *Science* **1996,** *273,* 912-915.

Franklin, R. W., *Nature* **1957,** 180, 4600, 1470.

Furneaux, R. C.; Rigby, W. R.; Davidson, A. P., *Nature* **1989,** 337, 6203, 147.

Fürstner, A.; Ackermann, L.; Beck, K.; Hori, H.; Koch, D.; Langemann, K.; Liebl, M.; Six, C.; Leitner, W., *J. Am. Chem. Soc.* **2001,** 123, 37, 9000.

Fürstner, A.; Koch, D.; Langemann, K.; Leitner, W.; Six, C., *Angew. Chem. Int. Edit.* **1997,** 36, 22, 2466.

Goncalves, D.; Irene, E. A., *Quim. Nova* **2002,** 25, 5, 794.

Hamley, I. W., *The physics of block copolymers*. ed.: Oxford University Press: Oxford, 1998.

Handa, Y. P.; Lampron, S.; Oneill, M. L., *J. Polym. Sci. Pol. Phys.* **1994**, 32, 15, 2549.

He, X. H.; Song, M.; Liang, H. J.; Pan, C. Y., *J. Chem. Phys.* **2001**, 114, 23, 10510.

Helfand, E.; Wasserman, Z. R., *Macromolecules* **1976**, 9, 6, 879.

Hou, S. F.; Harrell, C. C.; Trofin, L.; Kohli, P.; Martin, C. R., *J. Am. Chem. Soc.* **2004**, 126, 18, 5674.

Huang, E.; Mansky, P.; Russell, T. P.; Harrison, C.; Chaikin, P. M.; Register, R. A.; Hawker, C. J.; Mays, J., *Macromolecules* **2000**, 33, 1, 80.

Ishida, H.; Bussi, P., *Macromolecules* **1991**, 24, 12, 3569.

Jansen, J.; Treiner, C.; Vaution, C.; Puisieux, F., *Int. J. Pharm.* **1994**, 103, 1, 19.

Jenekhe, S. A.; Chen, X. L., *Science* **1998**, 279, 5358, 1903.

Jeon, N. L.; Finnie, K.; Branshaw, K.; Nuzzo, R. G., *Langmuir* **1997**, 13, 13, 3382.

Jessensky, O.; Muller, F.; Gosele, U., *Appl. Phys. Lett* **1998**, 72, 10, 1173.

Jessensky, O.; Muller, F.; Gosele, U., *J. Electrochem. Soc.* **1998**, 145, 11, 3735.

Johnson, B. J. S.; Stein, A., *Inorg. Chem.* **2001**, 40, 4, 801.

Kamiya, Y.; Hirose, T.; Mizoguchi, K.; Terada, K., *J. Polym. Sci. Pol. Phys.* **1988**, 26, 7, 1409.

Kamiya, Y.; Mizoguchi, K.; Hirose, T.; Naito, Y., *J. Polym. Sci. Pol. Phys.* **1989**, 27, 4, 879.

Kataoka, K.; Kwon, G. S.; Yokoyama, M.; Okano, T.; Sakurai, Y., *J. Control. Release* **1993**, 24, 1-3, 119.

Kawai, S.; Ueda, R., *J. Electrochem. Soc.* **1975**, 122, 1, 32.

Keller, F.; Hunter, M. S.; Robinson, D. L., *J. Electrochem. Soc.* **1953**, 100, 9, 411.

Kellogg, G. J.; Walton, D. G.; Mayes, A. M.; Lambooy, P.; Russell, T. P.; Gallagher, P. D.; Satija, S. K. *Phys. Rev. Lett.* **1996**, 76, 2503-2506.

Kim, D. H.; Karan, P.; Goring, P.; Leclaire, J.; Caminade, A. M.; Majoral, J. P.; Gosele, U.; Steinhart, M.; Knoll, W., *Small* **2005**, 1, 1, 99.

Kim. E.: Xia, Y. N.: Whitesides. G. M.. *Nature* **1995,** 376. 6541. 581.

Kim. H. C.: Russell. T. P.. *J. Polym. Sci. Pol. Phys.* **2001,** 39. 6, 663.

Kim, T.: Moon, S. I.: Xiang, H. Q.; Shin, K.: Russell, T. P.: McCarthy, T. J.. *Abstr. Pap. Am. Chem. S.* **2004,** 228. U491.

Koneripalli, N.: Singh, N.: Levicky, R.: Bates, F. S.: Gallagher, P. D.: Satija, S. K. *Macromolecules* **1995.** 28. 2897-2904.

Kono. M.: Sun, X.; Li. R.: Wong, K. C.: Mitchell, K. A. R.: Foster. T.. *Surf. Rev. Lett.* **2001,** 8. 1-2. 43.

Koppi. K. A.: Tirrell. M.: Bates. F. S.. *Phys. Rev. Lett.* **1993,** 70. 10. 1449.

Kung. E.: Lesser. A. J.: McCarthy. T. J.. *Macromolecules* **2000,** 33. 22. 8192.

Lambooy. P.: Russell. T. P.: Kellogg. G. J.: Mayes. A. M.: Gallagher. P. D.: Satija. S. K.. *Phys. Rev. Lett.* **1994,** 72. 18. 2899.

Lee. S. B.: Mitchell. D. T.: Trofin. L.: Nevanen. T. K.: Soderlund. H.: Martin. C. R.. *Science* **2002,** 296. 5576. 2198.

Legrange. J. D.: Markham. J. L.: Kurkjian. C. R.. *Langmuir* **1993,** 9. 7. 1749.

Li, A. P.: Muller, F.: Birner. A.: Nielsch. K.; Gosele, U.. *J. Appl. Phys.* **1998,** 84. 11. 6023.

Li, A. P.: Muller, F.: Birner. A.: Nielsch. K.; Gosele, U.. *Adv. Mater.* **1999,** 11, 6. 483.

Li. F. Y.; Zhang, L.; Metzger. R. M., *Chem. Mater.* **1998,** 10, 9, 2470.

Li, W. H.: Wickham, R. A.; Garbary, R. A.. *Macromolecules* **2006,** 39. 2. 806.

Liu, X. G.: Zhang. Y.; Goswami, D. K.; Okasinski. J. S.: Salaita. K.; Sun. P.: Bedzyk. M. J.: Mirkin. C. A., *Science* **2005,** 307, 5716, 1763.

Malmsten. M.: Lindman. B., *Macromolecules* **1992,** 25. 20. 5440.

Malygin, A. A.: Malkov, A. A.; Dubrovenskii. S. D.. *Stud. Surf. Sci. Catal.* **1996,** 99. 213.

Mansky. P.; Liu, Y.; Huang, E.; Russell, T. P.: Hawker. C.. *Science* **1997,** 275. 5305. 1458.

Martin. C.. *Science* **1994,** 266. 1961.

Masuda. H.: Fukuda. K.. *Science* **1995,** 268. 5216. 1466.

Masuda. H.: Hasegwa. F.: Ono. S.. *J. Electrochem. Soc.* **1997**, 144. 5. L127.

Masuda. H.: Satoh. M.. *Jpn. J. Appl. Phys. 2* **1996**, 35. 1B. L126.

Masuda. H.: Yamada. H.: Satoh. M.: Asoh. H.: Nakao. M.: Tamamura. T.. *Appl. Phys. Lett.* **1997**, 71. 19. 2770.

Masuda. H.: Yamada. H.: Satoh. M.: Asoh. H.: Nakao. M.: Tamamura. T.. *Appl. Phys. Lett.* **1997**, 71. 19. 2770.

McHugh. M. A.: Krukonis. V. J.. *Supercritical Fluid Extraction.* ed.: Butterworth-Heinemann: Newton. 1994.

Menelle. A.: Russell. T. P.: Anastasiadis. S. H.: Satija. S. K.: Majkrzak. C. F. *Phys. Rev. Lett.* **1992**. *68.* 67-70.

Michailowski. A.: AlMawlawi. D.: Cheng. G. S.: Moskovits. M.. *Chem. Phys. Lett.* **2001**, 349. 1-2. 1.

Miller. C. J.: Majda. M.. *J. Am. Chem. Soc.* **1985**, 107. 5. 1419.

Milner. S. T.: Morse. D. C.. *Phys. Rev. E* **1996**, 54. 4. 3793.

Moon. S. I.: McCarthy. T. J.. *Macromolecules* **2003**, 36. 12. 4253.

Morkved. T. L.: Lu. M.: Urbas. A. M.: Ehrichs. E. E.: Jaeger. H. M.; Mansky, P.: Russell. T. P.. *Science* **1996**, 273. 5277. 931.

Newitt. D. M. e. a.. *Thermodynamic Functions of Gases.* ed.: Butterworths Scientific Publications: London. 1956.

Ohta. T.: Kawasaki. K.. *Macromolecules* **1986**, 19. 10. 2621.

Park. C.: Cheng. J. Y.: Fasolka. M. J.: Mayes. A. M.: Ross. C. A.: Thomas. E. L.: De Rosa. C.. *Appl. Phys. Lett.* **2001**, 79. 6. 848.

Park. M.: Harrison. C.: Chaikin. P. M.: Register. R. A.; Adamson, D. H.. *Science* **1997**, 276. 5317. 1401.

Park. S.: Lim. J. H.: Chung. S. W.: Mirkin. C. A.. *Science* **2004**, 303. 5656. 348.

Qian. D.: Dickey. E. C.: Andrews, R.; Rantell. T.. *Appl. Phys. Lett.* **2000**, 76. 20. 2868.

Qin. L. D.: Park. S.: Huang. L.: Mirkin. C. A., *Science* **2005**, 309. 5731. 113.

Radzilowski. L. H.: Carvalho. B. L.: Thomas. E. L.. *J. Polym. Sci. Pol. Phy.* **1996**, 34. 17. 3081.

Regnier, F. E.; Unger, K. K.; Majors, R. E., *J. Chromatogr.* **1991**, 544, 1-2, R9.

Reiter, G.; Sommer, J. U. *Phys. Rev. Lett.* **1998**, *80*, 3771-3774.

Rockford, L.; Liu, Y.; Mansky, P.; Russell, T. P.; Yoon, M.; Mochrie, S. G. J., *Phys. Rev. Lett.* **1999**, 82, 12, 2602.

Rockford, L.; Mochrie, S. G. J.; Russell, T. P., *Macromolecules* **2001**, 34, 5, 1487.

Rong, M. Z.; Zhang, M. Q.; Zheng, Y. X.; Zeng, H. M.; Walter, R.; Friedrich, K., *Polymer* **2001**, 42, 1, 167.

Ross, C. B.; Sun, L.; Crooks, R. M., *Langmuir* **1993**, 9, 3, 632.

Saito, M.; Kirihara, M.; Taniguchi, T.; Miyagi, M., *Appl. Phys. Lett.* **1989**, 55, 7, 607.

Sander, L. C.; Wise, S. A., *Crit. Rev. Anal. Chem.* **1987**, 18, 4, 299.

Sevink, G. J. A.; Zvelindovsky, A. V.; Fraaije, J. G. E. M.; Huinink, H. P., *J. Chem. Phys.* **2001**, 115, 17, 8226.

Shaffer, M. S. P.; Windle, A. H., *Adv. Mater.* **1999**, 11, 11, 937.

Shieh, Y. T.; Su, J. H.; Manivannan, G.; Lee, P. H. C.; Sawan, S. P.; Spall, W. D., *J. Appl. Polym. Sci.* **1996**, 59, 4, 695.

Shin, K.; Xiang, H. Q.; Moon, S. I.; Kim, T.; McCarthy, T. J.; Russell, T. P., *Science* **2004**, 306, 76.

Shiraki, M.; Wakui, Y.; Tokushima, T.; Tsuya, N., *IEEE Trans Magn* **1985**, 21, 5, 1465.

Sofia, S. J.; Premnath, V.; Merrill, E. W., *Macromolecules* **1998**, 31, 15, 5059.

Sohn, B. H.; Yun, S. H., *Polymer* **2002**, 43, 8, 2507.

Steinhart, M.; Wendorff, J. H.; Greiner, A.; Wehrspohn, R. B.; Nielsch, K.; Schilling, J.; Choi, J.; Gosele, U., *Science* **2002**, 296, 5575, 1997.

Stenger, D. A.; Georger, J. H.; Dulcey, C. S.; Hickman, J. J.; Rudolph, A. S.; Nielsen, T. B.; Mccort, S. M.; Calvert, J. M., *J. Am. Chem. Soc.* **1992**, 114, 22, 8435.

Stocker, W.; Schumacher, M.; Graff, S.; Thierry, A.; Wittmann, J. C.; Lotz, B., *Macromolecules* **1998**, 31, 3, 807.

Suh, K. Y.; Kim, Y. S.; Lee, H. H., *Adv. Mater.* **2001**, 13, 18, 1386.

Sun, Y.; Steinhart, M.; Zschech, D.; Adhikari, R.; Michler, G. H.; Gosele, U., *Mac. Rad. Comm.* **2005**, 26, 369.

Textor, M.; Ruiz, L.; Hofer, R.; Rossi, A.; Feldman, K.; Hahner, G.; Spencer, N. D.. *Langmuir* **2000**, 16, 7, 3257.

Thompson, G. E.; Furneaux, R. C.; Wood, G. C.; Richardson, J. A.; Goode, J. S.. *Nature* **1978**, 272, 5652, 433.

Tierney, M. J.; Martin, C. R.. *J. Electrochem. Soc.* **1990**, 137, 12, 3789.

Ton-That, C.; Shard, A. G.; Teare, D. O. H.; Bradley, R. H.. *Polymer* **2001**, 42, 3, 1121.

Tsyganenko, A. A.; Mardilovich, P. P.. *J. Chem. Soc. Faraday T.* **1996**, 92, 23, 4843.

Wang, D. H.; Ni, Y. H.; Huo, Q.; Tallman, D. E.. *Thin Solid Films* **2005**, 471, 1-2, 177.

Wang, W. C. V.; Kramer, E. J.; Sachse, W. H.. *J. Polym. Sci. Pol. Phys.* **1982**, 20, 8, 1371.

Watkins, J. J. Ph.D. Thesis, University of Massachusetts, 1997.

Watkins, J. J.; Blackburn, J. M.; McCarthy, T. J.. *Chem. Mater.* **1999**, 11, 2, 213.

Watkins, J. J.; Mccarthy, T. J.. *Macromolecules* **1994**, 27, 17, 4845.

Watkins, J. J.; Mccarthy, T. J.. *Macromolecules* **1995**, 28, 12, 4067.

Watkins, J. J.; Mccarthy, T. J.. *Chem. Mater.* **1995**, 7, 11, 1991.

Wetzel, B.; Haupert, F.; Zhang, M. Q.. *Compos. Sci. Technol.* **2003**, 63, 14, 2055.

Wissinger, R. G.; Paulaitis, M. E.. *J. Polym. Sci. Pol. Phys.* **1987**, 25, 12, 2497.

Wissinger, R. G.; Paulaitis, M. E.. *J. Polym. Sci. Pol. Phys.* **1991**, 29, 5, 631.

Woollam, J. A.; Snyder, P. G.. *Mat. Sci. Eng. B-Solid* **1990**, 5, 2, 279.

Xia, Y. N.; Zhao, X. M.; Whitesides, G. M.. *Microelectron. Eng.* **1996**, 32, 1-4, 255.

Xiang, H.; Shin, K.; Kim, T.; Moon, S. I.; McCarthy, T. J.; Russell, T. P., *Macromolecules* **2005**, 38, 4, 1055.

Xiang, H. Q.; Shin, K.; Kim, T.; Moon, S. I.; McCarthy, T. J.; Russell, T. P., *Macromolecules* **2004**, 37, 15, 5660.

Yang, P. D.; Wirnsberger, G.; Huang, H. C.; Cordero, S. R.; McGehee, M. D.; Scott, B.; Deng, T.; Whitesides, G. M.; Chmelka, B. F.; Buratto, S. K.; Stucky, G. D.. *Science* **2000**, 287, 5452, 465.

Yu, B.; Sun, P. C.; Chen, T. C.; Jin, Q. H.; Ding, D. T.; Li, B. H.; Shi, A. C., *Phys. Rev. Lett.* **2006**, 96, 13.

Yu, Y. Y.; Chen, C. Y.; Chen, W. C., *Polymer* **2003**, 44, 3, 593.

Zhang, M. Q.; Desai, T.; Ferrari, M., *Biomaterials* **1998**, 19, 10, 953.

Zhao, D. Y.; Feng, J. L.; Huo, Q. S.; Melosh, N.; Fredrickson, G. H.; Chmelka, B. F.; Stucky, G. D., *Science* **1998**, 279, 5350, 548.

Zhao, X. L.; Kopelman, R., *J. Phys. Chem.-Us* **1996**, 100, 26, 11014.

Zoval, J. V.; Lee, J.; Gorer, S.; Penner, R. M., *J. Phys. Chem. B* **1998**, 102, 7, 1166.